LOCALIZED CORROSION AND STRESS CORROSION CRACKING CHARACTERISTICS OF LOW-ALUMINUM-CONTENT IRON-ALUMINUM ALLOYS

J. G. Kim and R. A. Buchanan

Dept. of Materials Science and Engineering
University of Tennessee
Knoxville, TN 37996-2200

ABSTRACT

The aqueous corrosion behavior of FAPY, a new low-Al-content Fe-Al alloy (Fe-16.1Al-5.4Cr-1.1Mo-0.11C-0.11Zr-0.06Y, at. %), was studied in various electrolytes and compared with reference materials. Corrosion rates for FAPY were much closer to that of 304L stainless steel than to the plain-carbon and low-alloy steels evaluated. Three-week crevice corrosion tests were performed in chloride-containing solutions on FAPY, and for comparison on 304L stainless steel. The FAPY alloy was less resistant to crevice corrosion than the 304L stainless steel. In the 3.5 wt. % NaCl solution, the FAPY alloy was subject to severe crevice corrosion. Slow-strain-rate corrosion tests were conducted at the freely-corroding open-circuit potential and at potentiostatically-controlled anodic and cathodic potentials to evaluate the environmental-embrittlement susceptibility. It was found that the FAPY alloy was susceptible to hydrogen embrittlement and anodic-dissolution stress corrosion cracking, but at the freely-corroding and hydrogen-producing-cathodic potentials, the ductilities were significantly higher than those for Fe_3Al-based iron aluminides.

INTRODUCTION

Iron aluminides based on the Fe_3Al stoichiometry posses excellent resistance to high-temperature oxidation and sulfidation. However, a major deterrent to their commercialization is the limited room-temperature ductility. Investigations have shown the low ductility to be caused by hydrogen embrittlement which occurs due to the reaction of water vapor with active aluminum.[1-3] Recent studies at the Oak Ridge National Laboratory (ORNL) have shown that the environmental-embrittlement effect can be minimized by reducing the aluminum content from its Fe_3Al-based value of 28 at. % to a value of 16 at. %, which places the new alloys in the disordered phase field.[4] The new low-Al Fe-Al alloys posses room-temperature ductilities in excess of 25 %,[4] while retaining good high-temperature oxidation and sulfidation resistance. The objective of the present

present study was to investigate the aqueous corrosion and stress corrosion cracking behaviors of one of the new low-Al Fe-Al alloys.

PROCEDURES AND RESULTS

The new low-Al Fe-Al alloy investigated was designated as FAPY by ORNL and consisted of Fe-16.1Al-5.4Cr-1.07Mo-0.11C-0.11Zr-0.06Y (at. %). Prior to testing, specimens were annealed in air for 1 hour at 800 ^{o}C and air cooled. In addition to the FAPY alloy, and depending on the specific evaluation, the following materials were evaluated for comparison: AISI 1010 plain-carbon steel, A387-G22 2 1/4 Cr - 1 Mo low-alloy steel, AISI 304L stainless steel, and the Fe_3Al-based iron aluminides, FA-84 (Fe-28Al-2Cr-0.05B, at. %), FA-129 (Fe-28Al-5Cr-0.5Nb-0.2C, at. %), and FAL-Mo (Fe-28Al-5Cr-1Mo-0.08Zr-0.04B, at. %).

Anodic Polarization Behaviors

Cyclic anodic polarization evaluations were performed on FAPY, and for comparison on the plain-carbon, low-alloy and stainless steels. Tests were conducted in the following electrolytes: distilled water (plus 0.01 wt. % Na_2SO_4 to provide adequate conductivity), tap water (approximately 15 ppm Cl^-), a mild acid-chloride solution (200 ppm Cl^-, pH=4), a 3.5 wt. % NaCl solution (pH $\approx$ 7) and 1 N NaOH. An EG&G Model 273 potentiostat was employed to conduct the polarization tests at a scan rate of 600 mV/h. Each solution was aerated by sparging with pure oxygen before as well as during the test. The results are shown in Figures 1-5.

In the distilled water (Figure 1), the plain-carbon and low-alloy steels exhibited active corrosion, i.e., no passivation, whereas the FAPY alloy and the stainless steel exhibited passivation to very high potentials. The polarization behaviors in tap-water (Figure 2) showed no significant differences compared to those in distilled water, except that FAPY demonstrated a large hysteresis loop indicating susceptibility to localized corrosion. In the mild acid-chloride solution (Figure 3), the plain-carbon and low-alloy steels underwent active corrosion only, whereas the FAPY alloy and the stainless steel remained passivated to their respective breakdown potentials. The corrosion, breakdown and protection potentials were higher for the stainless steel than for the FAPY alloy. In the much-higher-chloride 3.5 wt. % NaCl solution (Figure 4), again the plain-carbon and low-alloy steels underwent active corrosion only; however, the FAPY alloy and the stainless steel remained passivated to their respective breakdown potentials. The breakdown and protection potentials were

higher for the stainless steel than for the FAPY alloy. Comparing the results in the mild acid-chloride solution (Figure 3) and the 3.5 wt. % NaCl solution (Figure 4), the breakdown and protection potentials for both the FAPY alloy and the stainless steel decreased in the 3.5 wt. % NaCl solution due to the higher chloride concentration. In the highly-basic 1N NaOH solution (Figure 5), all of the materials exhibited very similar and excellent corrosion behavior by passivating to high potentials. Overall, the polarization behavior of the FAPY alloy was much closer to that of the 304L stainless steel than to the plain-carbon and low-alloy steels.

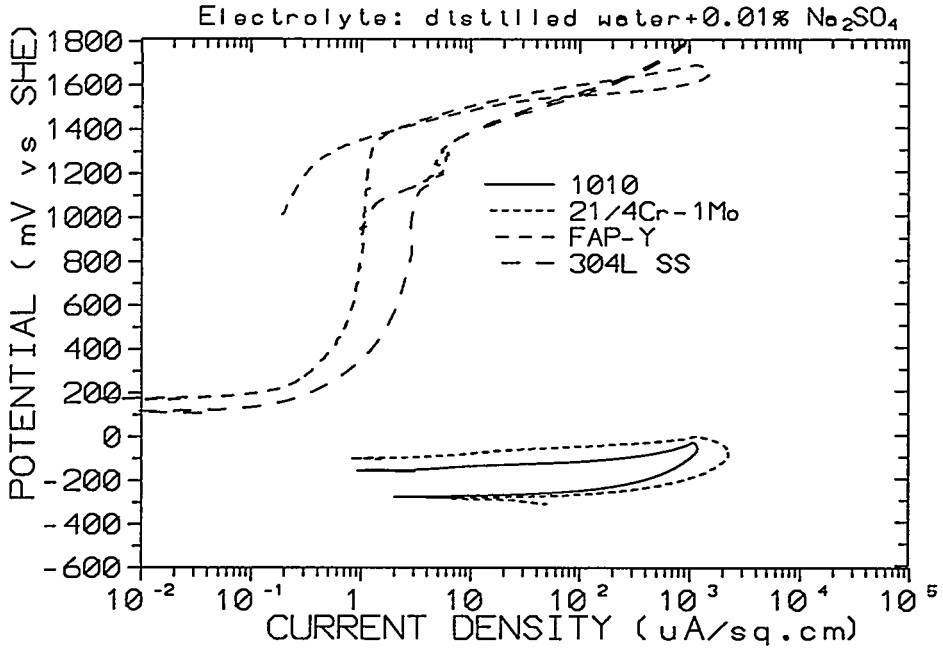

Fig. 1. Cyclic anodic polarization curves in aerated distilled water.

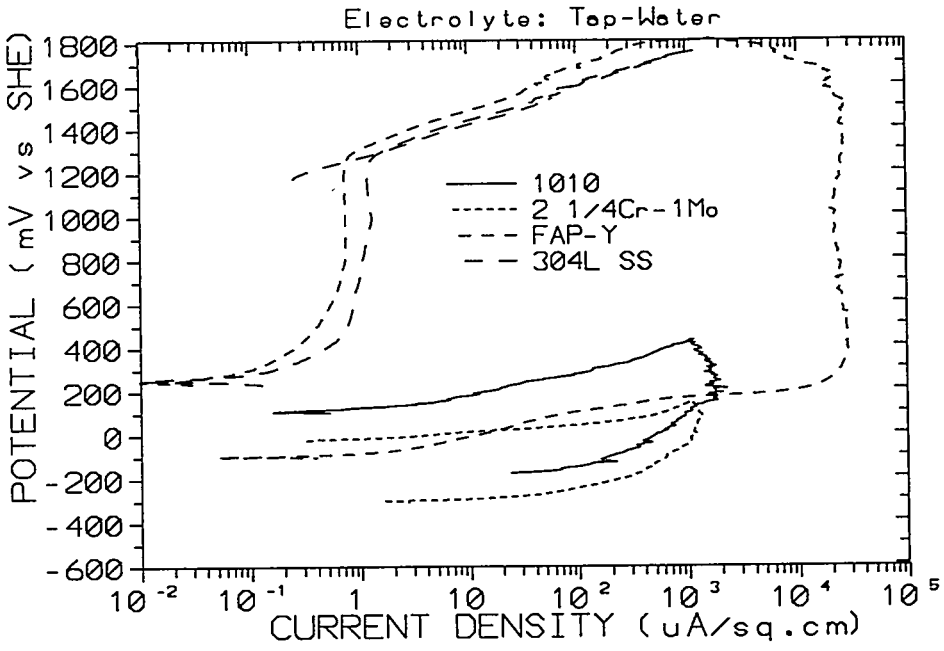

Fig. 2. Cyclic anodic polarization curves in aerated tap-water.

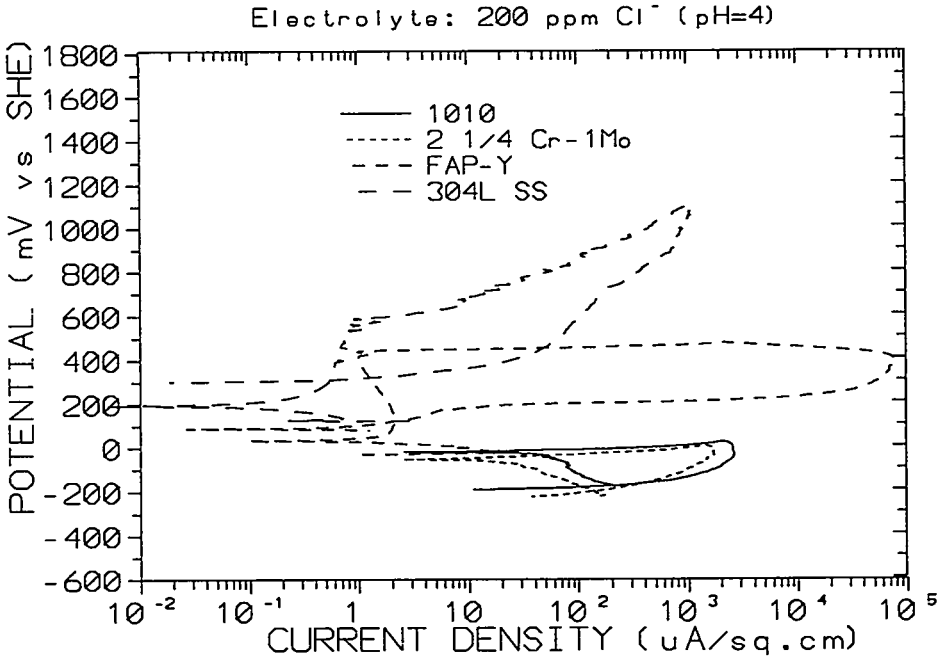

Fig. 3. Cyclic anodic polarization curves in aerated 200 ppm Cl^- (pH=4) solution.

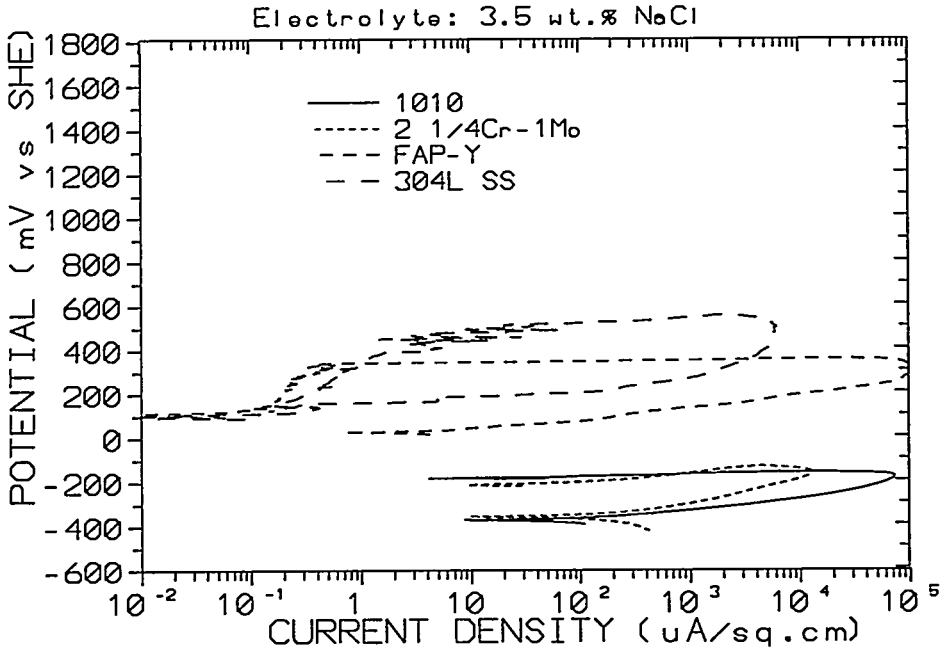

Fig. 4. Cyclic anodic polarization curves in aerated 3.5 wt .% NaCl solution.

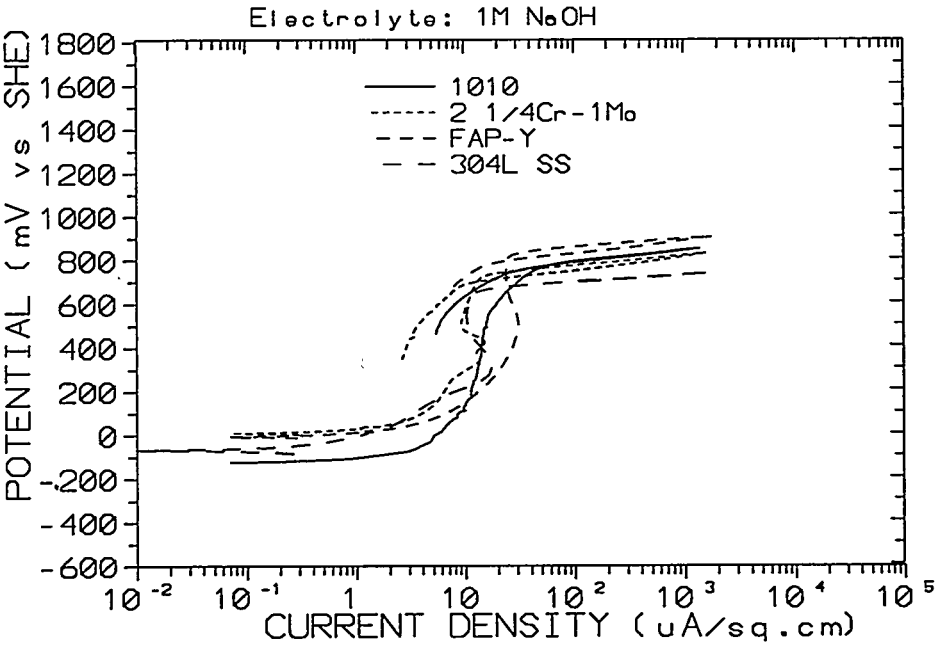

Fig. 5. Cyclic anodic polarization curves in aerated 1N NaOH solution.

Corrosion Rates

Corrosion rates were determined by two different methods: the electrochemical polarization-resistance method, which provided corrosion rates over approximately the first two hours of exposure, and a three-week immersion test method, whereby corrosion rates were calculated from weight-loss measurements and represented three-week-average corrosion-rate values. The same materials and electrolytes were evaluated as described in the previous section on polarization behavior. The results are given in Table 1.

As seen in Table 1, the corrosion rates determined by the polarization-resistance method (initial exposure values) were generally higher than those determined by the weight-loss method (three-week average values), indicating that the corrosion rates decreased with time. In the distilled water, tap water, mild acid-chloride solution, and 3.5 wt. % NaCl solution, the corrosion rates for the FAPY alloy and the 304L stainless steel were similar and much lower than those of the plain-carbon and low-alloy steels. In the highly-basic NaOH solution, the corrosion rates were quite low for all of the materials.

Table 1. Results of corrosion rate measurements.

Solution	Material	Average Penetration Rates (mpy)	
		Polarization Resistance	Three-Week Immersion
Distilled Water	1010	12.1	3.9
	21/4Cr-1Mo	6.3	3
	FAPY	<0.1	<0.1
	304L SS	<0.1	<0.1
Tap Water	1010	0.93	4.5
	21/4Cr-1Mo	1.9	2.2
	FAPY	<0.1	<0.1
	304L SS	<0.1	<0.1
200 ppm Cl^- pH=4	1010	56	4.8
	21/4Cr-1Mo	20	3.6
	FAPY	2.3	<0.1
	304L SS	<0.1	<0.1
3.5 wt. % NaCl	1010	40	3.8
	21/4Cr-1Mo	39	3.2
	FAPY	0.19	<0.1
	304L SS	<0.1	<0.1
1M NaOH	1010	0.53	<0.1
	21/4Cr-1Mo	0.59	<0.1
	FAPY	0.38	<0.1
	304L SS	0.14	<0.1

Crevice Corrosion Behaviors

Three-week crevice-corrosion tests were conducted on the FAPY alloy, and for comparison on the Fe_3Al-based iron aluminide, FAL-Mo, and on 304L stainless steel, using multiple crevice assemblies which formed 60 crevice sites on each specimen. The tests were performed in the mild acid-chloride solution (200 ppm Cl^-, pH=4) and in the 3.5 wt. % NaCl solution. The results are given in Table 2.

In the mild acid-chloride solution, the percentages of crevice sites that underwent active crevice corrosion were 8 % for the FAPY alloy, 0 % for FAL-Mo, and 2 % for the stainless steel. In the higher-chloride 3.5 wt. % NaCl solution, the percentages were 100 % for the FAPY alloy, 8 % for FAL-Mo, and 3 % for the stainless steel. The degree of crevice corrosion increased significantly with increasing Cl^- concentration for the FAPY alloy. Overall, the resistance to crevice corrosion in chloride environments for the FAPY alloy was considerably less than that of the FAL-Mo iron aluminide and the 304L stainless steel.

Table 2. Three-week immersion test results for creviced specimens in 200 ppm Cl^- (pH=4) and 3.5 wt. % NaCl solutions.

Solution	Measurement	Material		
		FAP-Y	FAL-Mo	304L SS
200 ppm Cl^-, pH=4	No. of Crevice Sites Attacked (60 max.)	5	0	1
	Percentage of Sites Attacked	8	0	2
	Max. Depth of Attack (μm)	80	0	4
3.5 wt.% NaCl, pH=7	No. of Crevice Sites Attacked (60 max.)	60	5	2
	Percentage of Sites Attacked	100	8	3
	Max. Depth of Attack (μm)	50	50	4

Slow-Strain-Rate Tests

Slow-strain-rate tests were performed on the FAPY alloy in the mild acid-chloride solution at a strain rate of 1.2×10^{-6} /s at the free-corrosion potential (E_{corr}) and at potentiostatically-

controlled anodic and cathodic potentials. Tests were also performed in air for comparison. The specimens, with gage sections of 12.7 x 1.78 x 0.63 mm, were polished with 600 grit SiC paper after heat treatment and prior to testing. The results are given in Table 3.

The highest slow-strain-rate ductilities for FAPY were observed at E_{corr} and -200 mV(SHE), and these ductilities were comparable to that observed in laboratory air. Embrittlement associated with pitting corrosion occurred at the applied anodic potentials (+300 and +500 mV(SHE)) and embrittlement associated with hydrogen occurred at the applied hydrogen-producing cathodic potentials (-1000 and -1500 mV(SHE)). The slow-strain-rate ductilities for the FAPY alloy (16 % Al) in the mild acid-chloride solution are compared in Figure 6 with those of previously-evaluated FA-84 and FA-129, two Fe_3Al-based iron aluminides (28 % Al). The trends in behavior for all three materials were similar; however, the ductilities at all potentials were significantly greater for the FAPY alloy in comparison to the Fe_3Al-based iron aluminides.

Table 3. Slow-strain-rate test results for FAPY in the mild acid-chloride solution.

Applied Potential (mV vs SHE)	Time to Fracture (hr.)	Fracture Stress (MPa)	Percent Elongation
+500	8.3	110	2.4
	--	--	2.3
+300	20.5	510	3.2
	39.5	607	6.3
E_{corr}	55	634	13.4
	--	--	17.3
-200	59	696	15.0
	43	558	11.0
-1000	26.5	610	4.7
-1500	26.7	552	4.7
	--	--	4.7
Air	34	758	14.2
	--	--	14.2

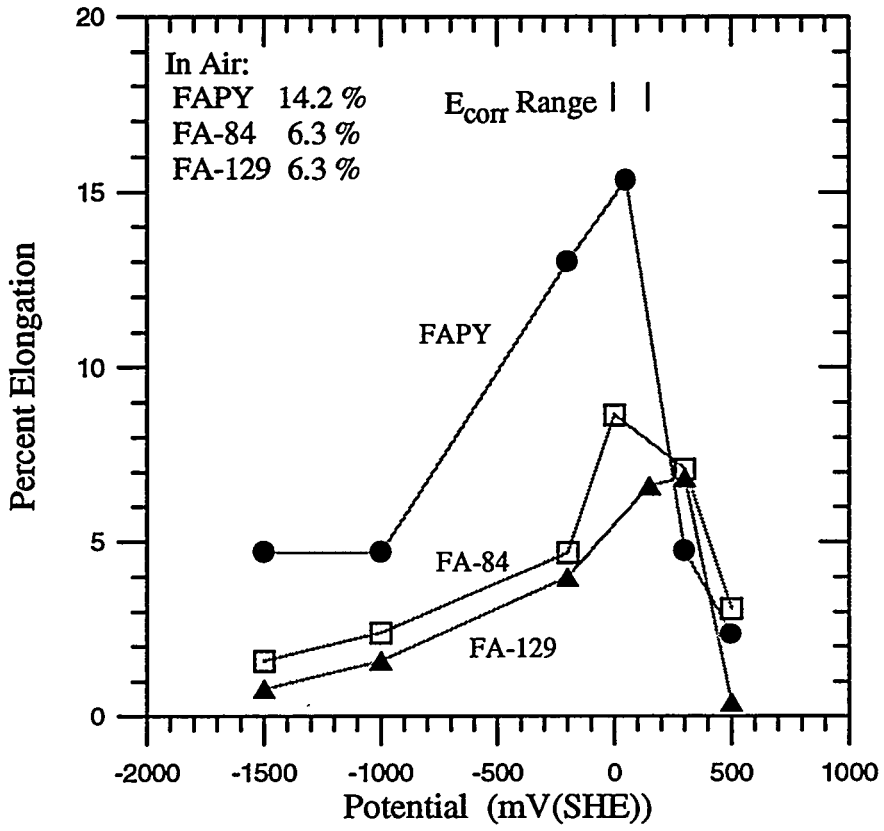

Fig. 6. Ductilities of FAPY, FA-84 and FA-129 under slow-strain-rate conditions in 200 ppm Cl^-, pH = 4 solution as a function of potential.

SUMMARY AND CONCLUSIONS

A low-aluminum-content iron-aluminum alloy developed at ORNL, FAPY (Fe-16.1Al-5.4Cr-1.07Mo-0.11C-0.11Zr-0.06Y, at. %), was evaluated in various electrolytes at room temperature to determine polarization behaviors, corrosion rates, crevice corrosion behaviors, and slow-strain-rate embrittlement characteristics. Reference materials were also evaluated for comparison. The results and conclusions are summarized as follows:

- With regard to cyclic-anodic-polarization behavior, both the FAPY alloy and 304L stainless steel passivated to relatively high potentials in distilled water, tap water, a 200 ppm Cl^- (pH = 4) solution and a 3.5 wt. % NaCl solution, whereas 1010 plain-

carbon steel and 2 1/4 Cr - 1 Mo low-alloy steel underwent only active corrosion. All four materials passivated in a highly-basic 1 N NaOH solution.

- In terms of surface-average corrosion rates, as determined by electrochemical polarization-resistance measurements and weight-loss measurements, the FAPY alloy behaved much more like 304L stainless steel than the plain-carbon and low-alloy steels in the distilled water, tap water and the two chloride solutions. In the NaOH solution, all four materials exhibited very low corrosion rates.

- With regard to crevice-corrosion behavior in a 200 ppm Cl^- (pH = 4) solution and a 3.5 wt. % NaCl solution, the FAPY alloy was found to be less resistant than both an Fe_3Al-based iron aluminide, FAL-Mo (Fe-28Al-5Cr-1Mo-0.08Zr-0.04B, at. %), and 304L stainless steel.

- In terms of slow-strain-rate ductilities in the 200 ppm Cl^- (pH = 4) solution, the FAPY ductility was found to be significantly higher than the two Fe_3Al-based iron aluminides evaluated, FA-84 (Fe-28Al-2Cr-0.05B, at. %) and FA-129 (Fe-28Al-5Cr-0.5Nb-0.2C, at. %), at the free-corrosion potentials and at hydrogen-producing cathodic potentials.

REFERENCES

1. C. T. Liu, C. G. McKamey, and E. H. Lee, "Environmental Effects on Room-Temperature Ductility and Fracture in Fe_3Al," *Scr. Metall. Mater.*, **24**, pp. 385-389, 1990.

2. D. B. Kasul and L. A. Heldt, in *Environmental Effects on Advanced Materials*, ed. R. H. Jones and R. E. Ricker, TMS, Warrendale, PA, 1991, p. 67.

3. N. S. Stoloff, M. Shea, and A. Castagna, in *Environmental Effects on Advanced Materials*, ed. R. H. Jones and R. E. Ricker, TMS, Warrendale, PA, 1991, p. 3.

4. V. K. Sikka, R. H. Baldwin, and C. R. Howell, "Low-Aluminum-Content Iron-Aluminum Alloys," in *Proceedings of the Seventh Annual Conference on Fossil Energy Materials*, CONF-9305135, ORNL/FMP-93/1, Oak Ridge National Laboratory, Oak Ridge, TN, 1993, pp. 197-208.

INTERACTIONS BETWEEN CREEP AND CORROSION IN ALLOY 800*

K. Natesan
Argonne National Laboratory
Energy Technology Division
Argonne, IL 60439

ABSTRACT

Metallic components within or immediately adjacent to gasifiers, such as gas distributors, thermowells, transfer lines, and cyclones, are subjected to particularly severe conditions of temperature, pressure, and hostile multicomponent gas environments. In addition, metallic heat exchangers/waste-heat boilers that are resistant to sulfidation, corrosion, and erosion in low- and medium-Btu gas environments are essential components in large-scale gasification schemes, in both dry ash and slagging type gasifiers. Components, in general, must be resistant to corrosion, erosion, and high-temperature creep. Refractory linings are conventionally employed to mitigate corrosion and erosion, and in some cases, internal cooling has been considered to avoid the problems associated with the interaction of high-temperature creep and fatigue. Contrary to the design situation for vessels and piping, no guidance in the form of a code or standard exists for vessel internals and long-life external components, especially for service in corrosive-erosive environments at elevated temperatures. Designers currently rely on their own stress-analysis techniques and rules and use their experience with petrochemical applications to incorporate the environmental effects in the design of components for coal conversion systems. Such an approach may lead to adequate design, but a substantial data base is needed on the mechanical properties of materials exposed to complex gas environments to provide a more viable basis for establishing long-term reliability of components.

The purpose of the present work is to examine the high-temperature creep behavior of Alloy 800, a high-chromium alloy that is widely used in coal conversion systems, after exposure to oxygen and oxygen/sulfur mixed-gas environments over a wide temperature range. In addition, the data on the creep behavior of the alloy under various pretreatment and test-exposure conditions are used to establish performance envelopes for the alloy for service in fossil energy applications.

BACKGROUND

In general, coal gasification processes result in a complex multicomponent, multiphase mixture, the composition of which depends on several factors such as reaction conditions, type of coal feedstock, coal pretreatment, heat supply, reactor configuration, and gas purification. Furthermore, gasification of coal releases a wide variety of contaminants from coal feedstock, char, ash, and sulfur/chlorine/alkali-containing species. The manner in which these contaminants are released, transported in the gas

---

*Work supported by the U.S. Department of Energy, Office of Fossil Energy, Advanced Research and Technology Development Materials Program, Work Breakdown Structure Element ANL-3, under Contract W-31-109-Eng-38.

phase, and subsequently deposited on relatively cooler metallic surfaces can significantly affect the performance of downstream components.

Corrosion in Gasification Environments

Experimental studies conducted in both laboratory and pilot-plant facilities have clearly established that alloy sulfidation is the major mode of material degradation and that a viable alloy should develop protective oxide scales on exposure to sulfur-containing low-oxygen-partial-pressure atmospheres in coal gasification systems.[1-3] In the early stages of exposure, a high-chromium alloy (typical of structural materials used in gasification systems) develops oxide and sulfide nuclei. Eventually, thermodynamic conditions establish a continuous chromia scale via reoxidation of sulfide particles, while the released sulfur is driven into the substrate along the grain boundaries. Oxide growth occurs via chromium transport across the scale to the scale/gas interface, where it is oxidized, leading to increased thickness. At the same time, sulfur in the gas phase is adsorbed onto the scale/gas interface, and channels are established in the fine-grained oxide scale through which the transport of base-metal cations to the scale/gas interface is accentuated. If the sulfur pressure in the gas phase exceeds the metal/metal sulfide equilibria for the base-metal elements, sulfides of these elements are formed at the oxide scale/gas interface. As the sulfide grows, stresses develop in the oxide scale, which eventually is breached and leads to sulfidation at the oxide scale/substrate interface. Because the transport rates of cations and sulfur through the sulfide phase are orders of magnitude higher than those through the oxide scale, the sulfidation attack continues in an accelerated manner. At longer exposure times, the oxide is virtually destroyed and a massive sulfide scale develops, a condition that represents breakaway corrosion for the alloy. The same sequence of steps is operative in alumina-forming alloys, probably at a much slower rate than in chromia-forming materials. An extensive data base has been developed on the corrosion performance of various of commercial and experimental alloys in a wide range of coal gasification environments.[1-7]

Important factors in assessing the performance of materials are the expected or desired lifetimes of various plant components, ease of repair, and their relative cost. For design studies of conceptual commercial plants, a plant life of at least 20 yr has been assumed for major vessels and piping. For the heat exchanger/recovery systems, a tube life of at least 10 yr is required. For industrial and utility gas turbines, a 100,000-h life is desired. It is imperative that the short-term (up to 10,000 hours) materials performance data be extrapolated to establish corrosion design allowances for components. Such extrapolation is risky because the mechanisms of corrosion can change drastically with time because of the complex nature of the exposure environment and possible excursions or off-normal conditions, leading to irreversible damage, e.g., sulfidation, of the materials. Therefore, it is essential that the materials selected for service possess some degree of tolerance to more aggressive exposure environments and one must develop performance

envelopes that include a wide range of operating conditions under which the component materials will have adequate mechanical properties.

Time-Dependent Mechanical Properties

Very limited information is currently available on the effects of multicomponent gas environments, which are typical of medium-Btu coal gasifiction schemes, on the mechanical properties of structural materials. Uniaxial and biaxial stress-rupture properties of some heat-resistant materials have been evaluated in air and in a gas mixture (containing 0.5 vol.%H_2S), whose composition simulated gases that arise from high-Btu gasification processes.[8,9]

The objective of this work is to evaluate the effect of gas chemistry in the exposure environment on long-term, time-dependent creep properties, and of key variables, such as exposure temperature, applied stress, specimen pretreatment (e.g., thermal aging and preoxidation) on the creep rate, creep life, and metallurgical structure of the material.

EXPERIMENTAL PROCEDURE

Material and Specimen Preparation

Alloy 800, which is widely used in coal-gasification applications, was procured in ≈25-mm-thick flat stock suitable for fabrication of creep specimens. The composition (in wt.%) of the alloy was Fe, 46.6; Cr, 20.7; Ni, 30.4; Al, 0.29; and Ti, 0.41. Creep specimens were designed and fabricated according to ASTM Standard E139-70. All of the creep specimens were solution annealed for 3600 s at 1050°C and water quenched. The grain size of the specimens was ≈100 μm. Some of the annealed specimens were enclosed in Vycor capsules under vacuum, and furnace-aged for time periods of 160, 1000, and 2000 h at 843 and 927°C. In addition, several specimens were preoxidized in low-pO_2 environments for subsequent creep testing in a sulfur-containing environment.

Creep Testing

The creep testing laboratory is equipped with seven direct-load and three indirect-load creep machines, which were used to perform creep tests in air, low-pO_2, and oxygen/sulfur mixed-gas environments. The data acquisition system consists of a VIDAR 606 master scanner, a 502B integrating digital voltmeter, a 5404 system controller, and a teletype. Each of the creep machines is equipped with a high-temperature furnace and a stainless steel or alumina specimen chamber with water-cooled heads at the top and bottom. The test specimen was held in the uniform-temperature zone of the furnace by means of a gripping device that incorporated a split socket and solid clamping ring. Creep strain in the specimens was measured by a linear-variable-differential transducer (LVDT) that was attached between the fixed and movable pull rods of the creep assembly.

Displacements of 5 x 10^{-3} mm could be accurately determined with the LVDT. Before the start of each test, the LVDT was calibrated by measuring its output for displacements that were set manually with a micrometer. The linear portion of the calibration curve Was used to measure the strain in a specimen during creep testing.

A three-zone resistance-heated furnace was used toconduct creep tests at elevated temperatures. Three Chromel-Alumel or platinum-platinum/rhodium thermocouples were fed through the specimen chamber; one was spot welded onto each end of the grips on the specimen near the shoulder region. The third thermocouple was held in the gas phase adjacent to the gauge length portion of the specimen. Temperature was maintained within ±2°C of the desired value for each test. The specimens were loaded at a constant rate to the full load at the test temperature.

Creep Test Environments

Creep tests were conducted in air, 1 vol.%CO-CO_2, and oxygen/sulfur mixed gas environments. In addition, specimens were tested in sulfur-free oxidizing environments for a period of time; subsequently, the gas was changed from an oxidizing to a sulfidizing gas mixture. These latter tests were performed to evaluate the effect, if any, of sulfur in the environment on the fracture of the oxide scales that had developed under load. Table 1 lists the oxygen and sulfur partial pressures of the gas mixtures for several temperatures used in the study.

Table 1. Characteristics of gas environments used in creep tests

Test Environment	Test Temperature (°C)	PO_2 (atm)	PS_2 (atm)
Air	650	0.21	-
	750	0.21	-
	843	0.21	-
	927	0.21	-
1% CO-CO_2	650	1.2×10^{-19}	-
	750	1.9×10^{-16}	-
	843	4.8×10^{-14}	-
	927	3.4×10^{-12}	-
O/S mixed gas	650	1.2×10^{-22}	1.3×10^{-8}
	750	1.2×10^{-19}	1.6×10^{-7}
	843	1.3×10^{-18}	2.0×10^{-7}
	927	7.7×10^{-17}	8.7×10^{-7}
Two-stage*	650	1.2×10^{-19}	1.9×10^{-9}
	750	1.9×10^{-16}	2.0×10^{-8}
	843	4.9×10^{-14}	1.1×10^{-7}
	927	3.4×10^{-12}	4.5×10^{-7}

*In the first stage, specimens were oxidized in the pO_2 values listed, and in the second stage, the specimens were exposed to H_2-H_2S gas mixtures with the pS_2 values listed.

RESULTS AND DISCUSSION

Creep Test Data

Creep strain data were accumulated as a function of test time for all of the specimens tested in this study. The strain-time curves generally did not exhibit a clear demarcation between primary, secondary, and tertiary creep stages. In several cases, the specimens crept at a very slow rate and after a substantial period, the creep process accelerated to failure. Also, in some cases the creep strain-time curves were linear. The nature of the creep strain-time curve was influenced by the test temperature, test environment, specimen pretreatment, and applied stress. However, for a given applied stress, the test environment did not have much effect on the shape of the strain-time curve. Typical results are presented in this section.

Figure 1 shows the creep strain-time curves for specimens tested at 650°C at an applied stress of 137.9 MPa in air, 1 vol.% CO-CO_2, O/S mixed gas, and sequentially oxidizing/sulfidizing environments. The creep curves were analyzed to evaluate creep rates, rupture strain, and time to rupture; the results will be presented in the next section. Figure 2 shows similar data for specimens at 750°C in several test environments. Figures 3 and 4 show creep strain versus time curves for specimens tested at 843°C in several environments at applied stress levels of 55.2 and 27.6 MPa, respectively. Figure 5 shows similar data for specimens tested at 927°C at an applied stress of 17.2 MPa.

Even though the creep strain-time curves are of widely varying shapes, an attempt has been made to evaluate creep rate, which is useful to designers of components for service in coal gasification service. The designers are generally interested in time to accumulate 1 or 5% strain as a function of applied stress and environment, as well as rupture time and strain at rupture. The present data are not amenable to evaluation of time to accumulate 1% strain, primarily because the times to achieve 1% strain are substantially small when

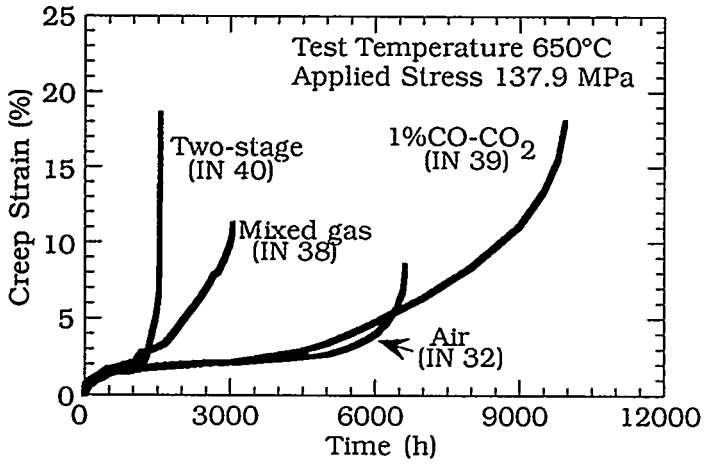

Figure 1.
Creep strain-time curves for specimens tested at 650°C at an applied stress of 137.9 MPa in several gaseous environments. Letters and numbers in parentheses = sample identification.

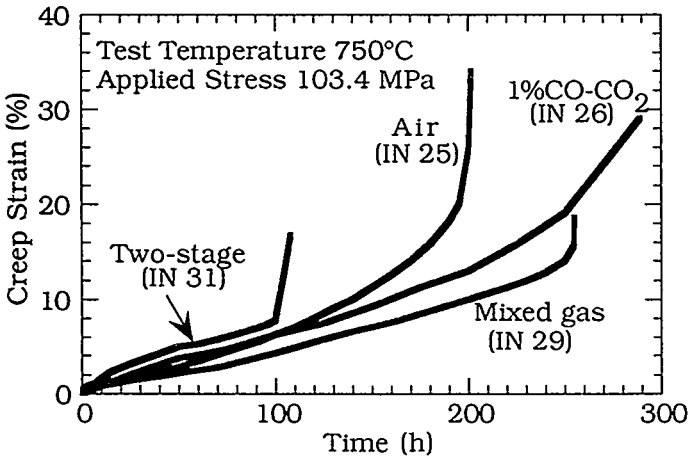

Figure 2.
Creep strain-time curves for specimens tested at 650°C at an applied stress of 137.9 MPa in several gaseous environments. Letters and numbers in parentheses = sample identification.

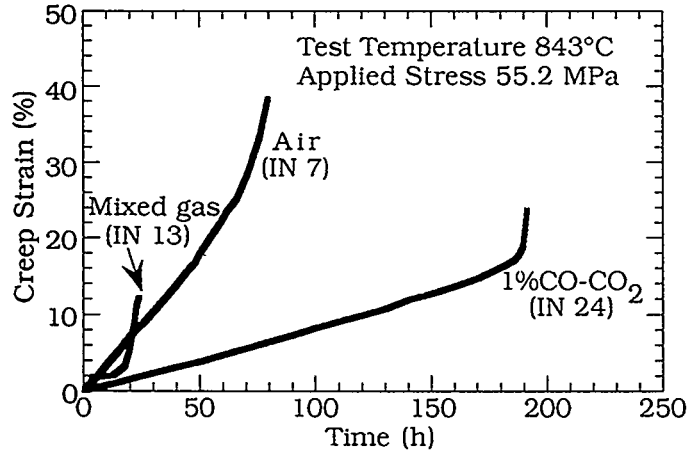

Figure 3.
Creep strain-time curves for specimens tested at 843°C at an applied stress of 55.2 MPa in several gaseous environments. Letters and numbers in parentheses = sample identification.

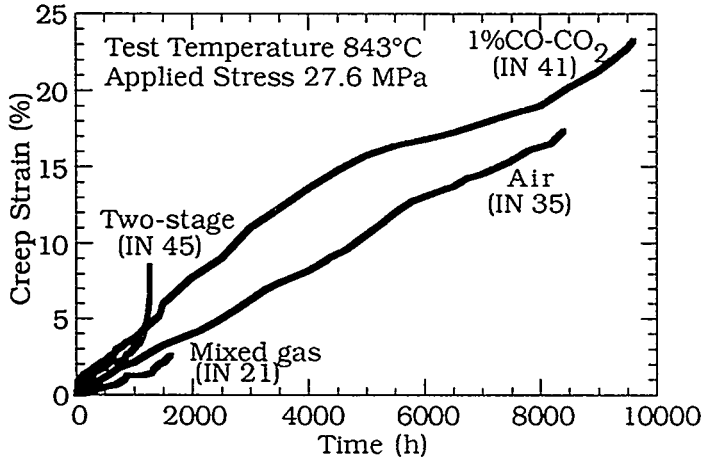

Figure 4.
Creep strain-time curves for specimens tested at 843°C at an applied stress of 27.6 MPa in several gaseous environments. Letters and numbers in parentheses = sample identification.

compared with the total test time. As a result, time values were obtained for accumulation of 5% strain, along with time to rupture and rupture strain. The results for tests conducted at several temperatures and in different gas environments are listed in Table 2.

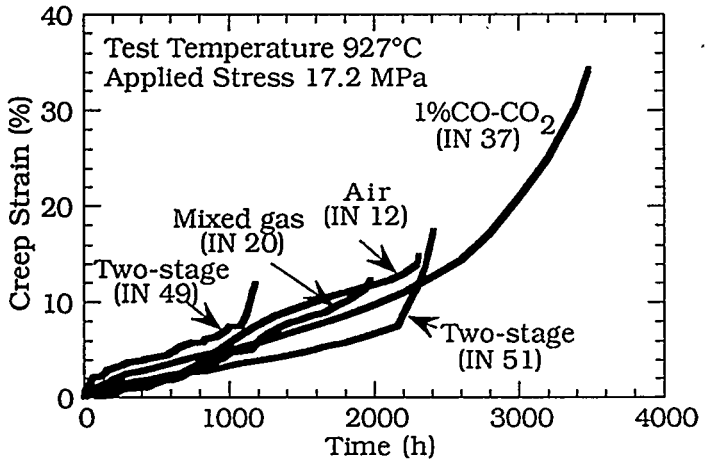

Figure 5.
Creep strain-time curves for specimens tested at927°C at an applied stress of 17.2 MPa in several gaseous environments. Letters and numbers in parentheses = sample identification.

Microstructural Information

Several of the tested specimens were examined in surface and cross section with a scanning electron microscope equipped with an energy dispersive X-ray analyzer. Details developed on some of the typical specimens are presented below. The major focus of the evaluation is to analyze the scaling of the alloy under load in air and low-pO_2 environments in the absence of sulfur in the test environment, evaluate the scaling process under load in O/S mixed gas, and establish the effect of sulfur on the mechanical integrity of the oxide scales developed in sulfur-free environments.

The specimens tested in air and low-pO_2 environments exhibited predominantly oxide scales, the composition of which was influenced by the oxygen partial pressure in the exposure environment. Analysis of cross sections of fracture surfaces showed that air-exposed specimens developed (Fe,Cr) oxide, whereas specimens exposed to low pO_2 developed chromium oxide. Further, the cracked regions in these specimens developed iron-rich oxide rather than chromium oxide. Significant internal oxidation was noted in specimens tested in a low-pO_2 environment.

The specimens tested in O/S mixed gas developed an oxide scale or a sulfide scale, depending on whether pO_2 in the test environment was greater or less than the pO_2 value for the transition boundary (established from corrosion studies) between chromium oxide/chromium sulfide formation. When pO_2 (test) > pO_2 (transition), the alloy develops chromium oxide scale. The alloy can develop a sulfide phase external to the oxide phase, depending on the outward cation transport through the oxide scale. In this case, even the cracked regions of the specimen exhibited oxide scale in contact with the alloy substrate and a sulfide scale on the gas side of the interface. When pO_2 (test) > pO_2 (transition), the alloy develops a massive sulfide scale and the time to rupture of the specimen is substantially reduced. Under these conditions, the alloy becomes embrittled because sulfur diffuses along the grain boundaries in the alloy.

Table 2. Creep test data for specimens tested under different conditions

Test Temperature (°C)	Test Environment[a]	Specimen Number	Applied Stress (MPa)	Rupture Time (h)	Rupture Strain (%)	Average Creep Rate (%/h)
650	Air	33	103.4	14050	12.2	0.00021
	Air	32	137.9	6630.1	8.5	0.00066
	CO-CO_2	39	137.9	9950	18.0	0.00079
	O/S gas	38	137.9	3061	11.2	0.0022
	Two-stage	40	137.9	1560	18.5	0.0023/0.055
750	Air	22	68.9	5165	18.9	0.0017
	CO-CO_2	27	68.9	2416	29.8	0.0105
	O/S gas	36	68.9	2141	13.4	0.0046
	Two-stage	48	68.9	1223	10.2	0.0093/0.019
	Air	28	89.6	324.8	38.5	0.065
	CO-CO_2	43	89.6	473.0	20.3	0.021
	Air	25	103.4	201.8	34.0	0.158
	CO-CO_2	26	103.4	269.4	29.0	0.063
	O/S gas	29	103.4	255.4	18.6	0.043
	Two-stage	31	103.4	108.0	17.8	0.111/1.25
	Air	30	124.1	75.4	35.3	0.335
	CO-CO_2	42	124.1	47.3	27.0	0.300
843	Air	35	27.6	8401	17.4	0.002
	CO-CO_2	41	27.6	9620	23.3	0.0037
	O/S gas	21	27.6	1628	2.6	0.0016
	Two-stage	45	27.6	1275	8.45	0.004/0.028
	Air	8	41.4	620	23.9	0.0146
	CO-CO_2	15	41.4	2697	29.5	0.0042
	O/S gas	18	41.4	618	23.2	0.0463
	Air	7	55.2	79.6	38.3	0.481
	CO-CO_2	24	55.2	191.7	23.7	0.077
	O/S gas	13	55.2	24.2	12.2	0.175
	O/S gas	16	55.2	27.3	8.6	0.171
927	Air	12	17.2	2311	14.8	0.0054
	CO-CO_2	37	17.2	3482	34.3	0.0050
	O/S gas	20	17.2	1975	12.3	0.0047
	Two-stage	49	17.2	1180	11.9	0.0078/0.029
	Two-stage	51	17.2	2412	17.4	0.0032/0.0088
	Air	11	27.6	310.1	19.8	0.027
	CO-CO_2	23	27.6	369.8	26.3	0.023
	O/S gas	17	27.6	473.2	26.3	0.0416
	Air	10	41.4	16.9	38.5	1.65
	CO-CO_2	44	41.4	35.4	33.8	0.954
	O/S gas	14	41.4	6.3	16.8	1.32

[a]Two -stage = Test environment where, in the first stage, specimens were oxidized in low pO_2, and in the second stage, the specimens were exposed to an H_2-H_2S gas mixture.

The corrosion morphologies of specimens tested in two stages, namely oxidation in Stage 1 followed by exposure to H_2/H_2S in Stage 2, were more complex and were influenced by the time of exposure in Stage 1, sulfur partial pressure in Stage 2, and test temperature. Additional tests and more detailed analysis of tested specimens are needed to fully evaluate the performance of Alloy 800 under these conditions. Figure 6 shows the scanning electron microscopy (SEM) photomicrographs of cross sections of Specimens IN 21, IN 41, and IN 45, which were tested in 1%CO-CO_2, O/S mixed gas, and two-stage environmental conditions.

Creep Correlations

Creep data obtained for specimens tested under differing applied stress values and exposure conditions were used to generate correlations between time to rupture, applied stress, and average creep rate for accumulation of 5% strain. Figure 7 shows dependence of average creep rate for 5% strain accumulation at 750 and 843°C on applied stress for tests conducted in different gaseous environments. In general, the creep rates for the specimens were not significantly affected by variation of the test environment. Figure 8 shows dependence of time to rupture at 750 and 843°C on applied stress for tests conducted in different gaseous environments. It is evident that the sulfur-containing environment results in substantial reduction in rupture life of the alloy. The effect is more pronounced if

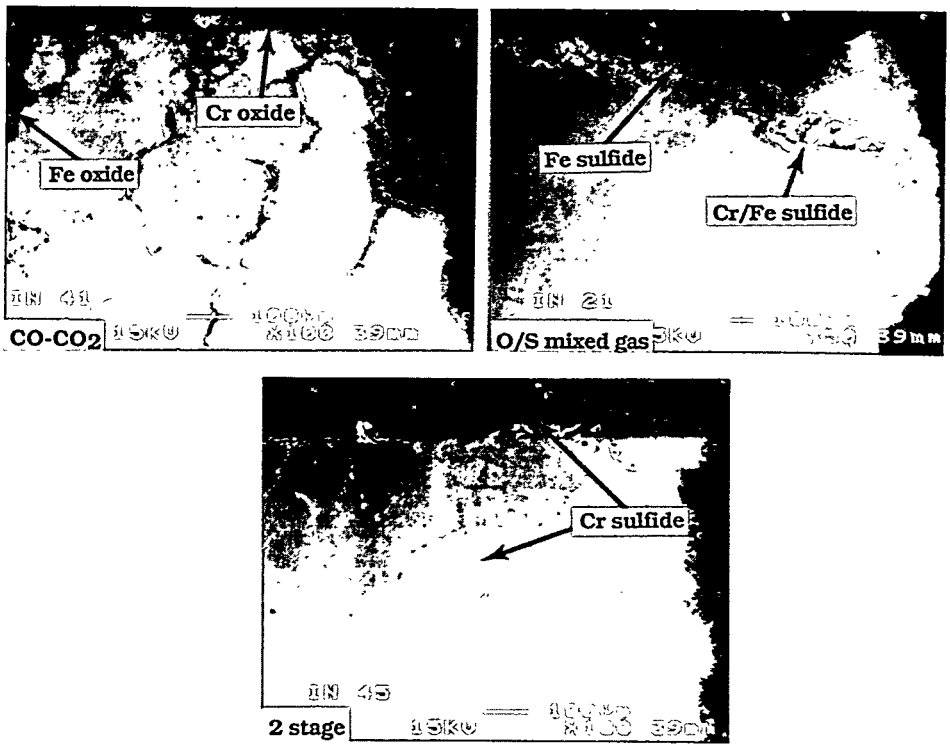

Figure 6. SEM photomicrographs of cross sections of specimens tested in several gaseous environments

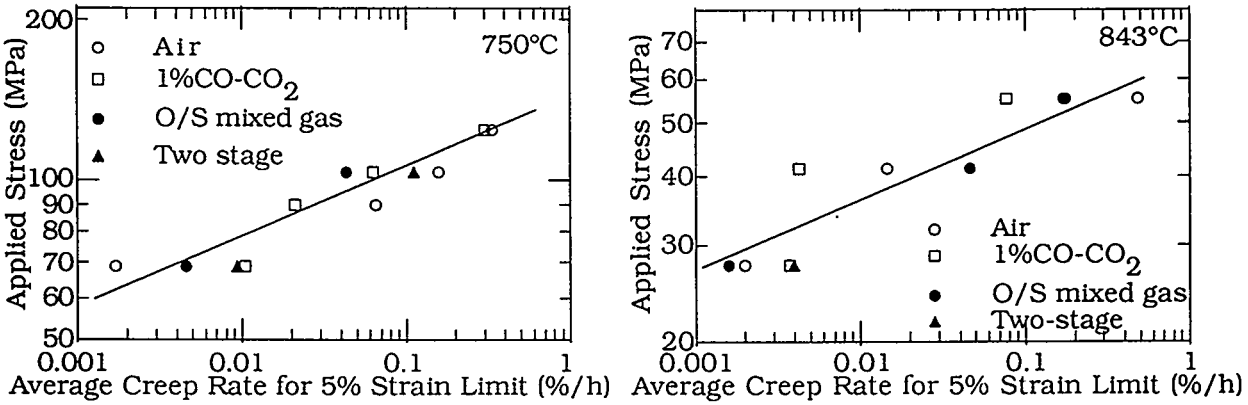

Figure 7. Dependence of average creep rate for accumulation of 5% strain at 750 and 843°C on applied stress, for specimens tested in different environments

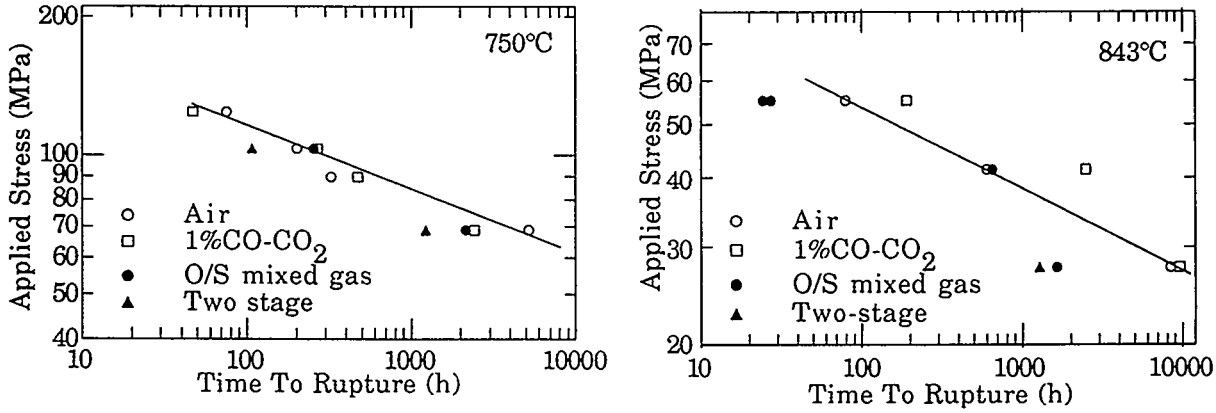

Figure 8. Dependence of time to rupture at 750 and 843°C on applied stress, for specimens tested in different environments

the specimen was preoxidized under load and subsequently exposed to a sulfur containing atmosphere. In the two-stage tests, the original oxide seemed to have been completely destroyed with substantial embrittling of the specimens due to sulfur diffusion in the grain boundaries of the alloy.

Correlations have been developed between rupture time and average creep rate for accumulation of 5% strain, and between rupture time and rupture strain for tests conducted at 650, 750, 843, and 927°C in different gaseous environments. The results indicated that, for a given rupture time, the creep rates are somewhat greater in a sulfur-containing environment than in an environment without sulfur. On the other hand, the rupture stains were substantially smaller in the presence of sulfur, indicating a profound embrittling effect of sulfur in the exposure environment.

SUMMARY

An extensive creep test program was conducted to evaluate the role of sulfur

containing environments on the creep properties of Alloy 800 and to establish the role of sulfur in the scaling process, creep crack propagation, and rupture life. Tests were conducted at 650, 750, 843, and 927°C in air, low-PO_2, O/S mixed-gas environments. In addition, tests were conducted sequentially in a sulfur-free, low pO_2 environment followed by an H_2/H_2S environment. Several conclusions can be drawn from the study.

- In the absence of sulfur in the test environment, the creep properties of the Alloy 800 are improved in low-pO_2 atmospheres when compared with those obtained in air.

- In O/S mixed gas environments, the alloy exhibited minimal effect if pO_2 (test) > pO_2 (Cr oxide/Cr sulfide transition boundary). The alloy exhibited substantial reductions in creep life and creep rupture ductility if pO_2 (test) < pO_2 (transition boundary).

- Average creep rate values for accumulation of 5% strain calculated from creep strain-time data showed negligible effect due to variations in chemistry of test gas atmospheres.

- Extensive microstructural analyses conducted on several of the tested specimens indicated that the creep performance of the materials is predominantly influenced by the corrosion behavior of the alloy in different exposure environments.

REFERENCES

1. K. Natesan, "Corrosion and Mechanical Behavior of Materials for Coal Gasification Applications," Argonne National Laboratory Report ANL-80-5 (1980).
2. T. C. Tiearney, Jr., and K. Natesan, "Sulfidation–Oxidation Behavior of Advanced Metallic Materials in Simulated Low–Btu Coal–Gasifier Environments," Oxid. Met. 17, 1 (1982).
3. K. Natesan, "High–Temperature Corrosion in Coal Gasification Systems," Corrosion, 41, 646 (1985).
4. K. Natesan, "Oxidation of Alloys in Bioxidants," Proc. Symp. Oxidation of Metals and Associated Mass Transport, eds. M. A. Dayananda, S. J. Rothman, and W. E. King, The Metallurgical Society of AIME, Warrendale, PA, October 6-7, 1986, p. 161.
5. R. A. Perkins, W. C. Coons, and S. J. Vonk, "Materials Problems in Fluidized–bed Combustion and Coal Gasification Systems," Electric Power Research Institute Report EPRI-CS-2452 (1982).
6. K. Natesan, "Alloy Performance in Coal Gasification Environments," Proc. Symp. Materials for Coal Gasification. ASM Metals Congress, eds. W. T. Bakker, S. J. Dapkunas, and V. Hill, ASM, Materials Park, OH, 51 (1988).
7. V. L. Hill and B. A. Humphreys, " Proc. Conf. Properties and Performance of Materials in the Coal Gasification Environment, V. L. Hill and H. L. Black, eds., American Society for Metals, Metals Park, OH, 1981, p. 257.
8. U. S. Lindholm and F. F. Lyle, "A Program to Discover Materials Suitable for Service Under Hostile Conditions Obtained in Equipment for the Gasification of Coal and Other Solid Fuels," Metals Properties Council Report, FE-1784-48, ed. A. O. Schaefer (1979).
9. R. M. Horton, "Effect of Simulated Coal Gasifier Atmosphere on the Biaxial Stress Rupture Strength and Ductility of Selected Candidate Coal Gasifier Alloys," Idaho National Engineering Laboratory Report, TREE-1296 (1978).

FUNDAMENTAL STUDY OF ALUMINIZING AND CHROMIZING PROCESS

Ning He, Ge Wang, and Robert A. Rapp

Department of Materials Science and Engineering
The Ohio State University
Columbus, OH 43210

ABSTRACT

For a halide-activated pack cementation process, codeposition of Cr and Si into diffusion coatings on steel surfaces can be achieved by using two halide salts to jointly optimize the partial pressures of $CrCl_2(v)$ and $SiF_2(v)$. The selection of the second salt is the key point for this process. A SOLGASMIX program was used to calculate the equilibrium vapor pressures of different metal halide gas species for different activator salt combinations. Two salts with the same cation develop low partial pressures for $CrCl_2(v)$ and $SiF_2(v)$, which are not high enough to codeposit Cr and Si into a coating. Two salts with different cations produce a different result. Some combinations, such as NaCl and CaF_2, have high and comparable partial pressures of $CrCl_2(v)$ and $SiF_2(v)$. However, other combinations either have low partial pressures, or the partial pressures of $CrCl_2(v)$ and $SiF_2(v)$ are not of the same magnitude. The role of the partial pressure for the alkali metal is elucidated. Experimental verifications are consistent with the theoretical predictions, and thus coated steels exhibit excellent corrosion resistance to cyclic oxidation and aqueous corrosion.

INTRODUCTION

The pack cementation coating process[1] is a self-generated Chemical Vapor Deposition (CVD) process carried out at high temperature to form diffusion coatings which can improve the environmental resistance of steels. The deposition of the individual elements Al, Cr or Si is commonly practiced commercially, but the codeposition of two elements simultaneously suffers an equivalent difficulty as electroplating an alloy, and this process is not commonly practiced. However, the addition of Cr plus Si into a steel surface to change the composition locally can greatly improve the resistance of the alloy to high-temperature oxidizing gases or to an ambient corrosive environment.

Chromium, as delivered by the $CrCl_2(v)$ species, is the main element used in the coating process to improve the oxidation and corrosion resistance of steels. However, as illustrated in Fig. 1 (a), the deposition and diffusion of chromium into steels in which the carbon content is higher than 0.004wt%[2] is limited by the formation of a thin

tendency for alloying. Also, excess binary halide salts are considered to be present in the pack at unit thermodynamic activities so that the initial input amounts do not influence the equilibrium partial pressures of any gaseous species. The initial amount of Ar gas ($1x10^{-4}$ mol) in the pack is chosen using the ideal gas law, but this gas does not enter into any reactions with the components.

In the cementation coating pack, the partial pressures of the silicon fluoride vapors are determined by the activity of the silicon and the halogen gas, e.g., according to the reaction: Si + xF(g) = SiF_x(v). In these systems with high temperatures and low halogen activities, the partial pressures of the atomic halogens exceed those for the molecular species. When the Si metal activity is held constant (unity in this study), the partial pressure of SiF_x(v) is dependent only on the pressure of F(g), which is determined by the decomposition reaction for the halide salt: NaF(s) = Na(v) + F(g). When the activity of NaF(s) is held constant (unity in this study), the pressure of F(g) is linked by an equilibrium constant to the vapor pressure of the Na(v) gas species. Therefore, the partial pressures of the SiF_x(v) species are dependent on the Na vapor pressure in the pack. A similar interdependence describes the relationships between $CrCl_2$(v) and the partial pressures of Na(v) and Cl(g) generated from an NaCl activator salt.

Table I shows the standard Gibbs energies of formation per mole of Cl_2 and F_2 for different metal halide vapors and the halide salts at 1400 K. The thermodynamic calculations for cementation packs with various activators were carried out by using a computer program, SOLGASMIX, evolved from Eriksson[1]. This program is capable of treating the mutual equilibria of multiple condensed phases and a gas phase. Table II shows typical input data for the program and the resulting output (equilibrium) information, in this case for the mutual equilibrium of pure Cr, Si and NaF at 1400K. According to the standard Gibbs energies of formation of all possible compounds in the system (as given in Table I) and the initial molar input of elemental components (given in Table II), the program redistributes the elements to generate the equilibrium partial pressures for the various vapor species at the

Table I. Standard Gibbs Energies of Formation (Kcal/mol) at 1400K

	Kcal/mole Cl_2		Kcal/mole F_2
NaCl	-131.56	NaF	-198.8
KCl	-138.09	KF	-195.06
$MgCl_2$	-101.1	MgF_2	-209.75
$CaCl_2$	-141.7	CaF_2	-238.05
$CrCl_2$(v)	-53.3	CrF(v)	-60.4
$CrCl_3$(v)	-43.9	CrF_2(v)	-116.7
$CrCl_4$(v)	-33.8	CrF_3(v)	-129.2
SiCl(v)	-25.3	SiF(v)	-77.3
$SiCl_2$(v)	-52.4	SiF_2(v)	-150.5
$SiCl_3$(v)	-54.3	SiF_3(v)	-160.1
$SiCl_4$(v)	-57.3	SiF_4(v)	-169.0

Table II. Example Input and Output Data for SOLGASMIX.

T= 1400 K			P = 1.00atm
Input Conditions			
Species			Amounts
Cr (c)			1.800E+01 (gm)
Si (c)			2.000E+00 (gm)
Ar			1.000E-04 (mol)
NaF (c)			1.000E+00 (gm)
C (c)			1.000E-4 (gm)
Al_2O_3 (c)			8.000E+01 (gm)
Output Gas Phase Equilibrium Compositions			
Species	Moles	Mol. Frac	P (atm)
Ar	1.00000E-04	9.72845E-01	9.72845E-01
Na	1.92375E-06	1.87152E-02	1.87152E-02
SiF_4	4.09908E-07	3.98777E-03	3.98777E-03
NaF	2.27212E-07	2.21042E-03	2.21042E-03
Na_2F_2	1.00183E-07	9.74627E-04	9.74627E-04
SiF_3	7.06561E-08	6.87374E-04	6.87374E-04
CO	2.15244E-08	2.09399E-04	2.09399E-04
AlF_3	1.66027E-08	1.61519E-04	1.61519E-04
SiF_2	8.36225E-09	8.13518E-05	8.13518E-05
AlF	5.78462E-09	5.62754E-05	5.62754E-05
SiO	5.53609E-09	5.38576E-05	5.38576E-05
AlF_2	1.74267E-09	1.69535E-05	1.69535E-05
SiF	1.79392E-12	1.74520E-08	1.74520E-08
Al_2F_6	8.57486E-13	8.34201E-09	8.34201E-09
CrF	8.64653E-14	8.41173E-10	8.41173E-10
CrF2	4.49571E-14	4.37363E-10	4.37363E-10
O_2	1.20204E-29	1.16940E-25	1.16940E-25
F_2	2.71406E-32	2.64036E-28	2.64036E-28
Output Condensed Phases			
Species	Moles		Activities
Al_2O_3 (c)	7.85000E-01		1.00000E+00
Cr (c)	3.46000E-01		1.00000E+00
Si (c)	7.11995E-02		1.00000E+00
NaF (c)	2.38176E-02		1.00000E+00
C (c)	9.99785E-05		1.00000E+00
$Na_2Si_2O_5$ (l)	1.82743E-09		1.00000E+00

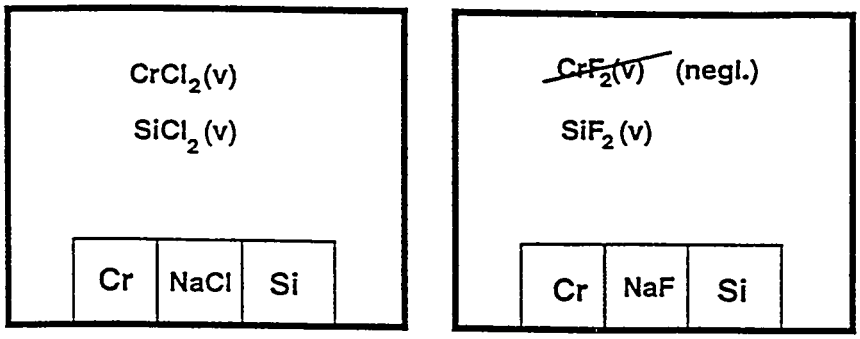

Single Activator Cementation Packs

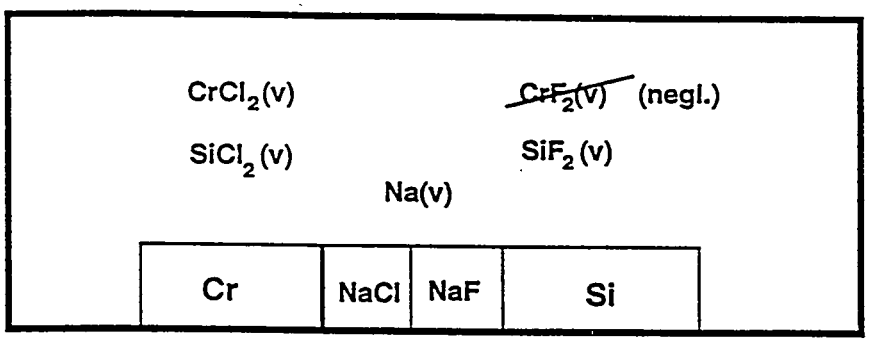

Dual Activator Cementation Pack With "Common Component"

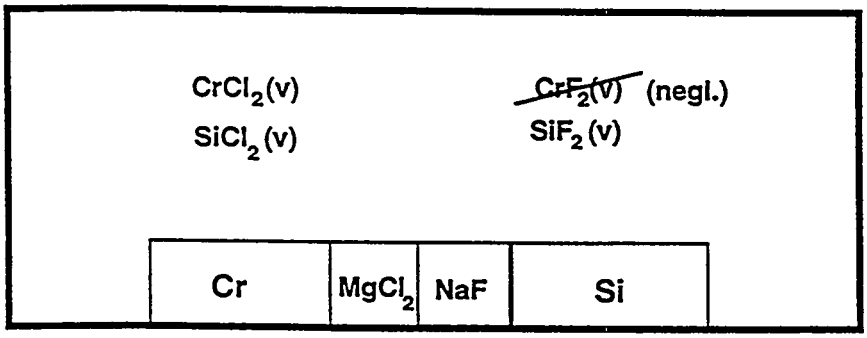

Dual Activator Cementation Pack Without "Common Component"

Fig. 2 Schematic Illustration of Multiphase Equilibria Evaluated to Demonstrate the Importance of the Common Component Effect.

minimum Gibbs energy state. Table II presents the resulting equilibrium vapor pressures; in accordance with the assumptions of unit activities for the pure reactants, the results do not depend upon the amounts of the reactants (in excess). To demonstrate the effect of a common (alkali) component in these multiphase equilibria, the SOLGASMIX program has been evaluated for the conditions shown schematically in Fig. 2.

COMPUTATIONAL RESULTS

Table III shows the calculated vapor pressures of metal halides, and the vapor pressures of halide gases, using a single salt and two salts (with or without a common cation).

Single Salt

According to Table I, NaCl is less stable than KCl, so the partial pressure of atomic chlorine for equilibrium between NaCl with Cr or Si is higher than that for equilibrium with KCl. Therefore, as shown in Table III, the vapor pressures of $CrCl_2(v)$ and $SiCl_2(v)$ using NaCl as a single activator are higher than those using KCl as an activator. An equivalent result is calculated for $MgCl_2$ and $CaCl_2$. The vapor pressures for $CrCl_2(v)$ and $SiCl_2(v)$ using $MgCl_2$ as a single activator are higher than those using $CaCl_2$. However, KF is less stable than NaF, so the partial pressure for $SiF_2(v)$ in the equilibrium for Si with KF is higher than that for the equilibrium of Si with NaF. The vapor pressure of $CrF_2(v)$ is always negligibly small here. Analogous relative vapor pressure behavior occurs for the use of MgF_2 or CaF_2 single salts.

Two Salts (Common Cations)

According to Table III, as a single salt, NaF generates a high sodium vapor pressure (1.86×10^{-2}), much higher than that for NaCl (1.28×10^{-4}). When these two salts are considered for joint use as a mixed activator, the sodium vapor pressure remains the same as that using NaF as a single activator. Therefore, the partial pressures of F(g) and $SiF_2(v)$ are the same as for the use of the single salt NaF. However, because the sodium vapor pressure using the two salts is much higher than that using the single salt NaCl, the partial pressures for

Table III Thermodynamic Calculations of Partial Pressures in Cr-Si-Halide Systems at 1400 K

	Single Salt						
	$P(CrCl_2)$	**$P(SiF_2)$**	**$P(SiCl_2)$**	**P(Cl)**	**P(F)**	**P(M1)**	**Comments**
NaCl	**3.66E-05**		2.66E-05	1.20E-08		Na: 1.28E-4	
NaF		**8.23E-05**			2.76E-14	**Na: 1.86E-2**	High P(Na)
KCl	**1.68E-05**		1.22E-05	8.13E-09		K: 5.83E-5	
KF		**1.08E-04**			3.17E-14	**K: 3.17E-2**	High P(K)
$MgCl_2$	9.34E-05		6.79E-05	1.92E-08		Mg: 1.49E-4	
MgF_2		7.46E-06			8.28E-15	Mg: 1.01E-4	
$CaCl_2$	7.28E-08		5.29E-08	5.36E-10		Ca: 1.44E-8	
CaF_2		3.84E-08			5.96E-16	Ca: 3.75E-8	
	Two Salts (Common Cations)						
	$P(CrCl_2)$	**$P(SiF_2)$**	**$P(SiCl_2)$**	**P(Cl)**	**P(F)**	**P(M1)**	**Comments**
NaCl & NaF	**1.65E-10**	**8.23E-05**	1.20E-10	2.55E-11	2.76E-14	**Na: 1.86E-2**	$P(CrCl_2)\downarrow\downarrow$
KCl & KF	**5.66E-11**	**1.08E-04**	4.11E-11	1.49E-11	3.17E-14	**K: 3.17E-2**	$P(CrCl_2)\downarrow\downarrow$
$MgCl_2$& MgF_2	8.24E-05	4.43E-06	6.00E-05	1.80E-08	6.40E-15	Mg: 1.7E-4	Minor Effect
$CaCl_2$ & CaF_2	4.66E-08	6.39E-08	4.39E-08	4.29E-10	7.69E-16	Ca: 2.25E-8	
	Two Salts (Different Cations)						
	$P(CrCl_2)$	**$P(SiF_2)$**	**$P(SiCl_2)$**	**P(Cl)**	**P(F)**	**P(M1)**	**P(M2)**	**Comments**
NaCl & KF	9.11E-11	2.00E-04	6.62E-11	1.90E-11	4.30E-14	Na:8.09E-2	K:2.34E-2	KF=0.1(mole)
NaCl & CaF_2	**4.17E-06**	**1.02E-05**	3.03E-06	4.05E-09	9.72E-15	Na:3.78E-4	Ca:1.41E-10	
KCl & NaF	**5.47E-10**	**1.00E-04**	3.97E-10	4.64E-11	3.04E-14	**Na:1.69E-2**	**K:1.02E-2**	High P(K) and $P(CrCl_2)\downarrow\downarrow$
KCl & MgF_2	4.75E-07	1.18E-05	3.45E-07	1.37E-09	1.04E-14	Mg:6.35E-5	K:3.46E-4	
KCl & CaF_2	1.62E-06	6.95E-06	1.18E-06	2.53E-09	8.02E-15	Ca:2.07E-10	K:1.88E-4	
$MgCl_2$ & NaF	8.48E-08	6.36E-03	6.16E-08	5.78E-10	5.80E-14	Mg:1.64E-1	Na:8.86E-3	
$CaCl_2$ & NaF	**6.46E-06**	**8.86E-06**	4.70E-06	5.05E-09	9.05E-15	Ca:1.62E-10	Na:3.03E-4	
$CaCl_2$ & KF	5.66E-11	1.08E-04	4.11E-11	1.49E-11	3.67E-14	Ca:1.33E-11	K:3.17E-2	KF=0.05(mole)
$CaCl_2$ & MgF_2	**5.28E-06**	**7.24E-06**	3.83E-06	4.56E-09	8.18E-15	Ca:1.99E-10	Mg:1.03E-4	

* P(Cl) and P(F) refer to the vapor pressures for the atomic vapors of the halogens, which exceed their molecular vapor pressures

** P(M1) and P(M2) refer to the vapor pressures for the atomic vapors of the alkali or alkaline earth metals

Cl(g), $CrCl_2$(v) and $SiCl_2$(v) using two sodium salts are lowered by 3 to 4 orders of magnitude compared to the use of the single salt NaCl. An analogous result happens for the same reason for KCl plus KF (salts with a common cation); the partial pressures for Cl(g), $CrCl_2$(v) and $SiCl_2$(v) are greatly reduced.

The vapor pressures for Mg in packs involving either MgF_2 or $MgCl_2$ as a single activator differ only modestly. Therefore, when both MgF_2 plus $MgCl_2$ are used as dual activators, the vapor pressure of Mg is close to that using either single salt. Therefore, the partial pressures for Cl(g), $CrCl_2$(v), $SiCl_2$(v), SiF_2(v) and F(g) using the two Mg salts are approximately the same as those using a single salt.

Two Salts (Different Cations)

When two salts with different cations are used together as activators, the resulting partial pressures for Cl(g), $CrCl_2$(v) , $SiCl_2$(v) , SiF_2(v) and F(g) follow certain trends. For instance, when NaF plus KCl are used together, the resulting partial pressure for K is 1.02×10^{-2} (more than 2 orders of magnitude higher than that using single KCl); the partial pressure of Na is 1.69×10^{-2} (little change from using the single NaF salt). Therefore, the resulting partial pressures for SiF_2(v) and F(g) are approximately the same as those using single NaF, but the vapor pressures for Cl(g), $CrCl_2$(v) and $SiCl_2$(v) are about 3 to 4 orders of magnitude lower than those using the single KCl salt. Other salt combinations follow the same rules and trends.

From an engineering standpoint, the codeposition of 25Cr and 3Si into steel in a single cementation pack process involves the practical problem of boosting the vapor pressure of $CrCl_2$(v) to compete with SiF_2(v) and $SiCl_2$(v). Table III offers some promising possibilities for the use of two activator salts with different cations. For example, the dual salt activators NaCl + CaF_2, KCl + CaF_2, $CaCl_2$ + NaF, and $CaCl_2$ + MgF_2 might be useful for codepositing Cr and Si, because they generate vapor pressures for $CrCl_2$(v) and SiF_2(v) of comparable and sufficiently high magnitudes.

Even though different cation salts were used in the calculation, a common component still exists in the pack. Si used as the metal source is likely to become the common cation when it reacts with the activator salts to form both its own chloride and fluoride of comparable partial pressures. In the cases studied in Table III, Cr indeed is not the common component, since Cr fluoride species are always negligible. The inherent Si common component leads to a lower Cr chloride vapor pressure than the single salt situation, although salts with a common cation are not intentionally used. Actually, during the pack cementation process, a somewhat higher process temperature than 1400 K is used. Naturally, reactions among the condensed reactants will nullify the assumption of unit thermodynamic activities, but the calculated trends and underlying interpretations should prove to be a useful basis for planning experiments.

EXPERIMENTAL VERIFICATION

Experiments were conducted in an electric resistance tube furnace in an Ar atmosphere. The packs tested contained 20wt.% Cr, 2wt% Si, and 2wt.% various activator salt(s). Alumina was used in the pack as the inert filler, and an interstitial-free iron was used as the metal substrate. The powder mixtures were mixed thoroughly in a ball mill. The powder and the metal substrate were then charged into an alumina crucible, covered with an alumina lid, sealed with a ceramic adhesive, cured in a hot (100°C) oven, and placed in the electric resistance furnace. The furnace was heated to 1150°C for 8 hrs, and then cooled to room temperature. The metal coupons were retrieved, and cleaned ultrasonically in both hot water and acetone. The surface compositions of the coatings were measured using Energy Dispersive Spectroscopy (EDS) analysis. The coating surface compositions as a function of the calculated chromium chloride vapor pressure are plotted in Fig. 3. The surface chromium concentration increases with an increase in the calculated chromium chloride vapor pressure. This fact indeed demonstrates that during chromizing/siliconizing the deposition of chromium is controlled by the vapor transport of the halide species.

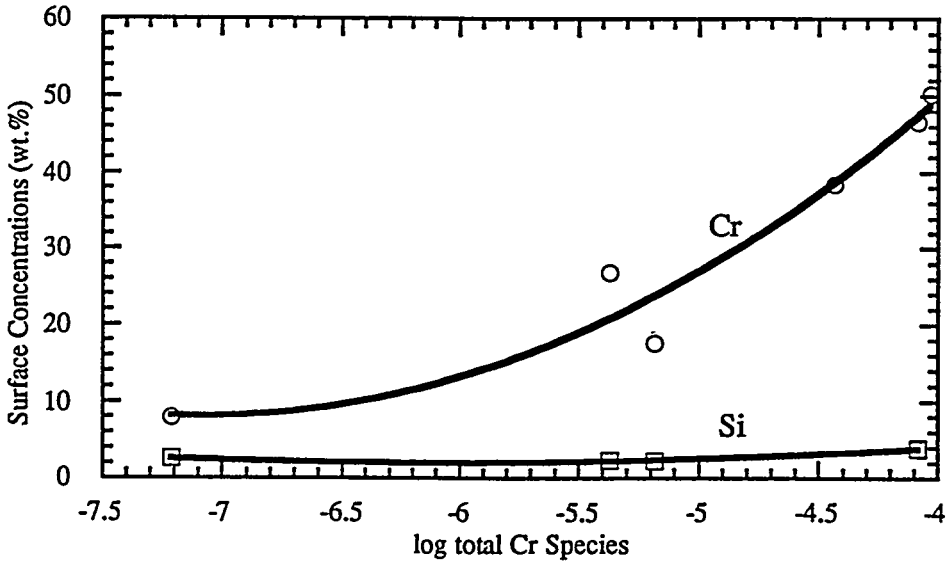

Fig. 3 Coating Surface Concentrations as a Function of the Calculated $CrCl_2$ Vapor Pressure.

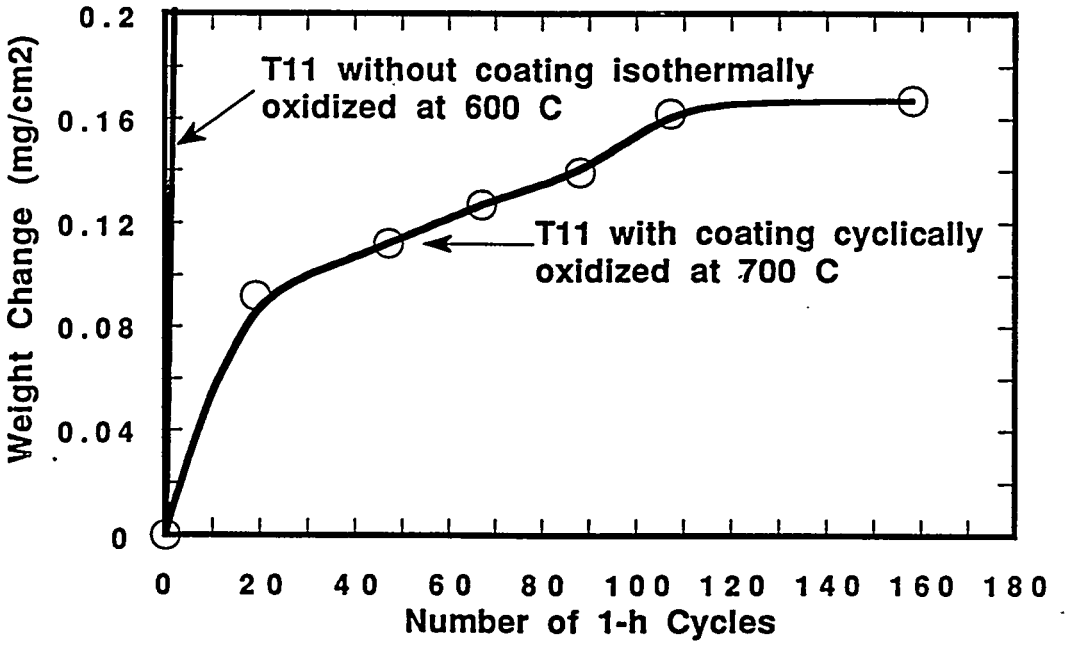

Fig. 4 Cyclic Oxidation Kinetics of a Cr-Si Coated T11 Steel (2.25Cr-1Mo) at 700°C.

TECHNOLOGICAL SIGNIFICANCE

Chromized-siliconized T11 steel with a surface composition of 25 wt.%Cr and 3wt% Si was subjected to a cyclic oxidation test at 700°C. Figure 4 shows one example of the tests. An extremely low weight gain (0.162 mg/cm^2) was recorded after 160 1-h cycles. The same coating principle was also applied to improve the aqueous corrosion resistance of interstitial-free iron and stainless steels. Figure 5 shows the electrochemical polarization curves of the interstitial-free iron and a 316L stainless steel in a 0.6M NaCl/0.1M Na_2SO_4 solution at room temperature, measured before and after chromizing/siliconizing. The coated steels exhibit higher transpassive potential (pitting potential) and a wider passivation region than the original steels.

CONCLUSIONS

For the practical codeposition of Cr and Si into steels in a halide-activated cementation pack:

1. The use of two salts with common cations as activators, e.g. NaCl + NaF, or KCl + KF, results in relatively low partial pressures for Cl(g), $CrCl_2(v)$ and $SiCl_2(v)$, so that Cr could not be deposited into the steel surface.

2. The dual use of two salts with different cations produces differing results. Some combinations (e.g. NaCl + CaF_2) show relatively high partial pressures for both $CrCl_2(v)$ and $SiF_2(v)$ that are also comparable in magnitude, an important condition for codeposition in a single process step.

3. Most combinations of two salts with different cations are not promising, because they either have relatively low partial pressures for $CrCl_2(v)$, $SiCl_2(v)$ and $SiF_2(v)$ or the partial pressures of $CrCl_2(v)$ and $SiF_2(v)$ are not comparable.

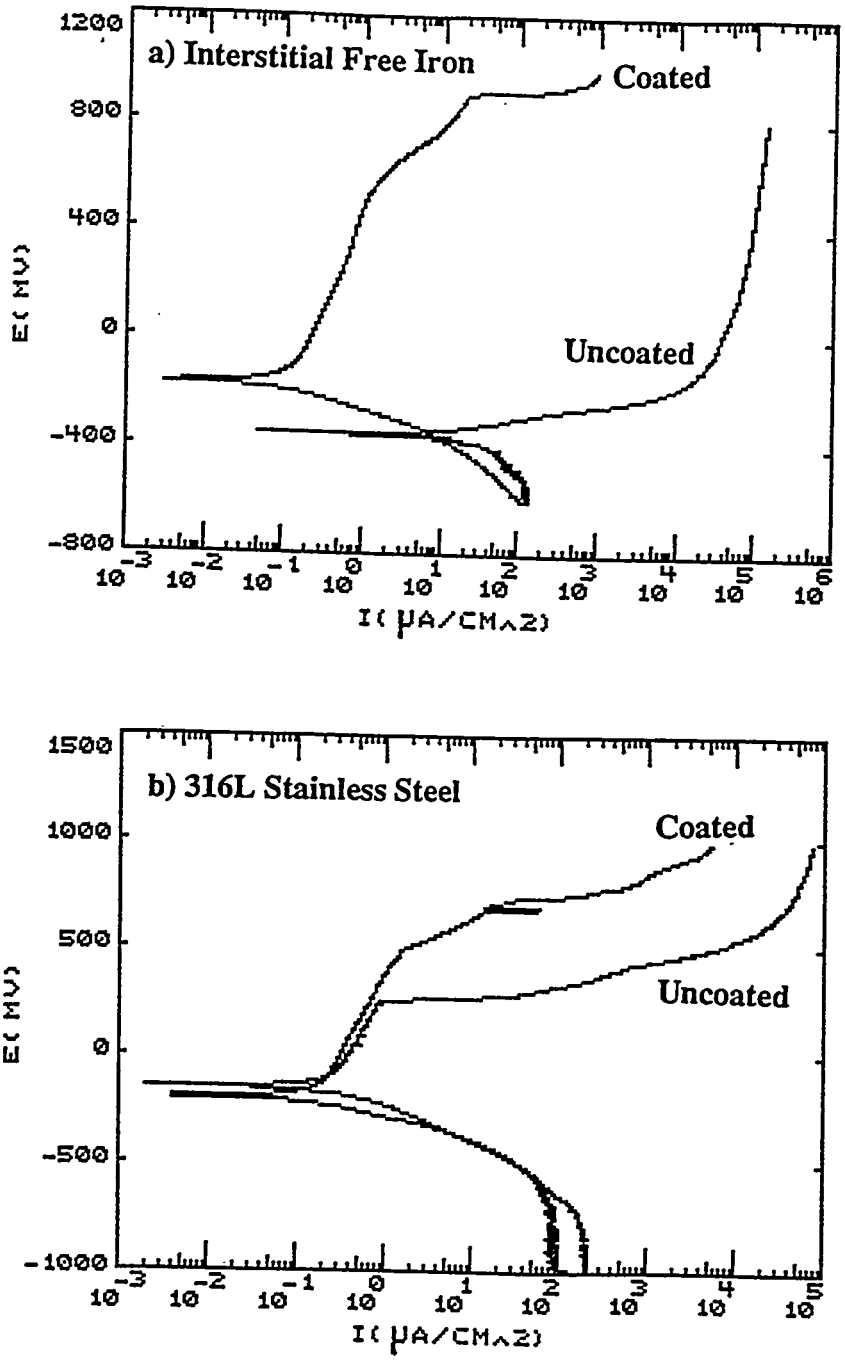

Fig. 5 Electrochemical Polarization Behavior of a) Coated Interstitial Free Iron and b) Coated 316L Stainless Steel in a 0.6M NaCl/0.1M $Na_2(SO_4)$ Solution (pH = 8) at Room Temperature.

4. In the multicomponent multiphase equilibrium considered, the high partial pressures for the atomic alkali metal vapors are important in deciding the effects of the common component.

5. Chromized-siliconized T11 steel demonstrates extremely slow cyclic oxidation kinetics at 700°C. The chromized/siliconized coating also greatly improves the pitting resistance of stainless steels.

REFERENCES

1. R. Bianco, M. A. Harper and R. A. Rapp, *J. Metals*, **Vol. 43** (1991), pp. 20-25.

2. K. Jyrkas, *Surface Engineering*, **Vol. 7** (1991), pp. 239-249.

3. M. A. Harper and R. A. Rapp, *The First International Conference on Heat-Resistant Materials*, K. Natesan and D.J. Tillack eds., (ASM Int., Materials Park, OH), (1991), pp. 279-288.

4. S. C. Kung and R. A. Rapp, *Oxid. Metals*, **Vol. 32**, (1989), pp. 89-109.

ACKNOWLEDGEMENT

This study is supported by DOE project 19X-SB154C of the Fossil Fuel Materials Program of the Oak Ridge National Laboratory (Dr. Rod Judkins, Project Monitor).

DEVELOPMENT OF A MODIFIED 310 STAINLESS STEEL

R. W. Swindeman

Oak Ridge National Laboratory
P. O. Box 2008
Oak Ridge, Tennessee, 37830

ABSTRACT

Structural materials performance requirements were re-evaluated for use in emerging fossil energy applications. Concepts included low emission boilers, advanced steam cycle, and combined-cycle technologies. Both pressure-bearing and non-pressure-bearing applications were considered. The adequacies of martensitic and austenitic steels were examined, and comparisons of the potential of various alloy selections were undertaken. Both austenitic and martensitic steels were judged to have applicability for boilers operating at 600°C while fine-grained austenitic alloys were judged to be best for service to 650°C. For applications in the range 650 to 760°C, modified 310 stainless steels were judged to be good choices. Above 760°C, the alloys being considered for pressurized fluidized bed combustors (PFBCs) included oxidation-resistant stainless steels. For carbonizers and gasifiers operating below 900°C, cobalt-bearing alloys and modified 310 stainless steels were of interest. Iron-aluminide cladding was also considered, and experimental studies were begun to examine compatibility with pressure boundary materials. The data base for modified 310 stainless steels was expanded to 1038°C, and testing times ranged to beyond 10,000 h. The performance of weldments in modified 310 stainless steel was examined and found to be adequate to enable the use of the material at 871°C. Exploratory work on fatigue was undertaken. For service above 900°C, exploratory evaluations of cast high alloys (HP) and alloy 160

were begun. Creep, fatigue and crack growth testing was initiated on alloy 160. Interactions and collaboration with industry were maintained.

INTRODUCTION

The need for more efficient coal combustion was identified ten years ago, when research on advanced steam cycle concepts was begun by the Electric Power Research Institute (EPRI) to improve the performance of pulverized coal power plants (1). The initial thrust of the FE/AR&TD alloy development research was to evaluate austenitic alloys that could be used for superheater tubing in the boiler of the EPRI Phase 2 conceptual plant (2). Such a plant, producing steam at 650°C and 35 MPa (1200°F and 5000 psi), was expected to be more efficient than existing plants and have lower emissions. The EPRI Phase 2 effort received very little support by the U.S. utility industry. Rather, state-of-the-art combined-cycle concepts and second-generation combined cycle concepts received increased attention from a few enterprising utilities, the EPRI, and the DOE energy technology centers (3). Recognizing that issues remained regarding the use of materials for second-generation combined-cycle systems, efforts undertaken in the last year to collaborate with the fossil power industry in various areas of structural materials technology. Topics that are covered included structural alloys for low emission boilers, advanced steam cycle, and second-generation combined cycle applications that incorporated gasifiers, carbonizers, fluidized bed combustors, and indirect heaters.

LOW EMISSION BOILERS

Low emission boilers (LEB) are being designed with steam temperatures in the range of 593 to 649°C (1100 to 1200°F), and pressures could be as high as 35 MPa (5000 psi) (4). Choices must be made regarding the materials of construction. Both ferritic and austenitic alloys are being considered. Main steam line piping, reheat piping, and headers will be thick-wall components.

Candidate materials include martensitic steels such as Gr91, NF616, and MCM12 and austenitic steels such as 316N and 347H stainless steels. Although base metal properties of these alloys appear to meet the needs for the expected service, issues remain regarding the performance of weldments. A small research effort at ORNL has been directed at examining the performance of weldments under creep rupture and fatigue loadings. Collaboration with utilities and component manufacturers has been part of this effort. Exploratory creep-rupture and fatigue testing of cross welds taken from heavy wall pipe of Gr 91 revealed much reduced life as a result of weakness in the heat affected zone of the welds. The reduced life is expected to be less significant at lower stresses, but long-time testing has yet to be performed. More severe losses are expected in NF616 and MCM12 weldments because of high strength levels in the base metal and their tendency to form a brittle Laves phase.

Recuperator temperatures in some LEB designs are as high as 649°C (1200°F). Some recuperator designs call for thin-section oxidation-resistant steels alloys. Candidates include modified 300 series stainless steels, modified alloy 800H, and nickel base alloys. Research undertaken to support the advanced steam cycle may be applicable to such LEB recuperators, and a small effort is underway to address this issue. An understanding of weld metal and weldment behavior at long times is essential for reliable design of LEB components, so research on weldments that was related to the advanced steam cycle has continued with this new application in mind. Cross-weld tests on modified alloy 800H have been underway, and creep testing times exceeding 25,000 h have been achieved at temperatures in the range of 600 to 700°C (1112 to 1292°). Both fine grain and medium grain size materials are being examined.

SECOND-GENERATION COMBINED-CYCLE

Materials and design methods for second-generation combined-cycle (SGCC) plants were examined. However, many different concepts for SGCC

exist, and materials performance requirements differ greatly from one concept to another. Fluidized bed combustors, carbonizers, gasifiers, and slagging combustors are all being considered in the coal combustion or conversion processes. Heat recovery and gas cleanup systems also vary. In spite of heavy usage of refractories and structural ceramics, it seems likely that metals will be needed for pressure retention, cyclones, gas stream piping liners, expansion bellows, filter supports, blowback systems, and heat recovery tubing. The material selection for these components will depend on the temperature, composition, and alkali corrosion potential of the gas stream.

Materials and design methods for SGCC systems were examined, and, in a collaborative effort with industry, criteria for design at high temperatures were studied (5). Concomitant with the study of criteria, exploratory mechanical testing was undertaken of candidate materials. Some alloys were provided by industry. Materials included alloy 800H, alloy 333, alloy 556, HR-160, modified HP, and stainless steels such as 309S, 310S, and 253MA. Also, the potential of modified type 310 stainless steel for fossil energy applications at temperatures above 815°C was assessed, and it was concluded that a 25Cr-20Ni steel having a strength comparable to alloy 800H would be of commercial interest. Two commercial heats of 310HCbN stainless steel tubing for testing. One experimental heat of a Ta-modified 310 stainless steel (310TaN) was procured as plate and included in the experimental investigations.

In Fig. 1, a comparison is shown of the creep curves for a few alloys of interest at 927°C and 25 MPa (1700°F and 3.63 ksi). It may be seen that the 310TaN stainless steel is substantially more creep resistant than 309 and 253MA stainless steels. Improved creep resistance over alloy 800H is also noted. Further comparisons are provided in Figs. 2a and 2b. Here, the strength to produced rupture in 10,000 h is compared for temperatures in the range of 760 to 982°C (1400 to 1800°F). The 310TaN stainless steel has more than twice the strength of 310 stainless steel and is substantially stronger that 253MA and RA85H over the entire temperature range (Fig. 2a). Depending on

the temperature, the 310TaN stainless steel is equivalent to or stronger than RA333 and alloy 811 and approaches the strength of alloy 556 above 900°C. Testing of 310TaN has been extended to beyond 10,000 h, and data for a number of temperatures and stresses have been correlated on the basis of the Larson Miller parameter. Such a correlation is shown in Fig. 3 where a parametric constant of 15 has been used to collapse the data to a single curve for all temperatures. A few tests on specimen from welds in 12.5-mm plate were also tested under creep conditions. These data are compared to base metal data in Fig. 4, which plots log stress versus the Larson Miller parameter. All specimens were cross welds, but two types of welds are represented. Alloy 556 filler metal was used to produce gas tungsten arc welds, and alloy 117 electrodes were used to produce shielded metal arc welds. Weldment rupture lives fell near the parametric curve for base metal. An autogenous weld was produced in sheet of the material and tested for formability. Small radius bends

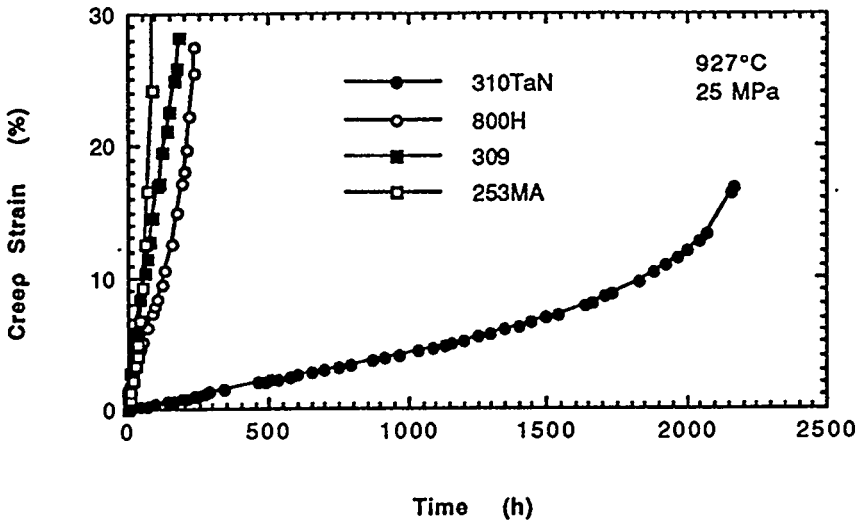

Fig. 1. Comparison of the creep curve for 310TaN stainless steel with curves for three structural alloys at 927°C and 25 MPa.

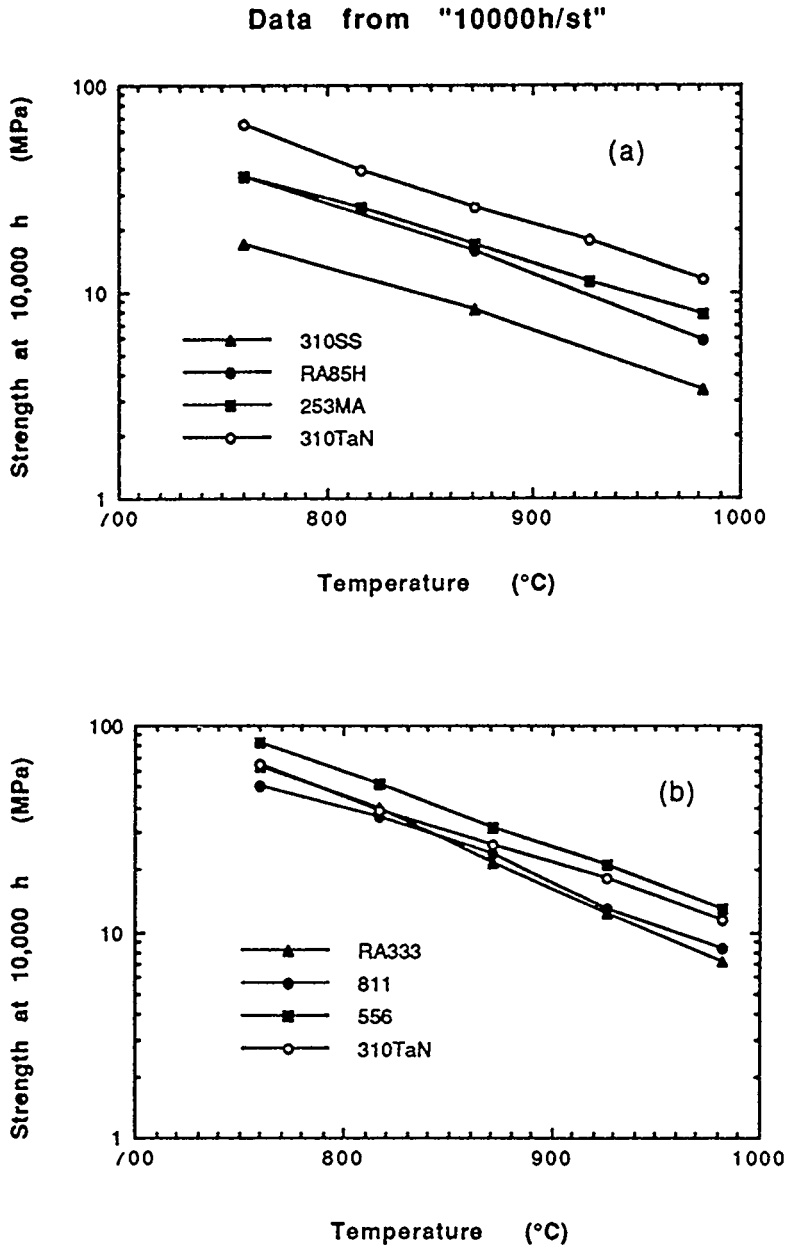

Fig. 2. Comparison of the strength at 10,000 h versus temperature for 310TaN stainless steel with (a) other stainless steels and (b) alloys 333, 556, and 811.

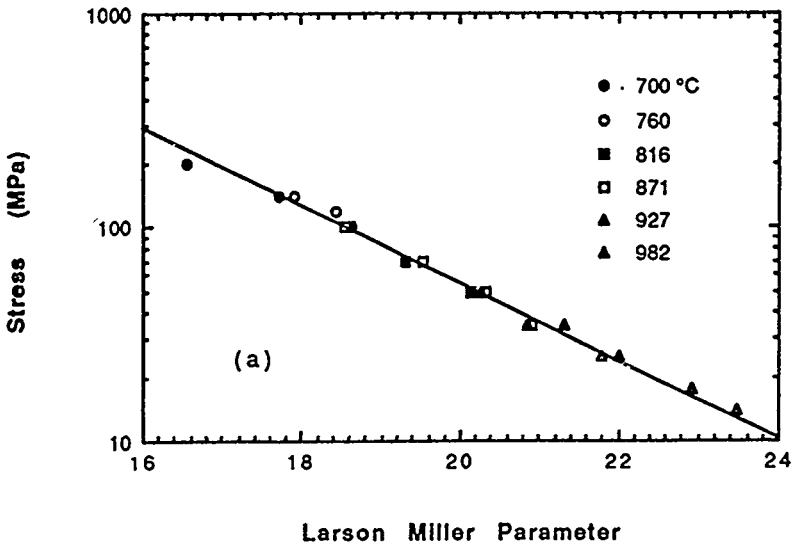

Fig. 3. Stress versus the Larson Miller parameter for rupture of 310TaN stainless steel.

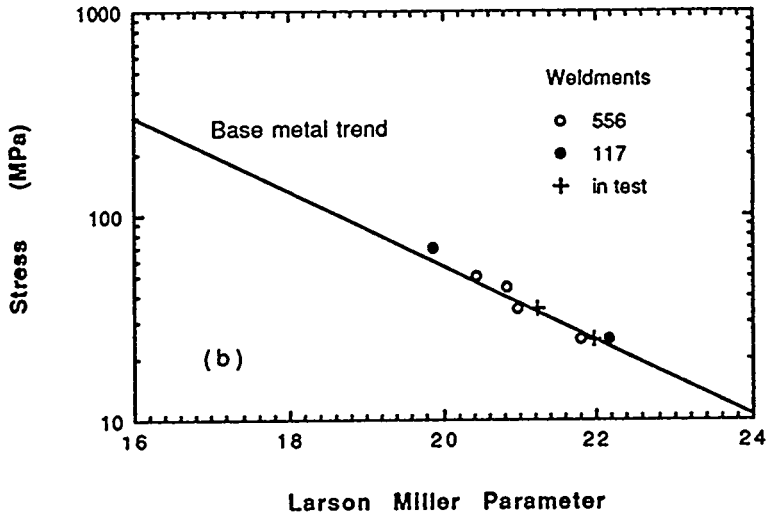

Fig. 4. Stress versus the Larson Miller parameter for rupture of cross welds in 310TaN stainless steel plate using alloys 556 and 117 as filler metal.

were made with no evidence of cracking. A few fatigue tests were performed around 816°C. Data indicated fatigue resistance was similar to other stainless steels. A few tensile tests were performed on aged samples. These tests reveal some loss in ductility, but room temperature elongation remained around 20%. Additional aging studies are in progress. A few oxidation studies were undertaken and results indicated that the oxidation rates for 310TaN stainless steel were similar to 310 and 310HCbH stainless steels at 870°C.

For protection against sulfidizing environments, an examination of the potential of iron-aluminide as a cladding material was explored (6). Coextrusion were made with iron-aluminide on type 310 and 310 stainless steels. Samples from these extrusions are being exposed to thermal cycling and aging.

An evaluation of the design and analysis of structural components in hot-gas cleanup systems was undertaken several years ago. Emphasis at that time was on the tubesheet that supported ceramic filters. Because of the low yield strengths of commercially available high temperature structural alloys, tubesheet alloys were judged to be susceptible to low-cycle fatigue failures under restrained thermal cycling conditions. A nickel-chrome-aluminide intermetallic alloy (cast IC 396M) with a very high yield strength was selected as an alternative material for tube sheet construction. A database was gathered on IC 396M sufficient for an elastic-plastic-creep analysis, and a re-analysis of the critical region of the tubesheet was performed (7). It was found that the high-strength intermetallic alloy would not be an improvement over commercial wrought alloy in regard to thermal fatigue resistance.

SUMMARY

Progress has been made on the evaluation of structural materials for a number of fossil energy applications, and most of the research involves collaborative efforts with industry. The materials and research thrusts were selected to meet the needs of industrial participants in advanced fossil energy projects. For low emmision boilers, most materials of interest are either

commercial or near-commercial in regard to fabrication technology. For construction of components in second- generation combined cycle applications were examined, and emphasis was placed on gathering data needed for establishing design methods and analysis procedures.

REFERENCES

1. S. B. Bennett, *Engineering Assessment of an Advanced Pulverized Coal Power Plant,* EPRI CS-2555, Electric Power Research Institute, Palo Alto, CA, August 1982.

2. R. W. Swindeman, et al., *Alloy Design Criteria and Evaluation Methods for Advanced Austenitic Alloys in Steam Service*, ORNL-6274, Oak Ridge National Laboratory, Oak Ridge, TN, 1986.

3. R. A. Bajura and H. A. Webb, "The Marriage of the Gas Turbines and Coal," *Mechanical Engineering*, pp. 58-63, September, 1991.

4. L. A. Ruth, "Combustion 2000, Clean, Efficient Power for the Future," paper presented at the *International Symposium on Improved Technology for Fossil Power Plants-New & Retrofit Applications*, Washington, D.C., 1993.

5. R. W. Swindeman and D. L. Marriott, "Criteria for Design with Structural Materials in Combined-Cycle Applications Above 815°C," paper 93-GT-203, International Gas Turbine and Aeroengine Congress and Exposition, Cincinnati, OH, May 24-27, 1993.

6. R. W. Swindeman, Summary of Work on Coatings and Claddings for Fossil Energy Applications, ORNL/TM-12367, Oak Ridge National Laboratory, Oak Ridge, TN, May 1993.

7. R. H. Mallett, *Creep-Fatigue Damage Analysis for a Hot Fluegas Vessel Tubesheet of Nickel-Chromium Aluminde Material*, MSTI-TR-756, Mallett Technology, Inc., August, 1993.

INVESTIGATION ON THE WELDABILITY OF HIGH TEMPERATURE ALLOY TUBING MATERIALS

C.D. Lundin and C.Y.P. Qiao

Materials Joining Research
Materials Science and Engineering
The University of Tennessee, Knoxville

ABSTRACT

Gleeble hot ductility, Varestraint hot cracking and Finger hot cracking evaluations on thick wall commercial 310HCbN tubing material agree with and verify the weldability predictions based on the Varestraint testing results from thin wall 310HCbN materials. A good correlation was found between hot cracking and hot ductility testing results.

Short term stress rupture testing of modified 800H, NF709, NF616 and transition joints between modified 800H and T91 was conducted. For welded modified 800H (with HD556 and Inconel 117 filler), the HAZ exhibits a lower rupture strength as compared to the base metal or filler metal. For welded NF709 (with 709 filler), the weld metal shows a slightly lower rupture strength compared to the HAZ and base metal. In general, the NF709 weldment (with NF709 filler) showed an equivalent or slightly lower rupture strength compared to the modified 800H weldments (with ether HD556 or Inconel 117 filler).

A preliminary evaluation on iron aluminide clad stainless steel tubing was carried out. Arc spray, GTAW and GMAW techniques were utilized for preparing the clad coupons. Comparison of the characteristics of the interface in terms of the different fabrication techniques was addressed. Iron aluminide weld deposited clad on stainless steel, by fusion welding, provides for an excellent bond between the iron aluminide and stainless steel and shows relatively good operational ease.

INTRODUCTION

Three major evaluations: hot cracking assessment of 310HCbN type material (HR3C), short term stress rupture testing of advanced austenitic alloy welds and a preliminary evaluation of iron aluminide weld deposited cladding on stainless steel tubing were undertaken in the last fiscal year.

The weldability studies on the high temperature alloys have enhanced the basic understanding of this group of alloys and provided information in further improvement of alloy behavior.

For coal fired power system units iron aluminide materials can play a significant role since iron aluminides possess an excellent sulfidization resistance. To combine the advantages of stainless steel and iron aluminide, a composite tubing material, in which iron aluminide is applied on the stainless steel tubing OD surface to endure the fire side environment, was evaluated using different welding process approaches. The results obtained from ORNL, B&W and The University of Tennessee on the evaluation of the iron aluminide clad stainless steel tubes show promising effects and it is expected that this study will lead to industrial structural application of the iron aluminide clad materials.

MATERIALS AND EXPERIMENTAL PROCEDURES

Tubing materials of modified 800H, 310HCbN, NF709, NF616, T91 and plate material of standard AISI 304 were utilized. Filler material of HD556 (wire), Inconel 617 (wire) Inconel 117 (SMAW electrodes), NF709 (both wire and SMAW electrodes) and NF616 (both wire and SMAW electrodes) were used to fabricated the welded coupons. Inconel 617 filler was employed to make the modified 800H/T91 transition joint coupons. The chemical composition (wt.%) of the base materials involved in the study is given in Table 1.1 while the compositions of the filler materials are shown in Table 1.2.

Table 1.1. Composition of the base materials.

	Mod. 800H (V988-1)	NF709 (E45243)	310HCbN (HR3C-A)	310HCbN (HR3C-B)	310HCbN (HR3C-C)	NF616 (2W104)	T91 (UT-B)	304 nominal
C	0.100	0.060	0.046	0.060	0.060	0.090	0.093	0.08 max
S	0.006	0.001	0.010	0.001	0.001	0.002	0.001	-
P	0.022	0.006	0.018	0.014	0.013	0.005	0.018	-
Cr	20.13	20.28	24.23	25.65	25.80	9.01	8.28	18 - 20
Ni	30.09	24.95	18.86	20.15	20.35	-	0.30	8 - 10
Mo	1.89	1.50	0.18	-	-	0.50	0.90	-
Mn	2.00	1.00	1.61	1.22	1.20	0.45	0.42	2.0 max.
Si	0.19	0.41	0.64	0.40	0.40	0.06	0.39	1.0 max
V	0.59	-	0.008	-	-	0.20	0.18	-
Al	0.01	-	-	-	-	-	0.034	-
Ti	0.28	0.05	0.009	-	-	-	0.001	-
Nb	0.22	0.26	0.32	0.47	0.45	0.050	0.066	-
N	0.007	0.167	0.202	0.246	0.250	0.048	0.047	-
Cu	0.01	-	0.08	-	-	-	0.07	-
B	0.006	0.005	-	-	-	0.004	<0.001	-
W	-	-	-	-	-	1.77	<0.01	-
Co	-	-	0.12	-	-	-	0.019	-
Sn	-	-	-	-	-	-	0.06	-
Sb	-	-	-	-	-	-	0.002	-
As	-	-	-	-	-	-	0.015	-
O	-		0.044	-	-	-	0.05	-
Fe	Bal.	Bal.	Bal.	Bal.	Bal.	Bal.	Bal.	Bal.

The assessments of the welded fabrication related HAZ hot cracking tendency were conducted on all three heats of 310HCbN tubing materials. Among them, heats HR3C-A and HR3C-B are thin walled tubing and the size was not suitable for preparation of the standard Gleeble hot ductility test samples, thus, only Varestraint hot cracking tests were performed on these two heats. Heat HR3C-C was used to conduct Varestraint hot cracking, Finger hot cracking and Gleeble hot ductility tests. Two different heat treatment conditions were evaluated for Heat HR3C-A (HR3C-A1 (as-received) & HR3C-A2 (annealed at 1200°C for 1 hour)) and both tubes were used to carry out Varestraint hot cracking tests.

Finger hot cracking tests were performed on modified 800H (V988-1), modified 800H (BWT7) and HR3C-C. Tubes V988-1 and BWT7 have the same composition. However, microstructural differences

(especially, the amount and distribution of precipitates) were evident.

Modified 800H, NF709, T91 and NF616 were used in preparing the welded coupons with HD556, Inconel 117, Inconel 617, NF709 and NF616 filler metal. Short term stress rupture testing was conducted on specimens extracted from the welded coupons of this group of materials.

AISI 304 stainless steel plate was used as the base material for the initial aluminide cladding study. The GTAW and GMAW fusion welding processes were used to deposit iron aluminide. The iron aluminide clad stainless steel coupons fabricated by hot extrusion (at B&W) and samples from the arc sprayed clad were also used for the metallographic evaluations. A composite Fe-Al wire (Al core - Fe sheath) was used for preparing the weld clad coupons.

Optical light microscopy (OLM) and scanning electron microscopy (SEM) were employed to perform the metallographic evaluations. A quantitative energy dispersive spectrum computer program (Automation Runner) was employed for chemical analysis.

Table 1.2. Composition of the filler materials.

	NF709 (wire)	NF709 (SMAW electrode)	Inconel 617 (wire)	NF616 (wire)	NF616 (SMAW electrode)	HD556 (wire)	Inconel 117 (SMAW electrode)
C	0.040	0.040	0.08	0.070	0.09	0.080	0.120
S	0.004	0.003	0.001	0.007	0.002	0.005	0.004
P	0.005	0.003	-	0.008	0.008	-	0.006
Cr	21.0	20.0	22.14	8.9	8.9	21.14	23.31
Ni	25.6	24.7	54.38	0.4	0.6	18.78	50.07
Mo	1.6	1.5	8.79	0.5	0.5	2.89	9.69
Mn	1.09	1.26	0.02	0.86	1.70	1.35	1.73
Si	0.2	0.4	0.17	0.2	0.5	0.49	0.47
V	0.036	-	-	0.098	0.024	-	
Al	-	-	1.37	-	-	0.34	
Ti	0.05	0.06	-	-	-	-	
Nb	0.24	0.23	-	0.05	0.05	0.92	0.62
N	0.228	0.160	-	0.082	0.038	-	-
Cu	-	-	-	-	-	-	0.04
W	-	-	-	1.62	1.68	2.25	-
Co	-	-	12.66	-	-	19.08	11.73
La	-	–	-	-	-	0.024	-
Ta	-		-	-	-	-	0.02
Fe	Bal.	Bal.	0.39	Bal.	Bal.	Bal.	2.19

RESULTS AND DISCUSSIONS

Hot Ductility and Hot Cracking Evaluations for 310HCbN Alloy

Hot Ductility Tests

A summary of the hot ductility test results for HR3C-C and the previously obtained hot ductility testing results on modified 800H and NF709 is presented in Table 2. HR3C-C has greater ductility recovery during on-

cooling testing than modified 800H and NF709. Thus, this 310HCbN type material has greater HAZ hot cracking resistance. The ductility as function of temperature for HR3C-C is shown in Figures 1. Again, it is indicated that the HR3C material is not sensitive to HAZ liquation cracking.

Table 2. Summary of hot ductility test results.

Material	DRR-1 (%)	DRR-2 (%)	NDR (C°)	RDR (%)	ZDT (°C)
Mod. 800 (V988-1)	50	13	75	18	1300
NF709 (E45243)	17	79	40	35	1308
310HCbN (HR3C-C)	130	93	20	100	1320

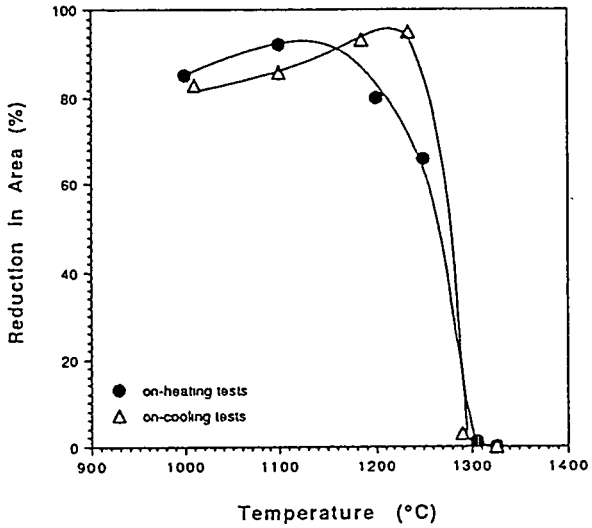

Figure 1. Ductility behavior of 310HCbN strength behavior of 310HCbN (HR3C-C).

Varestraint Hot Cracking Tests

A summary of the Varestraint hot cracking test results at 4% augmented strain for the 310HCbN alloys and the results from modified 800H and NF709 is presented in Table 3 in terms of total crack length, maximum crack length and cracked HAZ length (base metal HAZ) for all three zones. Higher hot cracking resistance in all three zones for 310HCbN is evident contrasted to modified 800H.

Table 3. Summary of Varestraint hot cracking tests at 4% augmented strain.

Material	Base Metal HAZ			Fusion Zone		Weld Metal HAZ	
	MCL	TCL	CHL	MCL	TCL	MCL	TCL
Mod. 800 (V988-1)	0.44	1.75	2.60	1.97	11.28	0.14	0.26
NF709 (E45243)	0.14	0.47	1.36	0.82	5.88	0.17	0.46
310HCbN (HR3C-A1)	0.09	0.22	1.06	1.33	6.53	0.24	0.90
310HCbN (HR3C-A2)	0.23	0.53	1.58	1.34	8.38	0.09	0.13
310HCbN (HR3C-B)	0.12	0.29	1.25	0.72	6.74	0.16	0.76
310HCbN (HR3C-C)	0.18	0.43	0.97	0.79	7.87	0.15	0.44

Finger Hot Cracking Tests

Finger hot cracking test results in terms of maximum crack length (MCL), total crack length (TCL) and average ratio of crack length to weld width were determined and are documented in Table 4. It is indicated that HR3C-C shows a greater hot cracking resistance than modified 800H. For the modified 800H ageing at 1200°C for 1 hour increases the hot cracking tendency compared to the as-received condition. Modified 800H (V988-1) shows a slightly lower hot cracking tendency than modified 800H (BWT7) (It should be pointed out that the Finger hot cracking test only indirectly reflects base metal HAZ hot cracking tendency.). However, the ranking from the Finger hot cracking tests agrees with the Varestraint hot cracking tests. A bar graph showing Finger hot cracking behavior is presented in Figure 2.

Table 4. Summary of Finger hot cracking testing results.

	Mod. 800H (V988-1) as-received	Mod. 800H (V988-1) aged 1 hr at 1200°C	Mod. 800H (BWT7) as-received	Mod. 800H (BWT7) aged 1 hr at 1200°C	310HCbN (HR3C-C) as-received
MCL[1]	0.52	1.13	0.49	1.09	0.43
TCL[2]	0.81	2.53	1.39	3.78	0.63
Ratio[3]	0.95	2.98	1.61	4.73	0.74

1: maximum crack length. 2: total crack length. 3: average ratio of crack length to weld width.

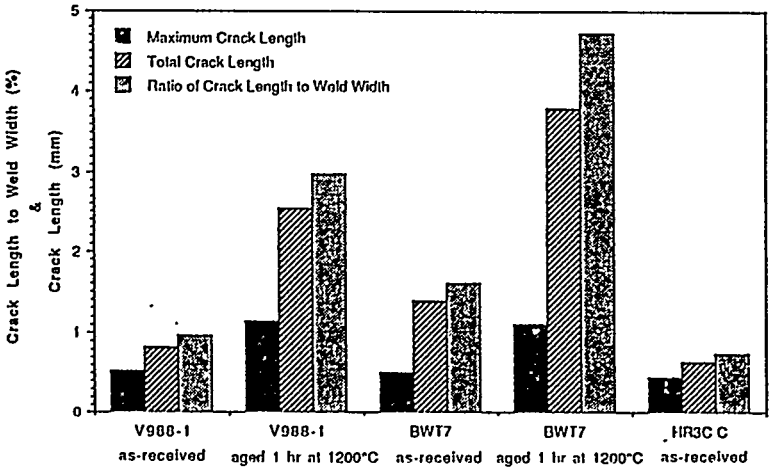

Figure 2. Figure hot cracking test results.

Stress Rupture Tests

HAZ softening was evident from a previous hardness evaluation of the weldments in advanced austenitic alloys, especially, modified 800H. In order to reveal whether HAZ softening degrades the HAZ mechanical properties, stress rupture tests were carried out on modified 800H, NF709 and transition joints between T91 and modified 800H. Figure 3 shows stress as a function of rupture time for modified 800H and NF709 while Figure 4 shows the stress rupture behavior of NF616 and the transition joint between modified 800H and T91. A

summary of stress rupture evaluation results including applied stress, rupture time, failure location, and the rupture ductility is given in Table 5.

The stress rupture results agree with the prediction from the microhardness measurements, in which mechanical property degradation was evident in the HAZ of modified 800H weldments. According to the stress rupture testing results, the HAZ of modified 800H shows lower rupture strength as compared to the base metal.

Table 5. Summary of Stress Rupture Testing Results.

Sample & Filler Material	Rupture Location	Stress (ksi)	Rupture Time (hr)	Ductility (%)
Mod.800H/HD556	Fine Grained HAZ	40	12	64
Mod.800H/HD556	Fine Grained HAZ	35	42	73
Mod.800H/HD556	Coarse Grained HAZ	30	152	75
Mod.800H/HD556	Partially Melted HAZ Adjacent to Fusion Boundary	25	624	68
Mod.800H/Inconel 117	HAZ	40	10	72
Mod.800H/Inconel 117	HAZ (the end away from Fusion Line)	35	8.3	68
Mod.800H/Inconel 117	Fusion Zone (Significant necking occurred in HAZ)	30	6.7	44
NF709/NF709	Fusion Zone	40	10	69
NF709/NF709	Base Metal (Crack at Fusion Zone almost through the cross section)	35	125.9	23
NF709/NF709	HAZ	30	12	46
BM of Mod.800H	Base Metal	45	51	57
BM of Mod.800H	Base Metal	40	101	66
Mod.800H/T91/617/filler PWHT: 1400°F; 30 mins.	the HAZ at T91 side	14	0.9	83
Mod.800H/T91/617/filler PWHT: 1400°F; 30 mins.	the HAZ at T91 side	12.8	0.5	92
Mod.800H/T91/617/filler PWHT: 1400°F; 30 mins	the HAZ at T91 side	11.43	5	92
Mod.800H/T91/617filler as-welded	the HAZ at T91 side	14	1.6	66
Mod.800H/T91/617filler as-welded	the HAZ at T91 side	12.8	2.4	84
Mod.800H/T91/617/filler as-welded	the HAZ at T91 side	11.43	3.1	89
Mod.800H/T91/617filler as-welded	the HAZ at T91 side	10	15.8	88
NF616/NF616/NF616filler PWHT: 1400°F; 30 mins.	HAZ	12.8	32	65
NF616/NF616/NF616filler PWHT: 1300°F; 30 mins.	HAZ	11.43	56	57
NF616/NF616/NF616filler PWHT: 1400°F; 30 mins.	HAZ	11.43	87	65
NF616/NF616/NF616filler PWHT: 1400°F; 30 mins.	HAZ	10	227.3	38

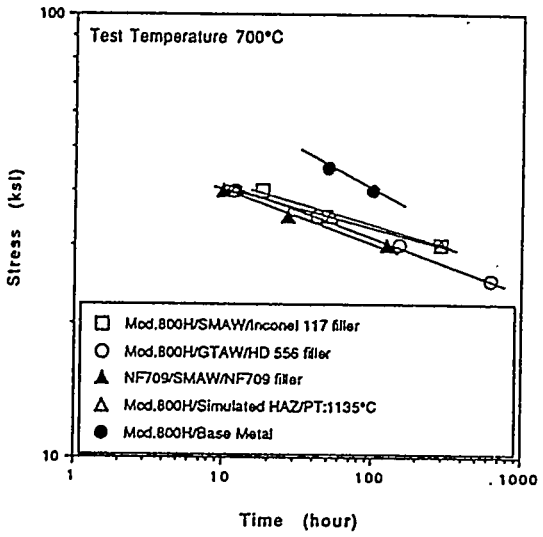

Figure 3. Stress rupture behavior of modified 800H and NF709.

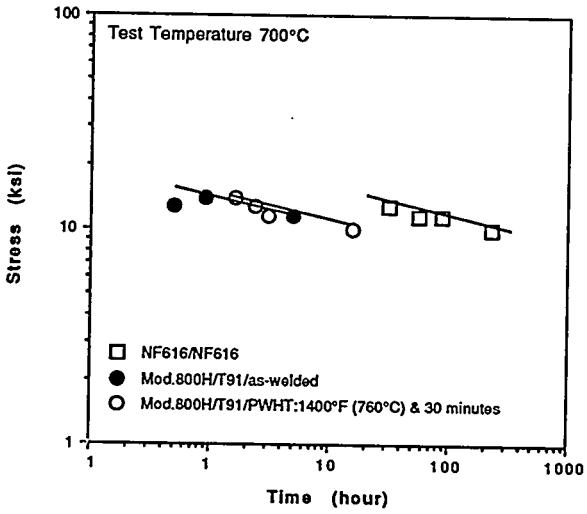

Figure 4. Stress rupture behavior of transition and joint between modified 800H and T91, and NF616.

The NF709 weldments showed a rupture strength similar to modified 800H although no significant HAZ softening was found in NF709 (a cold worked schedule is not incorporated for NF709 base metal performance).

As was expected, all transition joint (modified 800H to T91) specimens ruptured in the HAZ of the T91 for both as-welded and the welded + PWHT (1400°F for 30 minutes) conditions. PWHT slightly reduced the rupture strength of the HAZ on the T91 side of the transition joint. Tungsten containing (1.8 wt.%) 9Cr type steel, NF616, showed significantly higher weldment stress rupture strength compared to T91.

Metallographic Evaluation of Iron Aluminide Clad Stainless Steels

Based on etching response, the UTFA-1 etching practice [6] was selected for metallographic samples. Using this etching practice, grain boundaries can be definitively revealed and segregation bands are darkened in the iron aluminide cladding. The different grain orientations and constituents can be distinguished by choosing the proper etching conditions.

A typical microstructural morphology of the bond region of the iron aluminide clad stainless steel samples fabricated by arc spray is shown in Figure 5. Small scale porosity and lack of fusion were found in this type of cladding. With back scattered electron imaging, the EDS analyses indicate that the dark areas (lettered A and B) are rich in Al and bright gray areas (lettered C and D) are predominantly pure Fe. The areas E and F contain both Fe and Al. Therefore, in the as-sprayed condition, the clad material is mixture of Fe_3Al, FeAl, $FeAl_3$, Fe and Al. It is evident that further experimental work should be carried out on the arc-spray technique with the composite wire to produce the desired iron aluminide clad (single iron aluminide phase) on stainless steel.

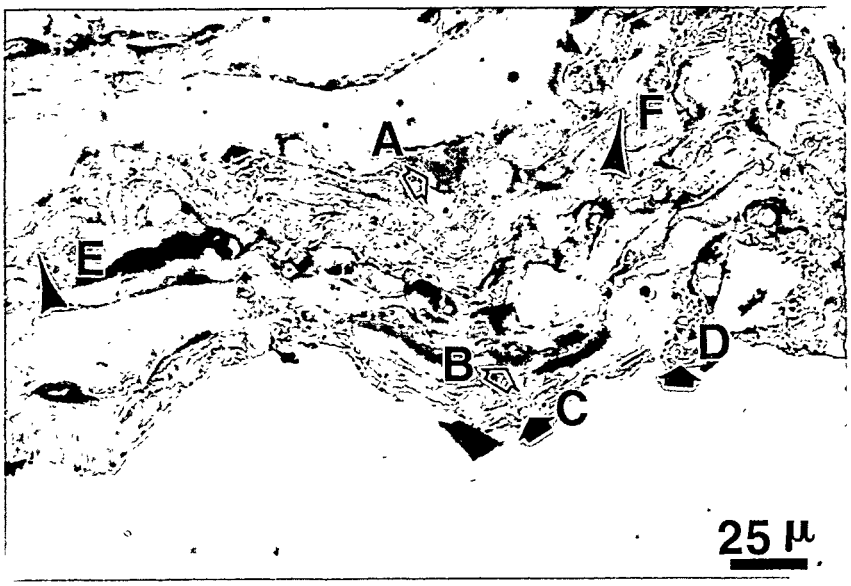

Figure 5. Typical microstructural morphology of bond area of the iron aluminide clad stainless steel with arc spray technique.

Figure 6 (a) shows the typical microstructural morphology of the interface region between the iron aluminide clad and 304 matrix of the B&W fabricated tuber at (hot extrusion). Excellent bonding is evident. Figure 6 (b) shows a GTAW autogenous bead on the OD surface of the hot extruded iron aluminide clad tube coupon. It is clear that interface cracks are observed under the weld. This indicates that the interface may be the critical location for this type of clad tube and interface cracking may occur under welding residual stresses during welding of the tubing.

Figure 7 shows the typical microstructure in a cross section through the iron aluminide GTAW clad 304 stainless steel. Excellent bonding between the clad and matrix was obtained in addition to a single iron aluminide phase. Since cladding by fusion welding can be performed during the last stage of the structural fabrication, interface cracking tendency induced by tube butt welding may be minimized.

Figure 8 shows the SEM morphology in the bond area in the GMAW iron aluminide clad. EDS quantitative chemical analysis was conducted across the bond area. In order to define the locations where EDS was performed, "crosses" are shown on the micrograph. The EDS results along Lines ab, cd and ef in Figure 9 are presented in Figures 9, 10 and 11, respectively. As indicated in Figures 9, 10 and 11, a single phase Fe_3Al ($D0_3$) was obtained in the clad. It is revealed by EDS that base metal has been diluted into the clad. Since a small amount of Cr (about 5 at.%) has a beneficial effect on ductility without reducing corrosion resistance [8], the enhanced Cr content in the clad may be beneficial to clad deposition behavior. An in situ melted zone (showing solidification substructure) was observed between the clad and matrix. The existence of an in situ melted zone provides for a relatively uniform chemical and mechanical property gradations and is expected to benefit bonding behavior.

(a)

(b)

Figure 6. The bond area microstructural morphology; (a) as-extruded condition; (b) with GTA weld on top of the iron aluminide clad.

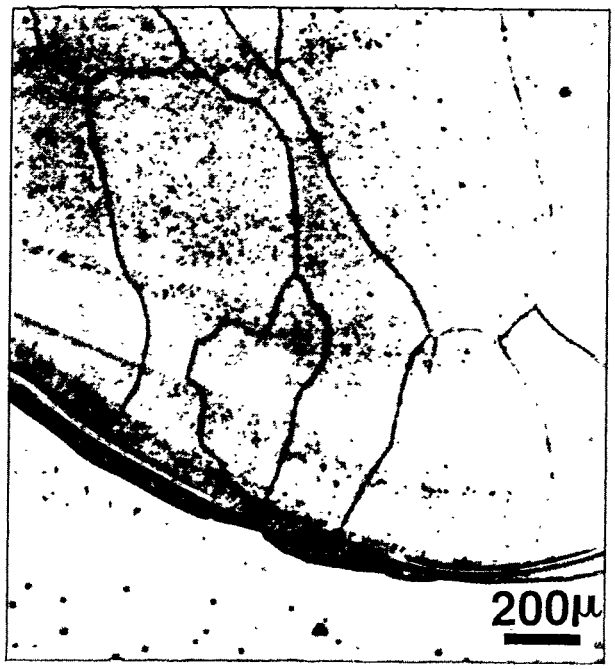

Figure 7. Typical microstructure of the cross section of GTAW welded iron aluminide clad stainless steel sample.

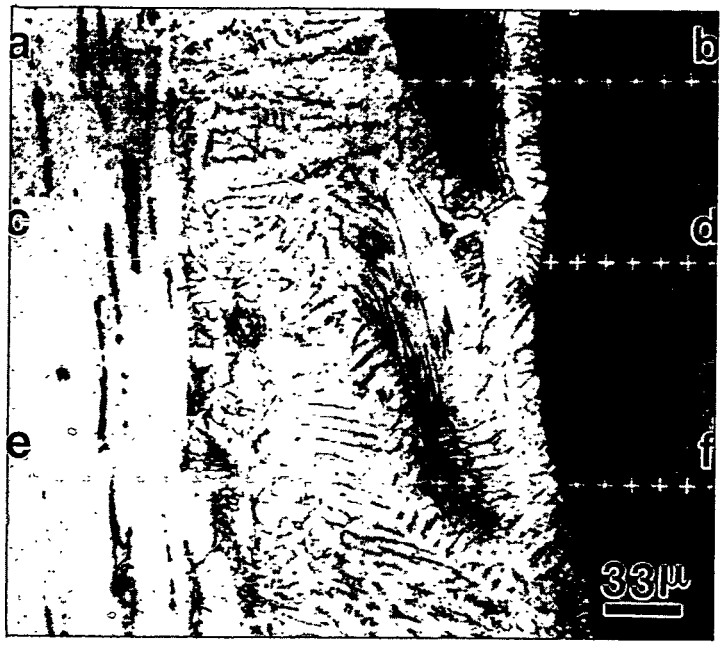

Figure 8. SEM morphology of GMAW welded iron aluminide clad stainless steel sample.

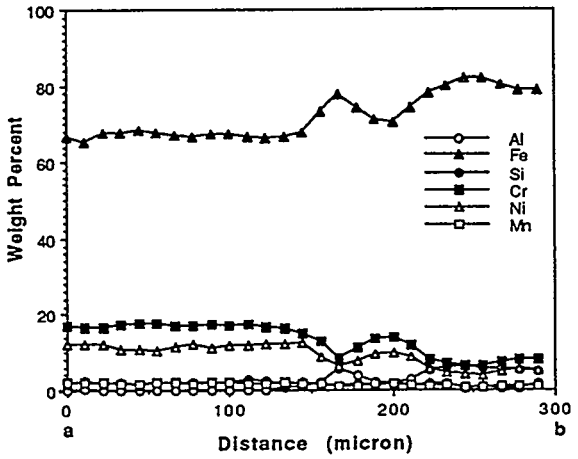

Figure 9. EDS results for line ab.

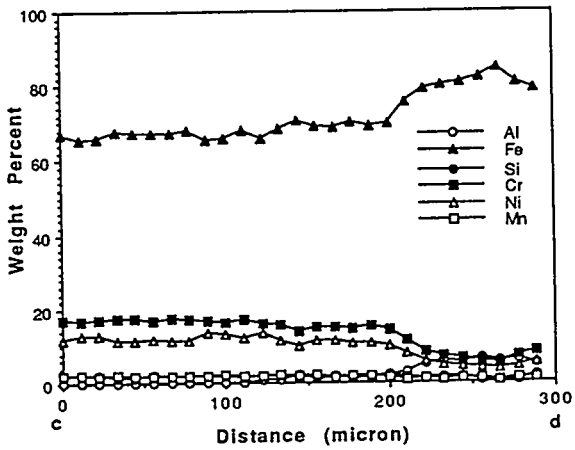

Figure 10. EDS result for line cd.

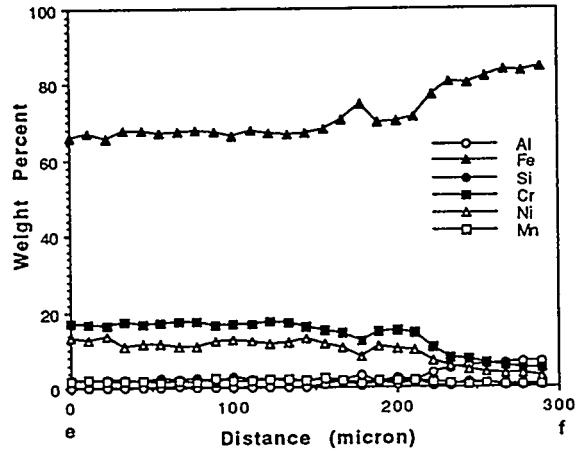

Figure 11. EDS results for line cd.

Silicon is also diluted into the clad although the amount of Si present in the clad is low. Silicon segregation in the iron aluminide clad may tend to form other secondary phases and/or cause an eutectic reaction. Weld solidification cracks were found in the GMAW clad iron aluminide samples. To minimize the crack sensitivity, adjustment of the alloying elements of the filler may be needed.

SUMMARY

1. Alloy 310HCbN showed a better hot cracking resistance compared to modified 800H tubing material based upon the results obtained from the Varestraint hot cracking test, Finger hot cracking test and Gleeble hot ductility test.

2. The results from short term stress rupture testing of the weldments of advanced austenitic alloys indicate that HAZ mechanical property degradation occurs in modified 800H. No HAZ mechanical property degradation

was observed in NF709 weldment and, the rupture strength of the NF709 weldment is similar to that of modified 800H.

3. The GTAW and GMAW processes were employed to deposit iron aluminide as a clad on austenitic stainless steel. Excellent bonding was obtained using GTAW and GMAW. These approaches provide a promising opportunity for industrial applications of iron aluminide clad tubing.

4. Weld solidification cracks were found in the iron aluminide clad. To minimize the solidification cracking tendency, major compositional adjustments in the alloy system and/or addition of minor alloying elements to the filler may be needed.

5. Silicon rich precipitates and other secondary phases which may form in the aluminide clad, at elevated temperature, should be investigated in order to reveal whether these secondary phases are detrimental to cladding performance.

ACKNOWLEDGMENTS

This study was financially supported by the U.S. Department of Energy, through Fossil Energy Materials Program operated at Oak Ridge National Laboratory managed by Martin Marietta Energy Systems Inc..

REFERENCES

1. Ogawa, K., Sawaragi, Y., Yamamoto, S., Natori, A., and Tukamoto, M., "Properties of HR3C Tube Welded Joints with Similar Welding Materials," EPRI Conference, Washington, March 1 - 3, 1993.

2. Sumitomo Metal Industries, LTD., "Characteristics of New Steel Tube (HR3C) with High Elevated Temperature Strength and High Corrosion Resistance for Boiler," Technical Report, Sumitomo Metal Industries, LTD, December 1987.

3. McKamey, C.G., DeVan, J.H., Tortorelli, P.F. and Sikka, V.K., "A review of recent developments in Fe_3Al-based alloys," J. Mater. Res, Vol. 6, No. 8, Aug. 1991.

4. Vyas, S., Viswanathan, S., and Sikka, V.K., "Effect of Aluminum Content on Environmental Embrittlement in Binary Iron-Aluminum Alloys," Scripta Metallurgica et Materialia, Vol. 27, pp. 185-190, 1992.

5. The University of Tennessee, a proposal for requesting the continuation of DOE Project on Weldability and Joining Techniques for Advanced Fossil Energy System Alloys, The University of Tennessee, Knoxville, August 1991.

6. Lundin, C.D., and Qiao, C.Y.P. "Preliminary Investigations of the Fe-Al Cladding on HR3C Alloy," technical report, The University of Tennessee, September 1993.

7. Mohn, W.R. and Topolski, M.J., "Evaluation of the Fabricability of Advanced Iron Aluminide-Clad Austenitic Stainless Steel Tubing," DOE Technical report, ORNL/Sub/88-SB775/03, July 1993.

8. Buchanan, R.A., and Kim, J., "UTN-3-Aqueous Corrosion of Iron Aluminides in Chloride and Sulfur-Compound Solutions," pp. 241-251, DOE Technical Report, ORNL/FMP-92-2, September 30, 1992.

Cr_2Nb-BASED ALLOY DEVELOPMENT

C. T. Liu, J. A. Horton, and C. A. Carmichael

Oak Ridge National Laboratory
Metals and Ceramics Division
P. O. Box 2008
Oak Ridge, TN 37831-6115

ABSTRACT

This paper summarizes recent progress in developing Cr_2Nb/Cr(Nb) alloys for structural use in advanced fossil energy conversion systems. Alloy additions were added to control the microstructure and mechanical properties. Two beneficial elements have been identified among all alloying additions added to the alloys. One element is effective in refining the coarse eutectic structure and thus substantially improves the compressive strength and ductility of the alloys. The other element enhances oxidation resistance without sacrificing the ductility. The tensile properties are sensitive to cast defects, which can not be effectively reduced by HIPping at 1450-1580°C and/or directionally solidifying via a floating zone remelting method.

INTRODUCTION

The objective of this task is to develop new-generation structural materials based on intermetallic alloys for use as critical hot components in advanced fossil energy conversion systems. The intermetallic phase, Cr_2Nb, with a C-15 complex cubic structure,[1] has been selected for this development effort because of its high-melting point (1770°C),[2-3] relatively low density (7.7 g/cm^2),[4] and potential resistance to oxidation and corrosion.[2] This intermetallic phase, like many other Laves phases, has a wide range of compositional homogeneity,[3] suggesting the possibility of improving its mechanical and metallurgical properties by alloy additions.

The major concern with Cr_2Nb and other A_2B Laves phases is their poor toughness and fracture resistance at ambient temperatures.[2,5,6] The single-phase Cr_2Nb is very hard (~800 DPH) and brittle at room temperature. Because of the brittleness, our development effort has been concentrated on two-phase structures containing the intermetallic phase

Cr_2Nb (hard phase) and the Cr-rich solid-solution phase (ductile phase). Previous studies indicated that the two-phase alloys exhibited plastic deformation under compression tests at room temperature, with strength much superior to nickel-base superalloys at and above 1000°C.[5,7,8] Bhandarker[9,10] has demonstrated that a dispersion of Fe_2Ta Laves-phase particles dispersed within grains of a ferritic steel produced good elevated-temperature strength without causing low-temperature embrittlement. Recently, considerable effort has been devoted to the development of new superalloys containing Laves phases for high-temperature structural use.[5-8, 10-16]

Our results obtained so far indicate that the two-phase Cr_2Nb/Cr(Nb) alloys have excellent strength for structural use at ultrahigh temperatures (e.g., 1000-1200°C).[5-8] Potential applications include hot components in advanced energy conversion systems, advanced heat engines, and high-temperature cutting and grinding tools. Current studies are focused on enhancement of fracture resistance and oxidation resistance. This report summarizes our recent progress on controlling microstructure and improving mechanical properties of Cr_2Nb/Cr(Nb) alloys through alloying additions and material processing. A detailed study of the corrosion behavior of these alloys has been reported separately by Tortorelli et al.[17-19]

ALLOY PREPARATION AND PROCESSING

Cr_2Nb/Cr(Nb) alloys weighing 300 g were prepared by arc melting and drop casting in copper molds (1" diam. x 3" long). In order to minimize the interstitial content (e.g., oxygen) in these alloys, high-purity niobium and chromium metal chips were used as charge materials, and the alloys were melted in a high vacuum (10^{-5} Pa) furnace. Cast molds were pre-heated to 100-300°C in order to control solidification and to reduce thermal shock during drop casting.

Oxide slags in cracked pieces were observed on the top of alloy buttons and ingots. Sometimes, these oxides were found to be trapped inside alloy ingots. Careful x-ray fluorescence studies indicate that these oxide slags contain mainly zirconium and aluminum. Removal of zirconium and aluminum from the alloys dramatically reduces the slag amount. The drop-cast behavior of the alloys is also sensitive to alloy additions. The drop castability can be substantially improved by certain alloying elements; however, these elements can only be identified by melting and casting practice.

The cast alloy ingots generally contain cast cavities, which vary in size from a few to several hundred μm.. The existing phase diagram of the Cr-Nb system indicates an

eutectic temperature of 1620°C for the Cr_2Nb and Cr-rich phases.[3] Accordingly, the Cr_2Nb/Cr(Nb) alloys were HIPped at 1450 and 1580°C at a maximum stress of 207 MPa (30 ksi) in order to reduce or eliminate the cavities. Metallographic examination of the ingot interior indicates only marginal reduction in cast porosities by these HIPpings. This observation indicates extremely high strength at these temperatures and/or a higher melting point of these alloys. Thus, we re-examined the incipient melting point of the chromium niobium (CN) alloys. In this study, alloy specimens were rapidly heated from 1200°C to a preset temperature and kept at that temperature for 6 min., followed by turning off the power. Our studies indicate that the melting point of CN alloys is ~1670 ± 20°C, which is about 50°C above the reported eutectic temperature for the Cr-Nb system. Based on the determined melting point, we plan to HIP the alloys again at a temperature close to 1650°C.

Two alloys, CN-67 and -65 (see Table 1), were processed by floating-zone remelting at a velocity of 1.9 - 2.4 cm/hr in high-purity inert gas at the University of Tennessee, using drop-cast ingots as a starting material. Figure 1 shows the rough ingot surfaces, which resulted from evaporation of chromium and formation of surface oxides during crystal growth. Metallographic examination of sectioned ingots shows large holes formed near the ingot surfaces (probably due to chromium evaporation) and cast micro-cavities away from the surface region. This observation indicates that cast cavities in these alloys cannot be completely eliminated by directional solidification through a floating-zone remelting method.

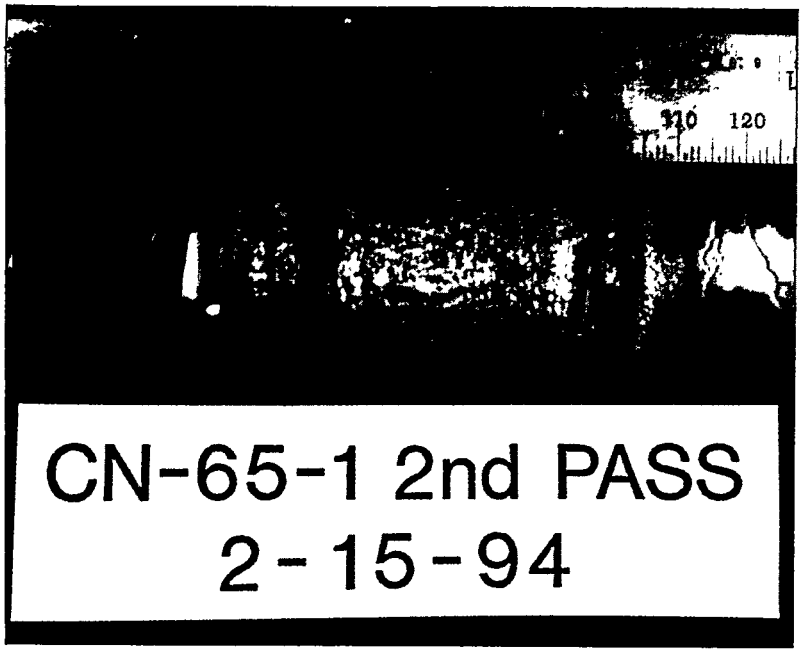

Fig. 1 CN-65 alloy ingot prepared by levitation-zone remelting.

EFFECT OF ALLOYING ADDITIONS ON MICROSTRUCTURE AND PHASE COMPOSITION

During this year, a total of 25 new alloys were prepared. A partial list of the alloy compositions is shown in Table 1. The alloys with 5.6 to 12 at. % Nb basically contain primary Cr-rich solid solution surrounded by the eutectic structure (Fig. 2a), a mixture of Cr_2Nb-type and the Cr-rich phases. The supersaturated Cr-rich solid solution (bright-contrast phase) precipitates out Cr_2Nb-type particles when annealed above 1000°C. The brittle, coarse Cr_2Nb particles in the eutectic structure are, in most cases, interconnected into a skeleton (dark-contrast phase in Fig. 2a) which is believed to be one of the major causes of poor fracture resistance of the CN alloys.

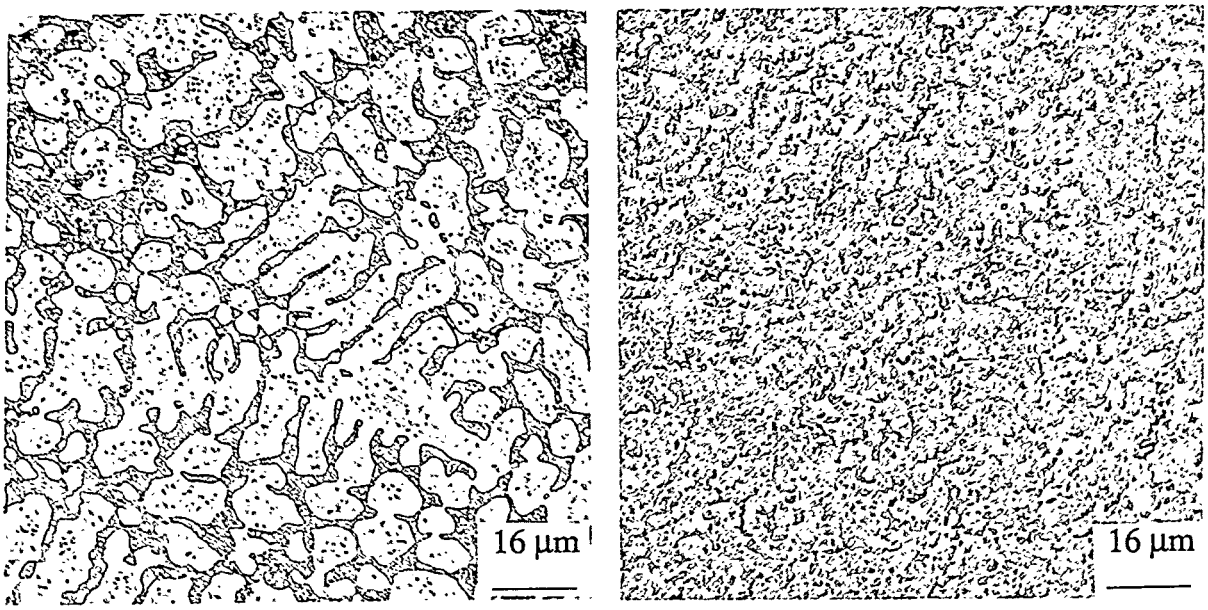

Fig. 2 Optical micrographs of (a) CN-61 and (b) CN-60 annealed for 3 d at 1100°C.

Alloying additions were added to refine the coarse Cr_2Nb eutectic structure in the CN alloys. Among all elements added to the alloys, the element referred to as XM is most effective in refining the interconnected eutectic structure (Fig. 2b). As shown in Fig. 3, the eutectic skeleton is broken into blocky Cr_2Nb-type particles in the alloy containing 6% XM. Another element, referred to as XO, is found to be most effective to date in improving oxidation resistance of the CN alloys. Because of their beneficial effects, a series of alloys containing these two elements were prepared as shown in Table 1. Our studies of the mechanical properties and oxidation resistance[19] suggest the optimum amount of XM and XO in the same alloy to be 6 and 4%, respectively.

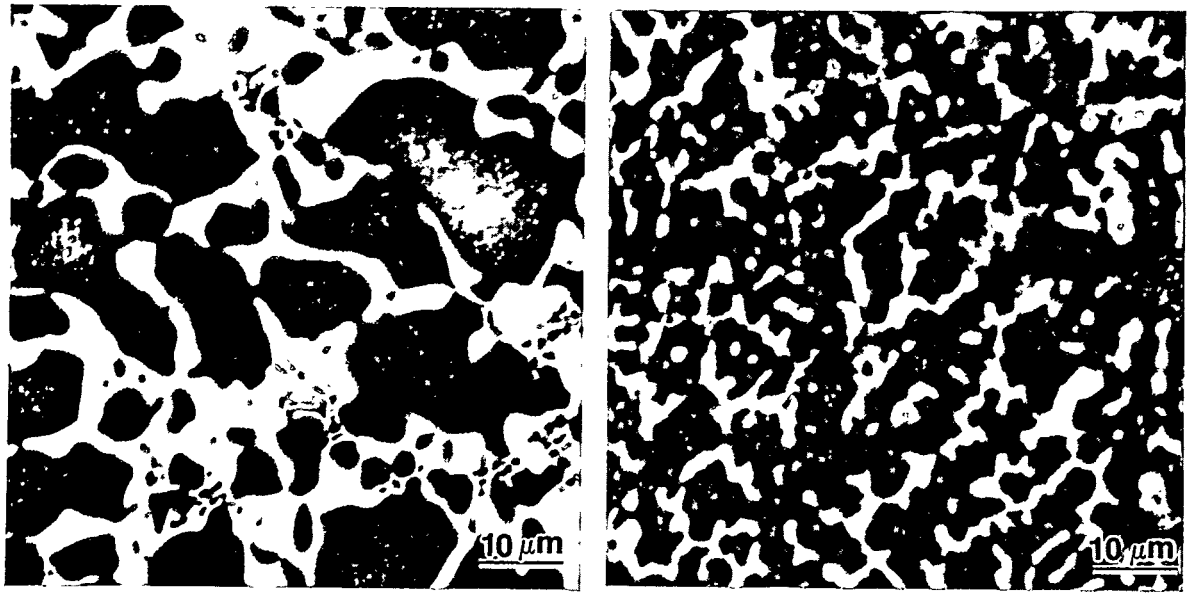

(a) (b)

Fig. 3 Backscattered electron images of (a) CN-61 and (b) CN-60 annealed for 3 d at 1100°C.

Table 1. Nominal Alloy Compositions of Selected CN Alloys

Alloy Number	Composition (at. %)
CN-60	Cr-12.0Nb-4.0Re-2.0Al-6.0XM
CN-80	Cr-12.0Nb-1.5Al-6.0XM
CN-72	Cr-12.0Nb-1.5Al-0.1Zr-6.0XM
CN-61	Cr-12.0Nb-4.0Re-2.0Al-4.0XO
CN-81	Cr-10.0Nb-1.5Al-6.0XM-4.0XO
CN-67	Cr-8.0Nb-1.5Al-0.1Zr-6.0XM
CN-64	Cr-5.6Nb-1.5Al-0.1Zr-4.0XM
CN-65	Cr-5.6Nb-1.5Al-0.1Zr-6.0XM
CN-69	Cr-5.6Nb-1.5Al-6.0XM
CN-70	Cr-5.6Nb-1.5Al-0.1B-6.0XM
CN-68	Cr-5.6Nb-1.5Al-0.1Zr-4.0Re-6.0XM
CN-66	Cr-5.6Nb-1.5Al-0.1Zr-10.0XM
CN-71	Cr-5.6Nb-1.5Al-0.1Zr-15.0XM
CN-74	Cr-5.6Nb-1.5Al-0.1Zr-6.0XM-4.0XO
CN-75	Cr-5.6Nb-1.5Al-0.1Zr-6.0XM-6.0XO
CN-76	Cr-5.6Nb-1.5Al-0.1Zr-6.0XM-8.0XO

Figure 4 shows the effect of heat treatment on the microstructures of the CN-65 alloy containing 5.6% Nb. Fine precipitates distribute uniformly across grains and some

coarse Cr_2Nb particles are observed at grain boundaries in the specimen (Fig. 4a) annealed at 1100°C for 3 days. HIPping at 1450°C apparently dissolved a major part of the fine precipitates within grains but did not remove the coarse Cr_2Nb particles at grain boundaries (Fig. 4b). A few cavities are visible in the HIPped specimen. Figure 5 shows the microstructure of the alloy containing 6% XM and 6% XO, where the eutectic structure can be easily identified. Comparison of Fig. 5 with Figs. 3b and 4a suggests that XO additions stabilize the classic eutectic structure.

The composition of phases in CN alloys was determined by electron microprobe analyses. Table 2 summarizes the composition of the phases determined by wavelength-dispersive spectrometry (WDS). The Cr-rich solid solution, the matrix phase, contains a low level of niobium, ~1%. The Cr_2Nb-type phase, on the other hand, contains more than 20% Nb, and the exact amount of niobium in the Cr_2Nb-type phase depends on the partitioning of alloying additions in the CN alloys. The element XM partitions more or less equally in the Cr_2Nb and the Cr-rich phases. The analysis of the composition of Cr_2Nb-type phase in CN-65 indicates that XM essentially occupies the niobium sites. The element XO in CN-75 partitions strongly in the Cr_2Nb-type phase, as indicated in Table 2. The partitioning ratio of XO in the Cr_2Nb-type and Cr-rich phases is 5.6 to 1. Unlike XM,

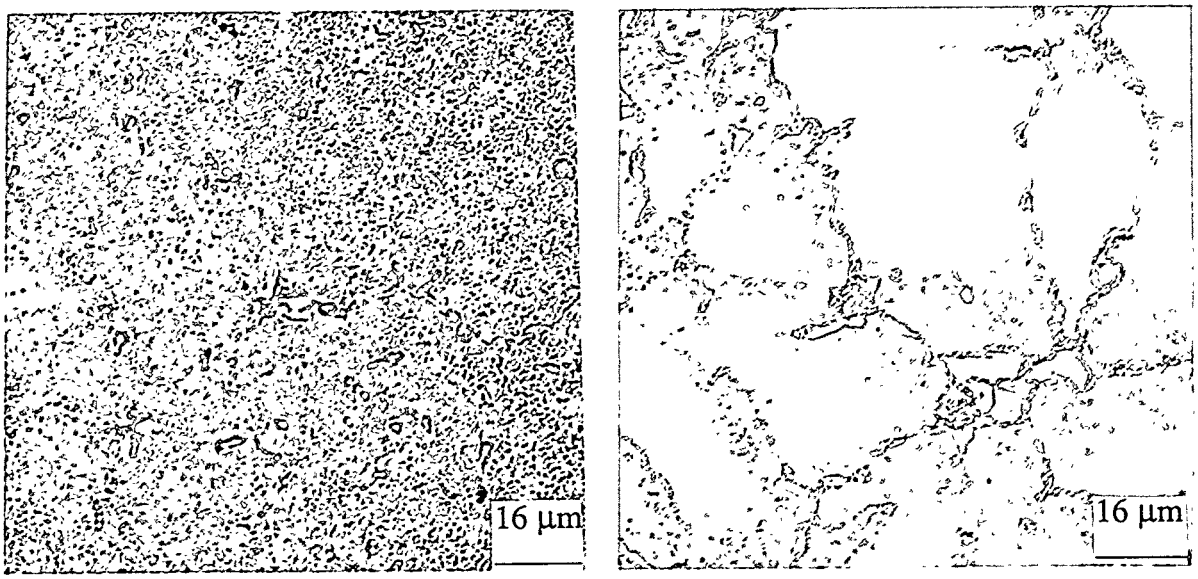

Fig. 4 Optical micrographs of CN-65 (a) annealed for 3 d at 1100°C, and (b) HIPped for 2 h at 1450°C.

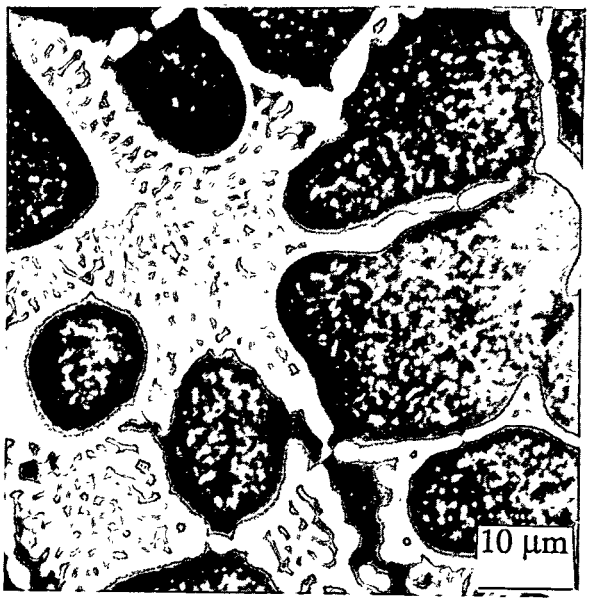

Fig. 5 Backscattered electron image of CN-75 annealed for 3 d at 1200°C.

Table 2. WDS Compositional Analysis of CN Alloys*

Alloy Number	Cr_2Nb-type Phase (at.%)	Cr-rich Matrix Without Fine Cr_2Nb Precipitates (at.%)	Cr-rich Matrix With Fine Cr_2Nb Precipitates (at.%)
CN-65	Cr = 67.0 Nb = 25.8 XM = 5.4 Al = 1.8 Zr = 0.0	Cr = 90.9 Nb = 1.2 XM = 6.7 Al = 1.2 Zr = 0.0	Cr = 88.2 Nb = 4.4 XM = 6.2 Al = 1.2 Zr = 0.0
CN-60	Cr = 63.4 Nb = 25.4 XM = 5.0 Re = 4.2 Al = 2.0		Cr = 79.0 Nb = 7.6 XM = 6.8 Re = 5.1 Al = 1.5
CN-75	Cr = 55.0 Nb = 22.3 XM = 7.9 XO = 14.0 Al = 0.8 Zr = 0.0	Cr = 90.2 Nb = 0.6 XM = 5.2 XO = 2.5 Al = 1.5 Zr = 0.0	Cr = 86.8 Nb = 3.0 XM = 5.5 XO = 3.4 Al = 1.3 Zr = 0.0

*Specimens annealed for 3 d at 1100°C or 1200°C.

XO mainly occupies the Cr sites instead of the niobium sites. The elements rhenium and aluminum partition approximately equally in the two phases. Zirconium was not detected in the CN alloys, and was probably lost due to its formation of ZrO_2 slags during melting.

The alloys CN-60 and CN-61 were examined by transmission electron microscopy (TEM). Both alloy specimens were annealed for 3 d at 1100°C, and then cut into 3 mm disks and ground to a thickness of approximately 50 μm, followed by ion milling at 6 kV. The specimens were examined in a Philips CM30 at 300 kV. Energy dispersive spectroscopy (EDS) was performed with an EDAX 9100 spectrometer. The EDS analyses were made on precipitates that intersected the ion milling perforations, thereby minimizing the contributions from surrounding matrix material.

Both alloys showed a mixture of the Cr-rich solid solution and Cr_2Nb-type phases. The small precipitates in the Cr-rich matrix ranged up to 0.4 μm in diameter. Figure 6a shows the eutectic structure (dark areas) in CN-61 (containing 4% XO) with only a few secondary precipitates visible. Figure 6b shows a region in CN-60 (containing 6% XM) with an extensive secondary precipitation. EDS analyses of the matrix versus the precipitates were made along the edge of the specimen as shown in Fig. 6b. Figure 6c shows dislocations in the Cr-rich matrix in CN-60. While many of the dislocations appeared to have interacted with small precipitates by bowing between them, many other dislocations have formed low-angle network structures.

EDS results were averaged and are shown in Table 3. Basically, the data in Table 3 agree well with those in Table 2 determined by electron microscopic analysis. In CN-60, the XM and rhenium additions did not preferentially partition to Cr_2Nb particles. Only about 1% of niobium remained in solution, with the rest precipitating out. In CN-61, the XO additions did preferentially precipitate out with the niobium in Cr_2Nb-type particles, while again the rhenium levels were similar in both matrix and in the Cr_2Nb-type phase. Apparently, no zirconium was retained by the alloy.

MECHANICAL PROPERTIES

Compressive Properties

Because the cast CN alloys, even in the HIPped conditions, contain defects such as cavities, the compressive properties are much less sensitive to these defects.

Therefore, the compressive properties of the CN alloys were determined at temperatures to 1200°C. Alloy specimens were annealed for 3 d at 1100°C prior to testing at room temperature in air and at elevated temperatures in vacuum. Tables 4 and 5 summarizes the results at different temperatures. For the alloys containing 12 at.% Nb, the yield strength at room temperature increases significantly by alloying with XM, rhenium, and XO. However, only XM improves the room-temperature ductility. XM is also very

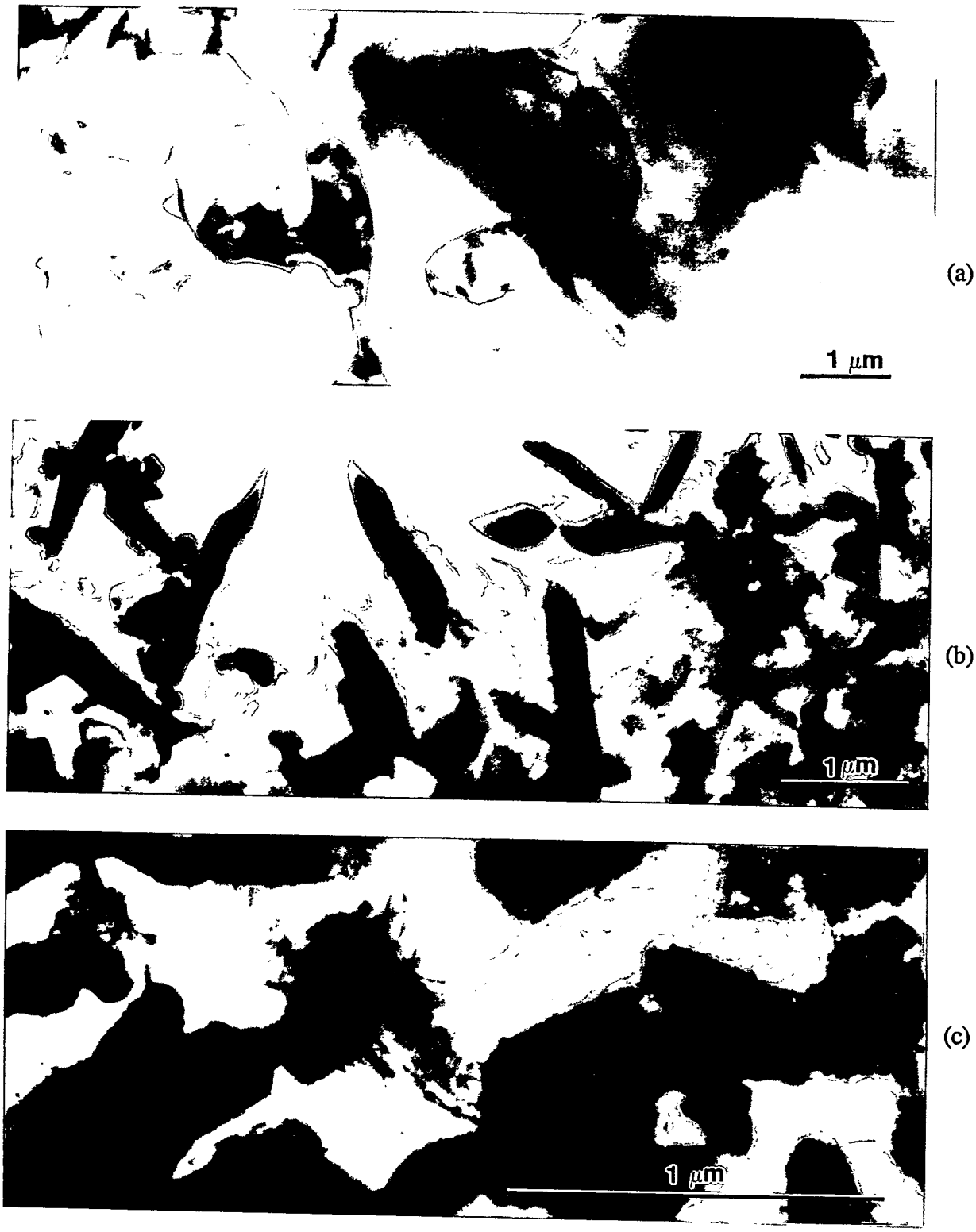

Fig. 6 TEM micrographs of (a) the eutectic Cr_2Nb structure in CN-61, (b) blocky particles in CN-60, and (c) dislocations in CN-60. All specimens were annealed for 3 d at 1100°C.

Table 3. EDS/TEM Compositional Analysis of CN-60 and CN-61

Alloy No.	Concentrations (at.%) Cr	Nb	Re	Al	XM	XO
CN-60						
nominal	76	12	4	2	6	
matrix	86	1	5	0	7	
secondary precipitation	52	39	5	0	3	
large precipitates	63	28	4	0	5	
CN-61						
nominal	78	12	4	2		4
matrix	91	1	3	1		5
large precipitates	53	28	4	1		13
secondary precipitates	57	29	5	0		15

Table 4. Compressive Properties of CN Alloys Tested at Room Temperature in Air

Alloy No.	Concentration of Key Elements (at.%)	Strength, MPa (ksi) Yield	Ultimate	Ductility (%)
CN-4	12Nb	960 (139)	1760 (255)	5.4
CN-44	12Nb-4Re	1230 (179)	2050 (298)	4.3
CN-60	12Nb-4Re-6XM	1793 (260)	2546 (369)	8.5
CN-61	12Nb-4Re-4XO	1395 (202)	1946 (282)	5.2
CN-7	6Nb	702 (102)	1261 (183)	9.5
CN-65	5.6Nb-6XM	1116 (161)	2228 (323)	16.0
CN-65*	5.6Nb-6XM	1097 (159)	2116 (307)	18.5
CN-68	5.6Nb-4Re-6XM	1111 (161)	2023 (293)	17.7
CN-70*	5.6Nb-0.1B-6XM	1047 (152)	2059 (297)	16.3
CN-75	5.6Nb-6XM-6XO	1300 (189)	2080 (302)	16.2

*HIPped at 1450°C and annealed 3 d/1100°C.

effective in improving both the strength and ductility of the CN alloys containing 5.6-6% Nb at room temperature (Table 4). The alloy CN-65 containing 5.6% Nb and 6% XM showed a yield strength of 1097 MPa and a ductility of 18.5% at room temperature. Alloying with 6% XO together with 6% XM appears not to lower the room-temperature ductility of the 5.6% Nb alloy.

At 1000 and 1200°C, both XM and rhenium effectively increase the compressive strength of the CN alloys containing 5.6 and 12% Nb (Table 5). The ductility of the alloys is not sensitive to alloying additions, and all the alloys showed ductility of more than 23%. HIPping at 1450°C appears not to affect the ductility at either room or elevated temperatures. The CN alloys are much stronger than Ni-base superalloys, whose strength drops to about zero at 1200°C.

Table 5. Compressive Properties of CN Alloys Tested at 1000 and 1200°C in Vacuum

Alloy No.	Concentration of Key Elements (at.%)	Strength, MPa (ksi) Yield	Ultimate	Ductility (%)
		1000°C		
CN-4	12Nb	685 (99)	856 (124)	22.8
CN-44	12Nb-4Re	855 (124)	1061 (154)	26.2
CN-60	12Nb-4Re-6XM	896 (130)	1632 (237)	29.2
CN-61	12Nb-4Re-4XO	741 (107)	1257 (182)	28.5
CN-7	6.0Nb	436 (63)	738 (107)	32.7
CN-65	5.6Nb-6XM	634 (92)	1203 (174)	33.8
CN-68	5.6Nb-4Re-6XM	675 (98)	1118 (162)	26.5
CN-70*	5.6Nb-0.1B-6XM	778 (113)	1394 (202)	23.1
CN-75	5.6Nb-6XM-6XO	710 (103)	1302 (189)	32.4
		1200°C		
CN-4		363 (53)	487 (71)	>31.5
CN-44		432 (63)	566 (82)	> 4.1
CN-60		535 (78)	664 (96)	> 5.6
CN-61		393 (57)	599 (87)	>30.0
CN-7		258 (37)	309 (45)	31.4
CN-65		404 (59)	547 (79)	30.4

*HIPped at 1450°C.

Tensile Properties

Tensile properties of HIPped and/or directionally solidified specimens were determined at room temperature and 1000°C. As mentioned before, these specimens contain cast defects (even after HIPping), and only the highest fracture strength for each alloy are reported in Table 6. The alloys showed a fracture strength at a level of 200-500

MPa, which appears to be independent of alloy composition. There is no apparent difference in fracture strength at room temperature and 1000°C, suggesting that the fracture process is dominated by cast defects in the alloys. Further studies are required to reduce cast defects by either HIPping at higher temperature (>1580°C) or hot extruding the CN alloys. A recent study of two-phase alloys based on Nb and Nb_5Si_3 indicates that their tensile ductility and strength can be dramatically improved by hot extrusion of the alloys at 1426°C.

Table 6. Tensile Properties of CN Alloys Tested at Room Temperature in Air and 1000°C in Vacuum

Alloy No.	Alloy Composition (at.%)	Treatment Condition*	Fracture Stress, MPa (ksi)
	Room Temperature		
CN-70	Cr-5.6Nb-1.5Al-0.1B-6XM	HIP/1450°C	326 (47.3)
CN-65	Cr-5.6Nb-1.5Al-0.1Zr-6XM	HIP/1580°C	487 (70.7)
CN-65	Cr-5.6Nb-1.5Al-0.1Zr-6XM	DS	367 (53.3)
CN-67	Cr-8Nb-1.5Al-0.1Zr-6XM	DS/HIP/1580°C	207 (30.1)
CN-74	Cr-5.6Nb-1.5Al-0.1Zr-6XM-4XO	HIP/1580°C	416 (60.4)
	1000°C		
CN-70	Cr-5.6Nb-1.5Al-0.1B-6XM	HIP/1450°C	478 (69.4)
CN-65	Cr-5.6Nb-1.5Al-0.1Zr-6XM	HIP/1580°C	360 (52.2)
CN-67	Cr-8Nb-1.5Al-0.1Zr-6XM	DS/HIP/1580°C	382 (55.5)
CN-74	Cr-5.6Nb-1.5Al-0.1Zr-6XM-4XO	HIP/1580°C	248 (36.0)

HIP = hot isostatically pressing
DS = directional solidification by levitation zone remelting

Fracture surfaces of the tensile specimens tested at room temperature and 1000°C were examined using a scanning electron microscope operated at 10 kV. The CN alloys showed mainly cleavage fracture at both temperatures with a more ductile appearance at 1000°C. Cast defects are visible on the fracture surfaces.

Creep Resistance

We recently initiated creep tests of CN alloys containing XM. The alloy CN-70 showed no measurable creep deformation at 1200°C at a stress of 55 MPa (8 ksi), indicating excellent creep resistance. The alloy exhibited a creep rate of 1.5×10^{-7} h^{-1} at

1000°C at a stress of 345 MPa (50 ksi). The alloy is much more creep resistant than Ni-base superalloys.

ACKNOWLEDGMENTS

The authors are grateful to Ben Oliver (University of Tennessee) for processing of the alloys by levitation-zone remelting, Tommy Henson for electron microprobe analyses, Dewey Easton for x-ray fluorescence analyses, and Joe Wright and Elmer Lee for metallography. Thanks are also due to Sharon Kneé for preparation of the manuscript. This research is sponsored by the U.S. Department of Energy, Office of Fossil Energy, Advanced Research and Technology Development Materials Program [DOE/FE AA 15 10 10 0, Work Breakdown Structure Element ORNL-4A] under contract DE-AC05-84OR21400 with Martin Marietta Energy Systems, Inc.

REFERENCES

1. F. Laves, in T*heory of Alloy Phases*, American Society for Metals, Metals Park, OH, 1956, p. 124.
2. H. J. Goldschmidt and J. A. Brand, J. *Less-Common Met.* **3**, 44 (1961).
3. T. B. Massalski, J. L. Murray, L. H. Bennett, and H. Baker (eds.), *Binary Alloy Phase Diagram*, American Soceity for Metals, Metals Park, OH, 1986.
4. A. I. Taub and R. L. Fleischer, *Science* **243**, 616 (1989).
5. M. Takeyama and C. T. Liu, *Mat. Sci. and Eng.* **A132**, 61 (1991).
6. J. D. Livingston, *Phys. Stat. Sol.* (a)**131**, 415 (1992).
7. C. T. Liu, pp. 375-383 in *Proc. 6th Annual Conf. on Fossil Energy Materials*, ORNL/FMP-9211, Oak Ridge National Laboratory, July 1992.
8. C. T. Liu, J. A. Horton, and C. A. Carmichael, pp. 297-307, in *Proc. 7th Annual Conf. on Fossil Energy Materials*, ORNL/FMP-93/1, Oak Ridge National Laboratory, July 1993.
9. M. D. Bhandarkar, M. S. Bhat, V. F. Zackay, and E. R. Parker, *Metall. Trans.* **6A**, 1281 (1975).
10. M. D. Bhandarkar, M. S. Bhat, E. R. Parker, and V. F. Zackay, *Metall. Trans.* **7A**, 753 (1976).
11. Y. Liu, J. D. Livingston, and S. M. Allen, *Metall. Trans. A*, **23A**, 3303 (1992).
12. K. C. Chen, S. M. Allen, J. D. Livingston, p. 373 in MRS Proc. Vol. 288, ed. Baker et al. (1993).
13. Y. Liu, S. M. Allen, and J. D. Livingston, p. 203 in MRS Proc. Vol. 288, ed. Baker et al. (1993).
14. R. L. Fleischer, *Scr. Metall.* **27**, 1799 (1992).
15. D. L. Anton and D. M. Shah, p. 733 in MRS Proc. Vol. 213, ed. Johnson et al. (1991).
16. G. E. Vignoul, J. M. Sanchez, and J. K. Tien, p. 739 in MRS Proc. Vol. 213, ed. Johnston et al. (1991).

17. P. F. Tortorelli and J. D. DeVan, pp. 229-236 in Proc. Symp. on *Oxide Films on Metals and Alloys*, B. R. MacDougall, R. S. Alwitt, and T. A. Ramanarayanan (eds.), Proceedings Vol. 92-22, The Electrochemical Society, 1992.

18. P. F. Tortorelli, L. J. Carsen, and J. H. DeVan, pp. 309-318 in *Proc. 7th Annual Conf. on Fossil Energy Materials*, ORNL/FMP-93/1, Oak Ridge National Laboratory, July 1993.

19. P. F. Tortorelli and J. H. DeVan in this procs.

20. M. G. Mendiratta and D. M. Dimiduk, *Metall. Trans. A.* **24A**, 501 (1993).

21. M. G. Mendiratta, J. J. Lewandowski, and D. M. Dimiduk, *Metall. Trans. A* **22A**, 1573 (1991).

ALLOYING EFFECTS ON THE HIGH-TEMPERATURE OXIDATION RESISTANCE OF Cr-Cr_2Nb

P. F. Tortorelli and J. H. DeVan

Oak Ridge National Laboratory
Metals and Ceramics Division
P. O. Box 2008
Oak Ridge, Tennessee 37831-6156

ABSTRACT

Alloying effects on the high-temperature oxidation resistance of Cr-Cr_2Nb were examined on the basis of isothermal exposures to air at 950°C. Additions of either Re and Al or Fe, Ni, and Al had relatively little effect on weight gains relative to the Cr - 6% Nb binary alloy. One alloying element that improved the mechanical behavior of Cr-Cr_2Nb alloys substantially increased the oxidation rates and spallation susceptibilities of Cr - 6 and - 12% Nb alloys. However, the addition of another element completely offset these deleterious effects. The presence of this latter element resulted in the best overall oxidation behavior (in terms of both weight gains and spallation tendencies) of all Cr-Cr_2Nb compositions. Its beneficial effect can be attributed to improvement in the oxidation resistance of the Cr-rich phase.

INTRODUCTION

Chromium-based alloys incorporating the Cr_2Nb Laves-phase are potential new materials for use in hostile environments of advanced heat engines and energy systems that operate at very high temperatures.[1,2] The intermetallic Cr_2Nb phase, with a C-15 complex cubic structure,[3] has a high-melting point (1770°C)[4-5] and relatively low density (7.7 g/cm^2).[6] Results to date indicate that the two-phase Cr_2Nb/Cr(Nb) alloys have excellent strength for structural use at high temperatures (1000-1200°C).[1,2,7,8] However, such alloys suffer from poor toughness and fracture resistance. Current development efforts are focused on improving these properties as well as evaluating the high-temperature oxidation resistance of Cr-Cr_2Nb alloys under relevant metallurgical and environmental conditions. Relatively low oxidation rates over extended periods of time are necessary for deployment of such alloys at the high temperatures envisioned for potential applications.

Previously-reported oxidation results showed that elevated-temperature (900 and 950°C) exposures of Cr-Cr_2Nb alloys containing 6 and 12 % Nb resulted in multilayer scales with an outer layer of chromia and inner products containing niobium.[8] (All

concentrations are in at. %.) Spallation and indirect evidence of isothermal scale cracking were observed. The alloy with the higher concentration of niobium showed better oxidation resistance in terms of weight gain and scale adherence.[8] This was attributed to its greater volume fraction of the Cr_2Nb-Cr eutectic at the expense of the Cr-rich phase. While parabolic kinetics were observed at 900, 950, and 1000°C, an isothermal exposure temperature of 1100°C led to accelerated reaction of binary Cr-12% Nb manifested in the form of breakaway oxidation.[9] Alloying additions of Al (up to 18%) or Re (2%) did not improve the isothermal oxidation resistance of Cr-12% Nb, nor did the reduction in the level of impurities.[9] Further studies have now been conducted to evaluate effects of other alloying additions on the isothermal oxidation resistance of Cr-Cr_2Nb alloys in air and form the basis of the present paper. The work has been mainly focused on 6% Nb alloys as these have been shown the most promise in improving room-temperature compressive ductility.[2]

EXPERIMENTAL PROCEDURES

Alloys of Cr-Cr_2Nb were prepared by arc melting and drop casting into water-cooled copper molds. High-purity niobium and chromium metal chips were used as charge materials, and the alloys were melted in a high vacuum (10^{-5} Pa) furnace. Details regarding alloy preparation and processing are described elsewhere.[2,10] Table 1 lists the alloy compositions discussed in this paper. As described below, the element referred to as XM was effective in refining the interconnected eutectic structure and improving mechanical behavior, while XO was beneficial to oxidation resistance. (These two elements cannot be currently disclosed due to patent considerations.) Rectangular specimens (approximately 8 x 8-16 x 1 mm) were cut or machined from as-cast or homogenized (1100°C, 3 days, vacuum) ingot pieces. All major surfaces were mechanically ground with 600-grit SiC abrasive before exposure.

Weight changes due to isothermal oxidation were measured using Cahn 1000 microbalances and a computer-controlled data acquisition system. The specimens were exposed to flowing, preheated, dried air (2 cc/s) at 950°C for up to 180 h. At the end of each experiment, the specimens were furnace cooled and visually checked for loss of corrosion products by spallation. Selected specimens were analyzed by scanning electron microscopy (SEM).

Table 1. Nominal compositions of alloys used in this study.

Alloy No.	Concentration (at.%)[a]					
	Nb	Al	Re	XM	XO	Zr
CN-4	12					
CN-7	6					
CN-52[b]	5.6	1.5	4			
CN-53[c]	5.6	1.5				
CN-60	12	2	4	6		
CN-61	12	2	4		4	
CN-65	5.6	1.5		6		0.1
CN-73[d]	5.6	1.5		6		0.1
CN-74	5.6	1.5		6	4	0.1
CN-75	5.6	1.5		6	6	0.1
CN-76	5.6	1.5		6	8	0.1

[a] Balance is Cr. Identities of elements denoted as XM and XO cannot be currently disclosed due to patent considerations

[b] 0.1% Hf

[c] 2% Fe, 2% Ni, 0.1% Hf

[d] Other ≤ 0.1%

RESULTS

Figure 1 compares the weight gain behavior of several 5.6% Nb alloys exposed to air at 950°C. Additions of either Re and Al (CN52) or Fe, Ni, and Al (CN53) had little effect on weight gains relative to the Cr - 6% Nb binary alloy (CN7). On the other hand, XM had a severe detrimental influence: the weight gains and rates for the alloys with 6% XM (CN65 and CN73) were substantially higher than for the XM-free compositions. The XM-containing alloys showed linear kinetics rather than the parabolic behavior associated with formation of protective oxide scales. As shown in Fig. 2, XM had a similar, although somewhat less dramatic, effect on the thermogravimetric results for Cr-Cr_2Nb alloys with 12% Nb.

Figure 2 also indicates that the presence of XO in Cr - 12% Nb (CN61) results in oxidation behavior that is comparable to, or slightly better than, that of the binary composition. Because of this, the combined effect of XM and XO on air oxidation resistance was examined through exposures of alloys CN74, CN75, and CN76 (see Table 1). The results from this series of exposures are shown in Figs. 3 and 4. The data in Fig. 3 indicate a substantial improvement in oxidation behavior when 4 - 8% XO is

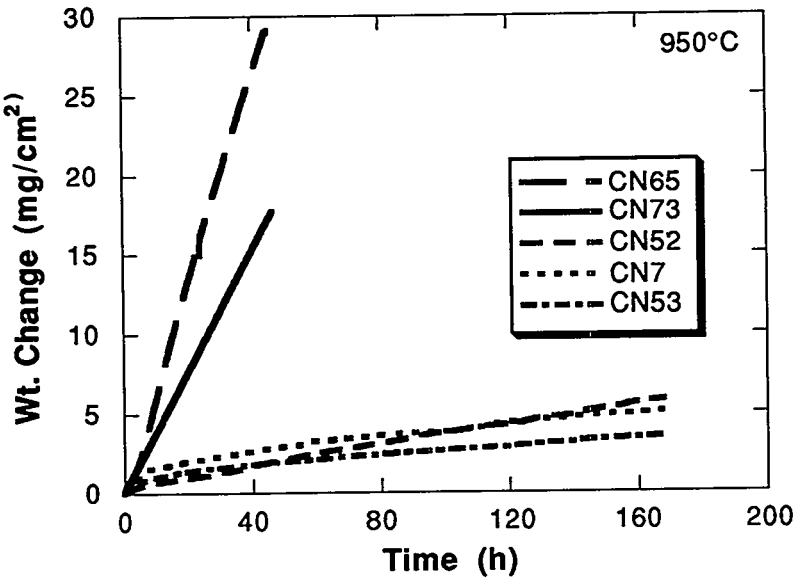

Fig. 1. Weight change versus time for Cr-~6% Nb alloys oxidized in air at 950°C.

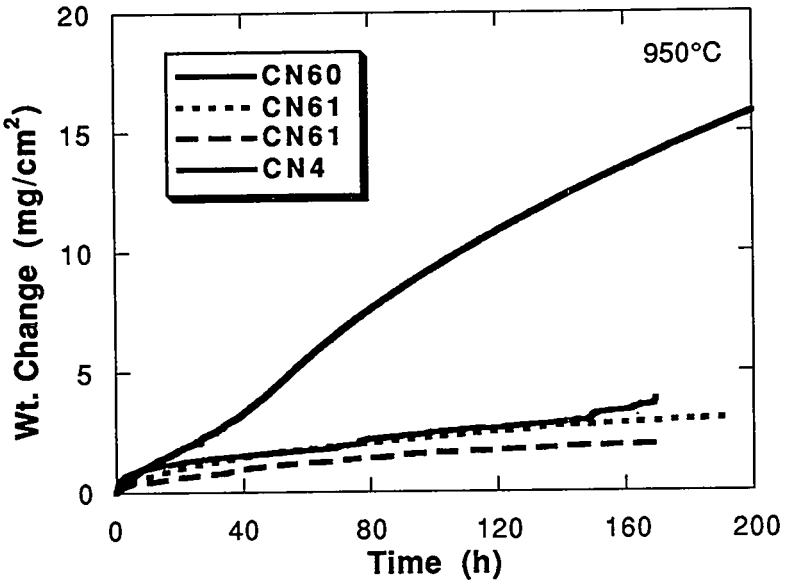

Fig. 2. Weight change versus time for Cr-12% Nb alloys oxidized in air at 950°C. Results from duplicate specimens of CN61 are included.

present in XM-containing alloys. In Fig. 4, the thermogravimetric results for the alloys with XM + XO are compared to those for CN61 and the Cr - 6% and - 12% binary compositions.[8] Alloys CN74, CN75, and CN76 (5.6% Nb) had smaller weight gains and rates than Cr - 6% Nb (CN7) and also compared favorably to Cr - 12% Nb (CN4). The differences in the thermogravimetric results among the three Cr - 5.6% Nb - 6% XM - XO compositions were insignificant (Fig. 4). Oxidation rates of XO-containing alloys

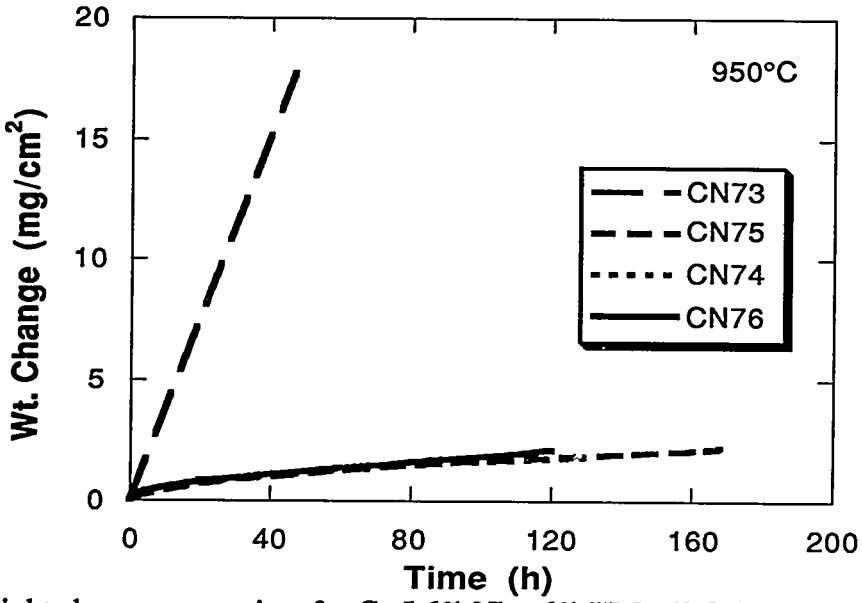

Fig. 3. Weight change versus time for Cr-5.6% Nb - 6% XM - (0-8%) XO alloys oxidized in air at 950°C. The curves for CN-74 and CN-75 are essentially identical.

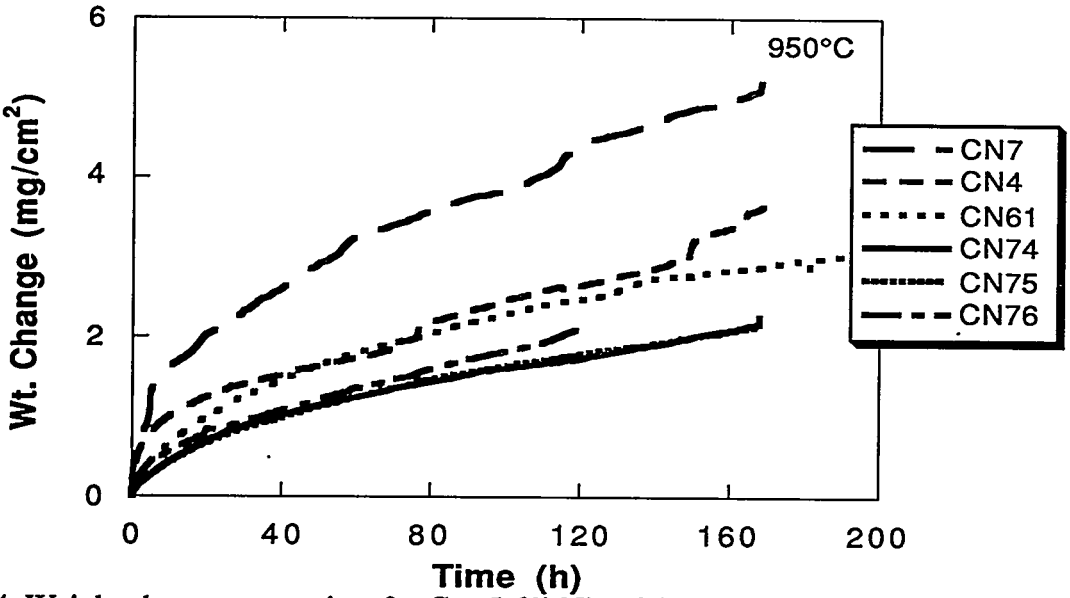

Fig. 4. Weight change versus time for Cr - 5.6% Nb - 6% XM - (4-8%) XO, Cr - 12% Nb - 4% XO, Cr - 6% Nb, and Cr - 12% Nb alloys oxidized in air at 950°C. The curves for CN-74 and CN-75 are essentially identical.

appeared to be relatively insensitive to the concentration of this element in the range investigated (4 - 8%). Furthermore, there was essentially no difference between the weight change results for the Cr - 5.6% Nb - 6% XM - XO alloys and that of Cr - 12% Nb - 4% XO (CN61). Indeed, in contrast to the difference in oxidation behavior of CN7 and

CN4 (ref. 8 and Fig. 4), the presence of XO appeared to eliminate differences in oxidation resistance observed for the binary 6 and 12% Nb alloys.

In order to ascertain whether significant differences in oxidation behavior could be due to certain microstructural differences, several of the alloys listed in Table 1 were exposed in both the as-cast and homogenized conditions. In isolated cases, an as-cast alloy showed extremely high weight gains. However, the typical differences in isothermal oxidation behavior were small, with the as-cast specimens showing slightly higher weight gains than the homogenized versions of the same composition (Fig. 5). Therefore, in general, such differences in starting microstructure did not appear to change the relative effects of the observed influences of compositional modifications.

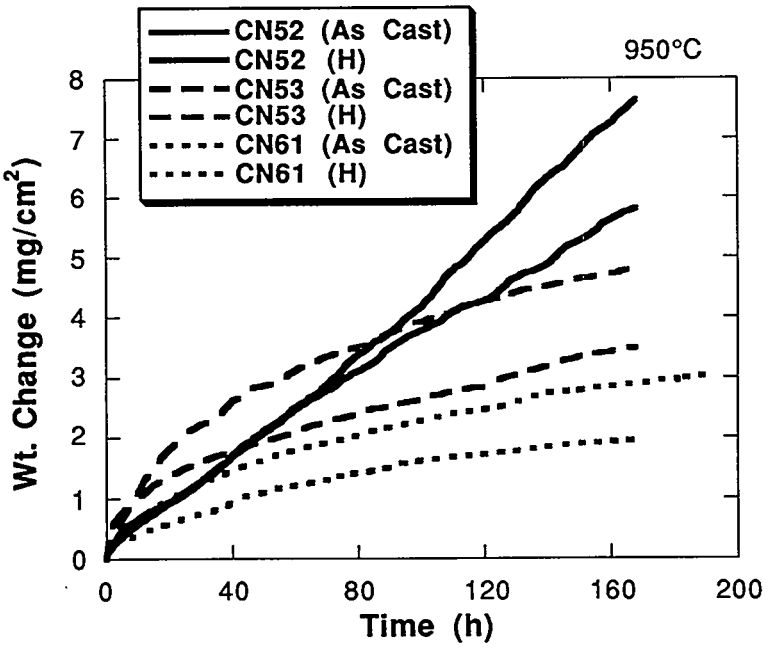

Fig. 5. Weight change versus time for as-cast and homogenized (H) Cr - Cr_2Nb alloys oxidized in air at 950°C.

The results of visual examination of specimen surfaces after cooling to room temperature following isothermal exposure at 950°C are given in Table 2. A significant variation in spallation tendency was noted. Alloys with XM suffered extensive spallation, while those with XO showed much less scale loss. An example of a specimen that suffered substantial spallation (CN60, see Table 1) is shown in Fig. 6. Note the scale cracking and multiple layers of surface products.

Table 2. Summary of visual observations of Cr-Cr_2Nb specimens after isothermal exposure to air for 150 to 180 h at 950°C.

Alloy	% Area Showing Some Spallation	Appearance of Scale(s)
CN52	25-50[(a)]	upper scale gray; lower: green-gray
CN53	<10	gray
CN60	75	gray and dark gray
CN61	<10[(a)]	gray
CN65	100	many large gray fragments; surface dark gray
CN73	100	many large gray fragments; surface dark gray
CN74	25-50[(a)]	upper scale gray; lower: green-gray
CN75	<10	gray
CN76	25[(a)]	upper scale gray; lower: dark and light gray

[(a)] Duplicate specimens

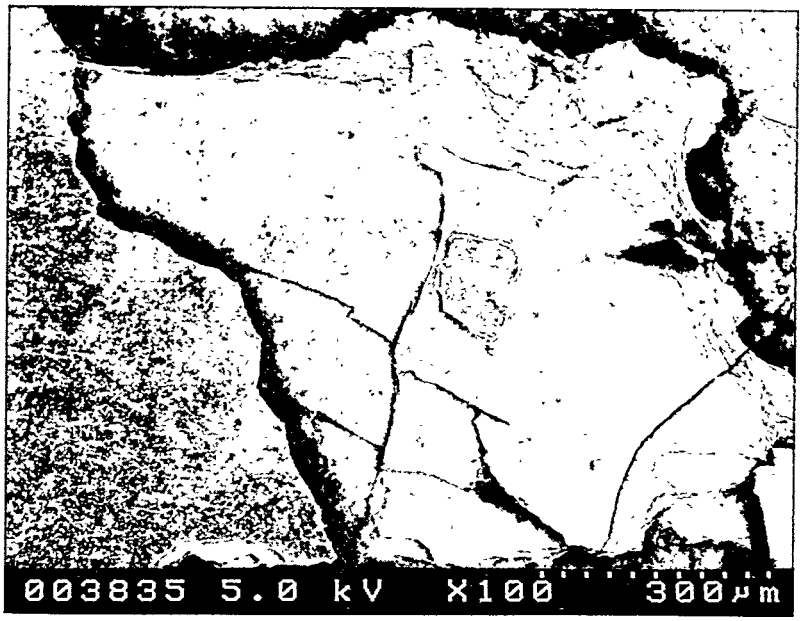

Fig. 6. Scanning electron micrograph of oxidized surface of Cr - 12% Nb - 4% Re - 2% Al - 6% XM after cooling from the isothermal exposure temperature of 950°C.

DISCUSSION

The alloys of the present study are in the hypoeutectic part of the Cr-Cr_2Nb two-phase region. The eutectic (17 at. % Nb) is composed of a Cr_2Nb matrix with a dispersion of Cr-rich material and Cr-rich regions with very fine Cr_2Nb precipitates.[1] It was previously shown that the oxidation of Cr -6 and -12 at. % Nb alloys in air at 950°C led to the formation of multilayer scales with an outer layer of chromia and inner products containing niobium.[8] A porous inner layer preferentially formed on a Cr-rich phase.[8] The alloy with the higher concentration of niobium showed better oxidation resistance in terms

of weight gain and scale adherence. Because the increase in niobium concentration from 6 to 12% results in a higher volume fraction of the eutectic mixture, the poorer overall oxidation resistance of the 6% Nb alloy appeared to be related to the greater abundance of the Cr-rich phase.[8]

The presence of the element denoted as XM refines the coarse eutectic structure of Cr-Cr_2Nb and, in so doing, substantially improves the compressive strength and ductility of the alloys.[10] However, the present results clearly indicate that this element has a substantial deleterious effect on the oxidation behavior of Cr - 6 and -12 % Nb alloys (Figs. 1 and 2). The rates of weight gain, and spallation tendencies, of alloys containing 6% XM are significantly greater than those shown by any of the other compositions. For 5.6% Nb - 6% XM alloys, the oxidation rates were approximately linear (Fig. 1). Indeed, this set of XM-containing alloys appeared more susceptible to air oxidation than the Cr-12% Nb-XM composition (compare Figs. 1 and 2). As such, this dependence on niobium content is consistent with the results of the earlier study of binary 6 and 12% Nb alloys.[8] The conversion of the interconnected Cr_2Nb-phase into a finer distribution (mainly for the 12% Nb alloy)[10] does not appear to be beneficial to oxidation resistance. Any microstructural influence, however, is probably secondary to direct chemical effects of the presence of XM on the overall oxidation behavior of these alloys.

The marked detrimental influence of XM on the oxidation behavior of Cr-Cr_2Nb can be completely offset by the addition of XO (see Fig. 3). Liu, Horton, and Carmichael have shown that XO strongly partitions to the Cr_2Nb(Cr) phase and stabilizes the eutectic structure.[10] Such a concentration of XO in the eutectic phase can decrease its susceptibility to reaction with oxygen and, when combined with the observed morphology of the Cr_2Nb(Cr), positively affect oxidation resistance. However, it is believed that it is the smaller concentration of XO in the Cr-rich phase that is actually the cause of improved overall oxidation behavior of the XO-containing alloys. This element has a known beneficial effect for chromia-forming systems, and, as the Cr-rich phase is thought to be the more susceptible microstructural component,[8] improvement in its oxidation resistance can have a substantial effect on weight gains and spallation resistance.

Corroboration of the role of XO in preferentially improving the oxidation resistance of the Cr-rich regions of Cr-Cr_2Nb alloys awaits microstructural analysis of properly prepared cross sections. However, there are specific results that tend to support such an influence of XO. Figure 4 shows that there is little difference in the isothermal oxidation

behavior between XO-containing 6 and 12% Nb alloys (that is, between alloys with different volume fraction ratios of the two phases). This is in contrast to previous findings (described above and in ref. 8) and supports the hypothesis that XO is specifically increasing the oxidation resistance of the Cr-rich phase. If the XO additions acted to preferentially improve the oxidation resistance of the eutectic phase, differences in behavior between 6 and 12% Nb alloys should increase, which is the opposite effect to what is shown by the present data. Furthermore, while there is definite evidence that scale cracking occurs for Cr-6 and -12% Nb alloys during isothermal exposure at 900 and 950°C,[8,9] the discontinuities in the thermogravimetric curves that typically indicate such processes[11] are not observed for the XO-containing alloys (compare the results for CN74, C75, and CN76 with those for CN4 and CN7). This finding suggests that the presence of this element reduces the susceptibility for isothermal scale cracking normally observed for the binary Cr-Cr_2Nb alloys. As much of the scale cracking and the spallation during subsequent cooldown appeared related to the Cr-rich regions,[8,9] the presence of a small concentration of XO in the Cr-rich phase can therefore significantly improve the oxidation of the alloys by reducing cracking and the resulting accelerated oxide growth and loss of product.

As described above, it was previously reported that 12% Nb alloys were superior in oxidation behavior to the 6% alloys.[8] Subsequent work with other alloys did not reveal any compositional modifications that improved the behavior to the point where they matched or exceeded that of the 12% Nb binary composition.[9] The present results show that, regardless of the presence of XM, the effect of XO is to improve the overall oxidation resistance (in terms of both weight gains and spallation, see Table 2) such that those alloys containing this element show the best behavior of any Cr-Cr_2Nb composition examined to date. As the differences in the isothermal oxidation results among the three Cr - 5.6% Nb - 6% XM - XO compositions are quite small (similar weight gains and rate constants for 4, 6, and 8% XO, Fig. 4), the choice of the appropriate XO level can be based on mechanical properties (or other) considerations.[10]

SUMMARY AND CONCLUSIONS

The effects of several alloying additions on the high-temperature oxidation resistance of Cr-Cr_2Nb were examined on the basis of isothermal exposures to air at 950°C. Additions of either Re and Al or Fe, Ni, and Al had relatively little effect on weight gains relative to the Cr - 6% Nb binary alloy. One alloying element that improved the

mechanical behavior of Cr-Cr_2Nb alloys substantially increased the oxidation rates and spallation susceptibilities of Cr - 6 and - 12% Nb alloys. However, the addition of another element completely offset these deleterious effects. The presence of this latter element resulted in the best overall oxidation behavior of all Cr-Cr_2Nb compositions and provides the opportunity to improve the mechanical properties of this alloy system without necessarily compromising oxidation resistance. The effects of this element were manifested as relatively low weight gains, substantially reduced scale cracking and spallation, and elimination of the dependence of oxidation behavior on niobium content (that is, on the relative amounts of the Cr-rich and eutectic phases). Its beneficial influence can be attributed to improvement in the oxidation resistance of the Cr-rich phase, which otherwise showed preferential susceptibility to degradation upon exposure to high-temperature air.

ACKNOWLEDGMENTS

The authors thank M. Howell for experimental support, A. M. Williams for microscopy, and C. T. Liu, J. R. Keiser, and R. E. Pawel for their reviews of the manuscript. This research was sponsored by the Fossil Energy Advanced Research and Technology Development (AR&TD) Materials Program, U S. Department of Energy, under contract DE-AC05-84OR21400 with Martin Marietta Energy Systems, Inc.

REFERENCES

1. M. Takeyama and C. T. Liu, "Microstructure and Mechanical Properties of Laves-Phase Alloys Based on Cr_2Nb," *Mater. Sci. Eng.* **A132**, 61, (1991).

2. C. T. Liu, J. A. Horton, and C. A. Carmichael, pp. 297-307, in *Proc. 7th Annual Conf. on Fossil Energy Materials*, ORNL/FMP-93/1, Oak Ridge National Laboratory, July 1993.

3. F. Laves, in *Theory of Alloy Phases*, American Society for Metals, Metals Park, OH, 1956, p. 124.

4. H. J. Goldschmidt and J. A. Brand, J. *Less-Common Met.* **3**, 44 (1961).

5. T. B. Massalski, J. L. Murray, L. H. Bennett, and H. Baker (eds.), *Binary Alloy Phase Diagram*, American Society for Metals, Metals Park, OH, 1986.

6. A. I. Taub and R. L. Fleischer, *Science* **243**, 616 (1989).

7. C. T. Liu, pp. 375-383 in *Proc. 6th Annual Conf. on Fossil Energy Materials*, ORNL/FMP-9211, Oak Ridge National Laboratory, July 1992.

8. P. F. Tortorelli and J. H. DeVan, "The Nature of Scales Grown on Binary Cr-Nb Alloys," pp. 229-236 in *Proc. Symp. on Oxide Films on Metals and Alloys*, B. R. MacDougall, R. S. Alwitt, and T. A. Ramanarayanan (eds.), Proceedings Vol. 92-22, The Electrochemical Society, 1992.

9. P. F. Tortorelli, L. J. Carson, and J. H. DeVan, pp. 309-318 in *Proc. 7th Annual Conf. on Fossil Energy Materials*, ORNL/FMP-93/1, Oak Ridge National Laboratory, July 1993.

10. C. T. Liu, J. A. Horton, and C. A. Carmichael, these proceedings.

11. P. Kofstad, *High Temperature Corrosion*, Elsevier Applied Science, London, 1988.

Fracture Behavior of Cr_2Nb-based Intermetallics

J. A. Cook[1], P. K. Liaw[1], and C.T. Liu[2]

1. Department of Materials Science and Engineering
434 Dougherty Eng. Bldg.
University of Tennessee
Knoxville, TN 37996-2200

2. Oak Ridge National Laboratory
P.O. Box 2008
Oak Ridge, TN 37831-6084

ABSTRACT

Microstructural evaluations of Laves-phase alloys based on Cr_2Nb were examined in order to determine phase relationships with heat treating temperatures up to 1580°C. At ambient temperatures, single-phase Cr_2Nb alloys are very hard and brittle due to the difficulty in generation and glide of dislocations because of the complicated crystal structure (C-15). The following results were revealed through examination of the Cr-Cr_2Nb two-phase region: (a) with increasing amounts of the soft chromium-rich phase, the hardness decreases; (b) the heat treatments studied provided the best dispersion of the chromium-rich phase in the Cr - 6 at.% Nb (CN-7) alloy; (c) an anneal of 3 days at 1100°C + 1 hour at 1580°C provided for the best dispersion of the Cr-rich phase and break-up of the Laves-type phase in the CN-7 alloy. Previous studies have shown [1] that the introduction of a soft chromium phase has promising effects in improving the mechanical properties of brittle Cr_2Nb Laves-phase alloys.

INTRODUCTION

The goal of this work is to develop a new generation of high-strength, corrosion-resistant intermetallic alloys based on Cr_2Nb for use as critical hot components in advanced fossil energy conversion systems.

The Cr_2Nb Laves phase has a cubic crystal structure (C-15) with a stacking sequence of an XYZ type, where X, Y, and Z represent closed-packed layers, similar to an f.c.c. structure; however, with each layer being composed of four interpenetrating atomic layers. The unit cell contains 24 atoms and has a lattice constant of 6.98 Å [2-5].

This Laves-phase alloy has been selected for this development because of its high melting point (1770°C) [6-7], relatively low density (7.7g/cm^2) [8], and potential resistance to oxidation and corrosion [6].

The most important concern with Cr_2Nb as well as other A_2B Laves phases is their poor ductility and fracture toughness at ambient temperatures [1,6,9]. Since the single-phase Cr_2Nb is very hard [800 Diamond Pyramid hardness (DPH)] and brittle at ambient temperatures, the efforts of alloy development have been placed on the Cr-Cr_2Nb two-phase compositions containing the intermetallic phase Cr_2Nb and the chromium-rich solid solution phase [1]. Previous studies have indicated that the two-phase Cr_2Nb alloys showed plastic deformation under compression at room temperature, with much greater strength than nickel-base superalloys at and above 1000°C [1,10].The results obtained to date indicate that the Cr-Cr_2Nb alloys have excellent strength for structural use at ultrahigh temperatures (i.e. 1000-1300°C) [1,10].

Work performed by Takeyama and Liu has indicated the following: (a) the eutectic composition has a niobium concentration of 17 at.% rather than 12 at.% as reported in the phase diagram shown in Figure 1 which was given by Goldschmidt [6,7]; (b) the soft regions are effective in preventing crack propagation originating in the brittle Laves-phase, which results in a high yield strength with moderate ductility up to 1000°C [1].

The potential applications of this Laves-phase alloy include hot components in advanced fossil energy conversion systems, advanced heat engines, and high-temperature cutting and grinding tools [11]. It has been shown [1] that the mechanical and metallurgical properties of the Cr-Cr_2Nb alloys can be improved through dispersion of the ductile Cr-rich phase or the break-up of the brittle Cr_2Nb phase. This paper summarizes our recent alloy development effort on controlling the dispersion of the Cr-rich phase and the break-up of the Laves-phase (Cr_2Nb) in the Cr-rich matrix by means of thermomechanical treatment.

EXPERIMENTAL PROCEDURE

Chromium-niobium alloys weighing 350g were prepared by arc melting and drop casting into pre-heated copper molds. High-purity niobium and chromium metal chips were used as charge materials in order to reduce the interstitial impurity (i.e. oxygen), and the alloys were melted in a high vacuum (10^{-5} Pa) furnace. The preheating of the copper mold to 100°C before drop casting was done in order to control alloy solidification and to reduce microporosity formation during drop casting [11].

Table 1 lists the composition (at.%) of CN(Cr-Nb) alloys investigated in this work. The alloys used in this study have nominal compositions of chromium with a variation of 6 to 17 at.% Nb. The alloys were placed in a covered alumina crucible and annealed at 1100°C for 3 d (days) + 1 h (hour) at 1400°C, 1500°C, 1550°C, or 1580°C under vacuum (10^{-6} Pa) for a total of four specimens per alloy studied. The effects of annealing, 1 hour at 1400, 1500, 1550, or 1580°C after 3 d at 1100°C, on the microstructures of the CN alloys were emphasized in this investigation.

Table 1. Alloy Compositions for the Cr_2Nb-based Intermetallics

Alloy	Atomic percent	Weight percent
CN-7	Cr - 94 % Nb - 6 %	Cr - 89.76% Nb - 10.24%
CN-4	Cr - 88 % Nb - 12 %	Cr - 80.41% Nb - 19.59%
CN-45	Cr - 83 % Nb - 17 %	Cr - 73.21% Nb - 26.79%

Microstructures of these alloys were examined by optical and scanning electron microscopy. The metallographic specimens were polished to 1 μm using an alumina slurry. Samples were etched in a solution of 15 gm KOH, 15 gm $K_3Fe(CN)_6$, and 90 ml H_2O for approximately 5 seconds. Microhardness readings were taken for each specimen using a LECO M-400 Hardness Tester. An average of three to five readings taken randomly across the sample gives the reported hardness values.

RESULTS AND DISCUSSION

Microstucture and Phase Composition

The CN alloys contain two phases, the Cr_2Nb intermetallic phase and the chromium-rich solid solution which can contain up to as much as 5 at.% Nb at the eutectic temperature of 1620°C.

The composition of the phases in the alloys CN-7, CN-4, and CN-45 was determined by semi-quantitative EDS analyses as reported in Table 2. Figure 2(a) shows the optical micrograph of CN-7 heat treated for 3d/1100°C + 1 h at 1400°C. In the Cr-6 at.% Nb (CN-7) alloy, Cr-rich patches cover most areas, and a small amount of the Laves-phase is seen as a network along the Cr-rich patches [Fig. 2(a)]. The Cr-12 at.% Nb (CN-4) alloy is shown in Figure 2(b) with the same annealing history as CN-7 in Figure 2(a). In this condition (CN-4), the lighter patches are the chromium-rich matrix phase surrounded by the Laves-phase, indicating that this is a hypoeutectic structure. Some dark spots can be seen within the Cr-rich patches, and these spots are the Cr_2Nb particles that are formed during cooling.

Table 2. Semi-quantitative EDS analysis of CN-7, CN-4 and CN-45

Alloy	Temperature (C°)	Laves-type phase (at. %)	Cr-rich phase (at. %)
CN -7	3d/1100 + 1h/1400	Cr = 90.1 Nb = 9.9	Cr = 98.2 Nb = 1.8
	3d/1100 + 1h/1580	Cr = 72.9 Nb = 27.1	Cr = 97.3 Nb = 2.7
CN -4	3d/1100 + 1h/1400	Cr = 80.1 Nb = 19.9	Cr = 97.2 Nb = 2.8
	3d/1100 + 1h/1580	Cr = 75.7 Nb = 24.3	Cr = 97.3 Nb = 2.7
CN -45	1h/1400	Cr = 85.8 Nb = 14.2	Cr = 96.4 Nb = 3.6
	1h/1580	Cr = 76.3 Nb = 23.7	Cr = 97.3 Nb = 2.7

It has been shown [11] that the precipitation of the Cr_2Nb Laves-phase particles from the Cr-rich phase is indeed sluggish. These precipitates are extremely fine, with a size of less than 1 μm for an alloy annealed for 3 days at 1100°C [1]. Heat treating at temperatures of 3d/1100°C + 1h at 1550 or 1580°C did not reveal the fine Cr_2Nb particles within the Cr-rich phase. These precipitates were partially dissolved due to an increase in the solubility of Nb in Cr at these temperatures and the remainder of the particles went into the Laves-type phase, thereby coarsening it. Thus, we see that there are two competing mechanisms occurring during the annealing treatment; (1) break-up of the Laves-type phase and (2) coarsening of the Laves-type phase due to Cr_2Nb particles migrating from the Cr-rich phase at high temperatures. Heat treatments at 1400 and 1500°C did not have much of an effect on the Cr_2Nb precipitates in the Cr-rich phase from the 3 day anneal at 1100°C. These results can be verified by the increased amounts of niobium seen in the Laves-type phase for the 1580°C anneal as reported in Table 2 for both CN-4 and CN-7.

In Figure 2(b) and 3(b), it is seen that a heat treatment at 1h/1580°C after a 3 day anneal at 1100°C provided a very good dispersion of the Cr-rich phase in the CN-7 alloy by breaking up the Laves-type phase that was networked along the Cr-rich phase [see Fig. 2(a) and 3(a)]. Not much improvement in structures (i.e. Cr-rich phase dispersion) was seen at the four temperatures investigated for the CN-4 alloy.

Scanning electron micrographs of the CN-4 alloy in Figure 3(c) for the 3d/1100°C + 1h/1400°C reveal the location of the fine Cr_2Nb precipitates in the Cr-rich phase which were either dissolved during etching or pulled out during polishing. In Figure 3(d), we see that there are no precipitates in the Cr-rich phase. Figures 3(a) and (b) show SEM micrographs for the CN-7 alloy at

3d/1100°C + 1h/1400°C and 3d/1100°C +1h/1580°C, respectively. Once again, we see the evidence for the presence of Cr_2Nb precipitates within the Cr-rich matrix at the lower temperature anneal (i.e. 1 h at 1400°C).

Hardness

Microhardness results are presented in Table 3 for the CN-4, CN-7, and CN-45 alloys for different annealing conditions. The effects of annealing temperature on hardness is shown in Figure 4(a) for the CN-4 alloy. The change in room temperature hardness with niobium concentration of several CN alloys of different thermomechanical history is shown in Figure4(b). No microcracking was observed at the tips of the microhardness indents as was previously reported for alloys in the as-cast condition [1]. The hardness decreases with decreasing niobium concentration and increasing amount of the soft Cr-rich phase. Previous work by Liu [10] has indicated that the hardness tends to decrease as the coarsening of the fine Cr_2Nb particles within the Cr-rich phase occurs for temperatures ranging from 950°C to 1200°C as shown in Figure 4(a). In the present investigation, the hardness increased slightly for the CN-4 and CN-7 alloys at annealing temperatures of 1550°C and 1580°C. Annealing at 1550°c and 1580°c has the following effects: (a) dissolution of the fine Cr_2Nb precipitates in the Cr-rich phase due to an increase in the solubility limit of Nb in Cr; (b) coarsening of the Laves-type phase from Cr_2Nb particles once present in the Cr-rich phase and break-up of the Laves-type phase, as mentioned previously, and; (c) re-precipitation of extremely fine Cr_2Nb particles in the Cr-rich phase upon cooling from 1580°C. The re-precipitation of the fine Cr_2Nb particles in the Cr-rich phase can occur during cooling from temperatures at or above 1400°C, which can lead to an increase in the hardness as shown in Figure 4(a).

Table 3. Microhardness Values (DPH) for the Cr_2Nb-based Intermetallics

Alloy	1400°C	1500°C	1550°C	1580°C
CN-7	367±2	393±12	424±9	406±5
CN-4	465±25	494±12	502±20	513±33
CN-45	616±31	618±26	618±17	613±26

FUTURE WORK

Due to the slow kinetics involved in dispersing the Cr-rich phase, annealing treatments at 1580°C for longer time periods (2 to 3 days) will be performed on these alloys in order to achieve a better dispersion of the Cr-rich phase and/or break-up of the brittle Laves phase. Following the annealing

treatments at 1580°C, a second-stage annealing treatment will be performed at 1200°C for 2 days in order to further precipitate the Cr_2Nb particles in the Cr-rich phase and coarsen them, thus reducing the hardness. Following annealing treatments, compression testing of these alloys will be performed in order to correlate the effect of microstructural change with the ductility of the material. Other future work will include fracture and fatigue testing of these alloys under different conditions, correlation of fracture and fatigue mechanisms with microstructural evaluations, and theoretical modeling of these results.

ACKNOWLEDGEMENTS

The authors wish to give their thanks to Nancy Cole for support of this program. Thanks are due to D.H. Pierce, C.A. Carmichael, and M. Williams for technical assistance. This work is sponsored by the Fossil Energy AR & TD Materials Program, U.S. Department of Energy, under subcontract 11X-SP173V to the University of Tennessee with Martin Marietta Energy Systems, Inc.

REFERENCES

1. M. Takeyama and C.T. Liu, *Materials Science and Engineering*, A132, (1991), pp. 61-66.

2. C.S. Barrett and T.B. Massalski, *Structure of Metals*, McGraw-Hill, New York, 1966, 3rd edn.

3. F. Laves, in *Theory of Alloy Phases*, American Society for Metals, Metals Park, OH, 1956, p. 124.

4. R.P. Messmer, R.C. Tatar and C.L. Briant, in J.L. Walter, M.R. Jackson and C.T. Sims (eds.), *Alloying*, American Society for Metals, Metals Park, OH, 1988, p. 29.

5. P. Villars and L.D. Calvert (eds.), *Pearson's Handbook of Crystallographic Data for Intermetallic Phases*, American Society for Metals, Metals Park, OH, 1985.

6. H.J. Goldschmidt and J.A. Brand, *J. Less-Common Met.*, 3 (1961) 44.

7. T.B. Massalski, J.L. Murray, L.H. Bennett and H. Baker (eds.), *Binary Alloy Phase Diagram*, American Society for Metals, Metals Park, OH, 1986.

8. A.I. Taub and R.L. Fleischer, *Science*, 243 (1989) 616.

9. J.D. Livingston, *Phys. Stat. Sol.* (a)131, 415 (1992).

10. C.T. Liu, pp. 375-383 in *Proc. 6th Annual Conf. on Fossil Energy Materials*, ORNL/FMP-9211, Oak Ridge National Laboratory, July 1992.

11. C.T. Liu, J.A. Horton and C.A. Carmichael, pp. 297-307 in *Proc. 7h Annual Conf. on Fossil Energy Materials*, ORNL/FMP-9211, Oak Ridge National Laboratory, July 1993.

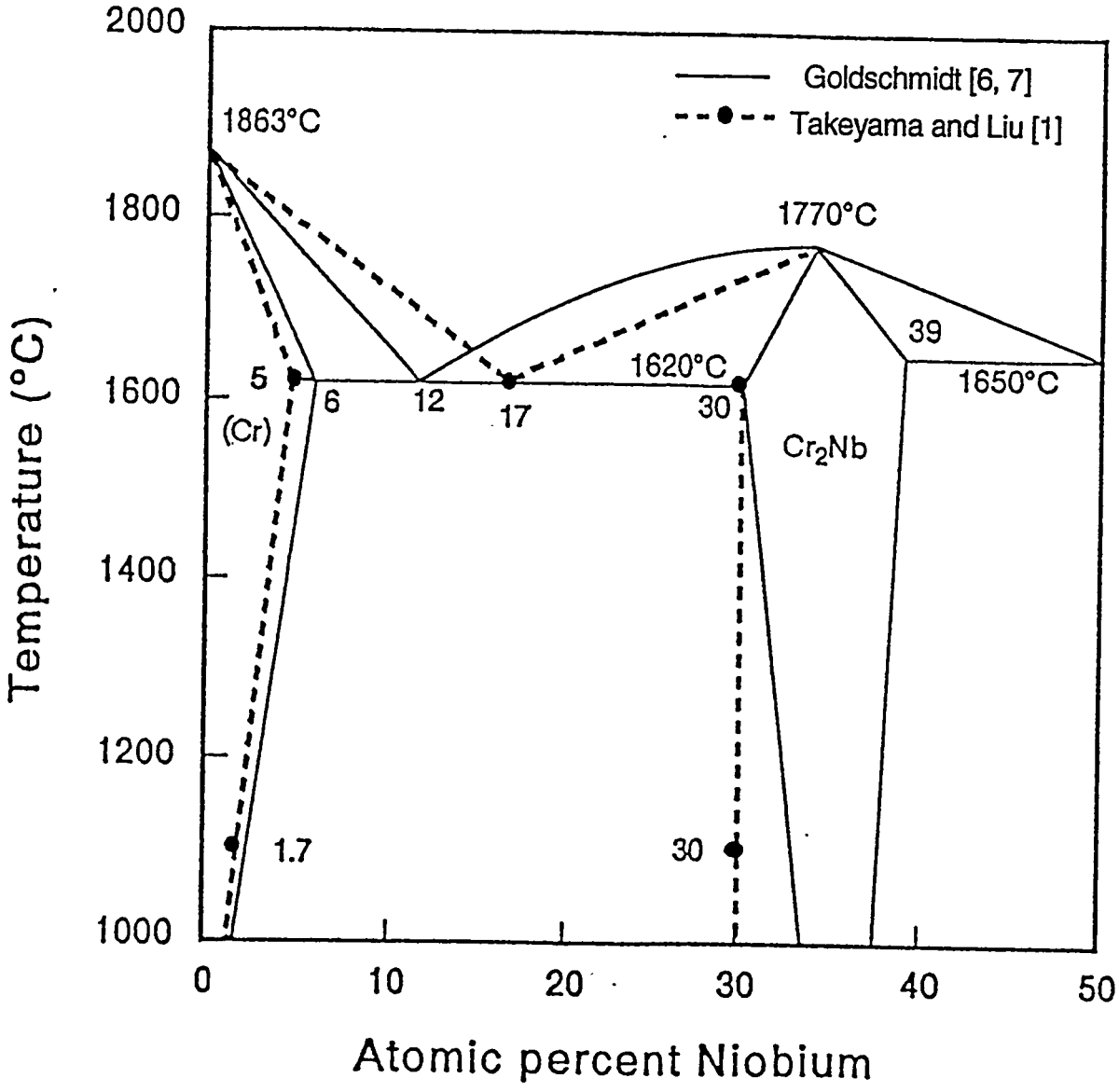

Figure 1. Modified chromium-rich side of the Cr-Nb binary phase diagram from the study of Takeyama and Liu (1), indicating two major differences: (1) the eutectic composition was 17 at.% Nb, instead of 12 at.% Nb; (2) the phase boundary between Cr + Cr_2Nb and CrNb was located at about 30 at.% Nb regardless of temperatures above 1000°C.

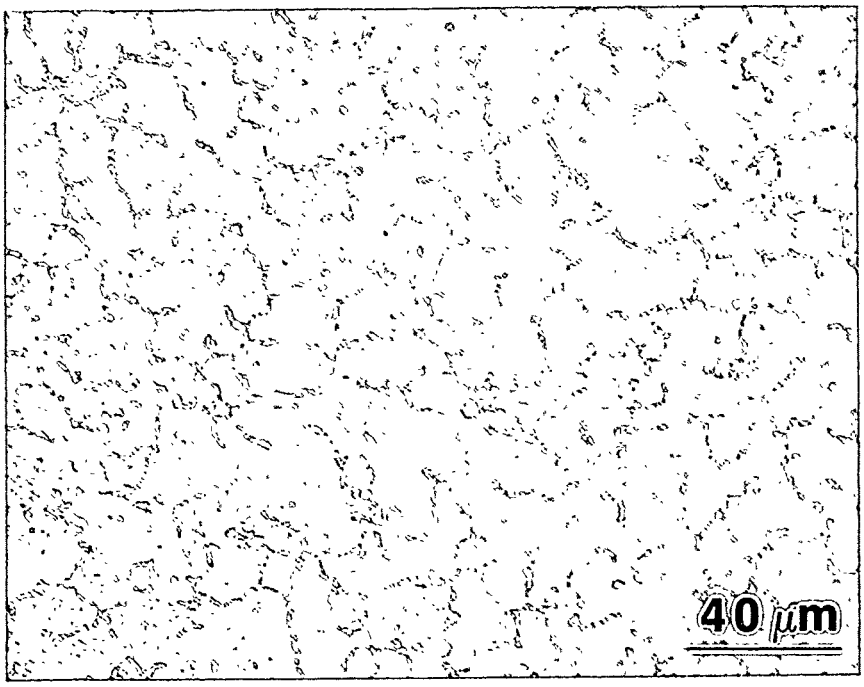

Figure 2(a). Optical micrograph of CN-7 showing chromium-rich patches (light patches) which cover most areas, and a small amount of the Laves-type phase seen as a network along the Cr-rich patches for an anneal of 3 d at 1100°C + 1 h at 1400°C.

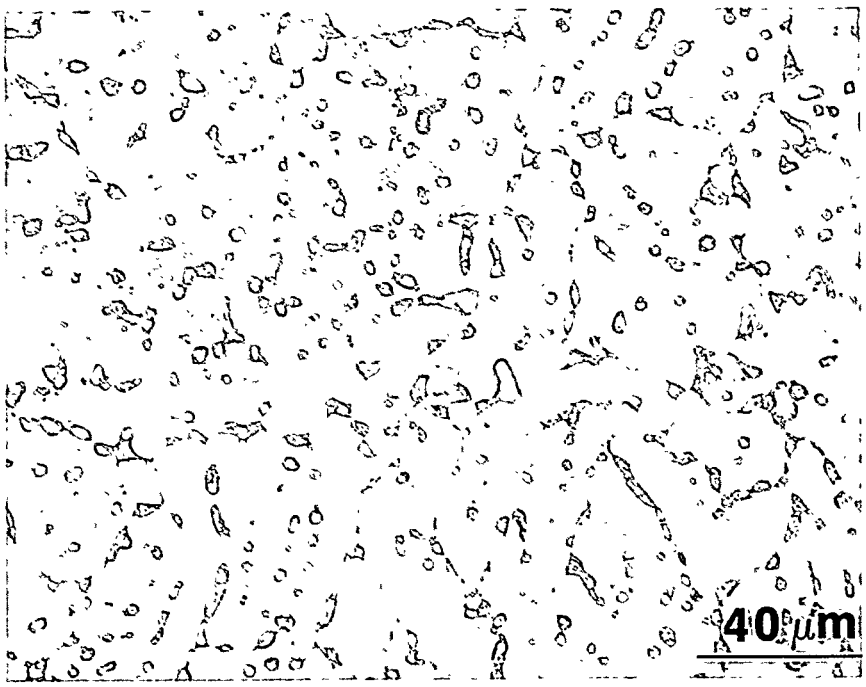

Figure 2(b). Optical micrograph of CN-7 showing chromium-rich patches (light patches) which cover most areas, and a small amount of the Laves-type phase that has been broken up (i.e. dispersed) from the lower temperature anneal. Sample was annealed for 3 d at 1100°C + 1 h at 1580°C.

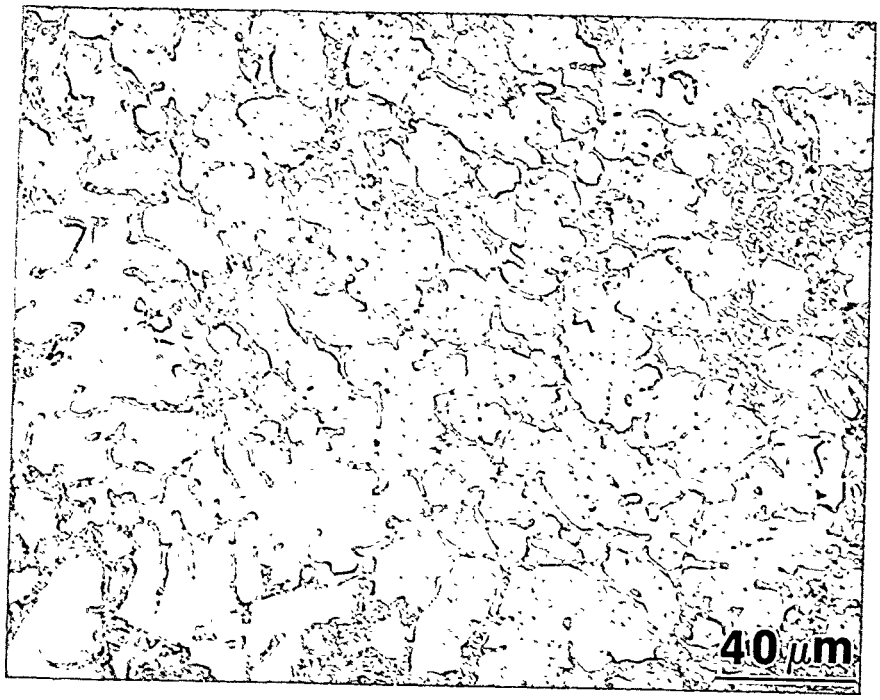

Figure 2(c). Optical micrograph of CN-4 showing chromium-rich patches (light patches) surrounded by the Laves-type phase (Cr_2Nb) for an anneal of 3 d at 1100°C + 1 h at 1400°C.

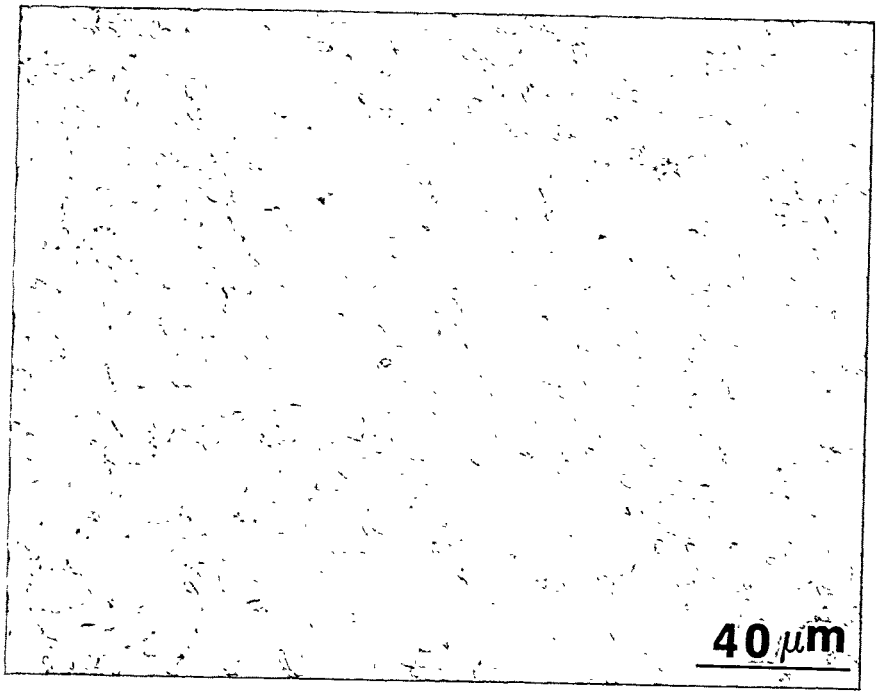

Figure 2(d). Optical micrograph of CN-4 showing chromium-rich patches (light patches) surrounded by the Laves-type phase (Cr_2Nb) for an anneal of 3 d at 1100°C + 1 h at 1580°C.

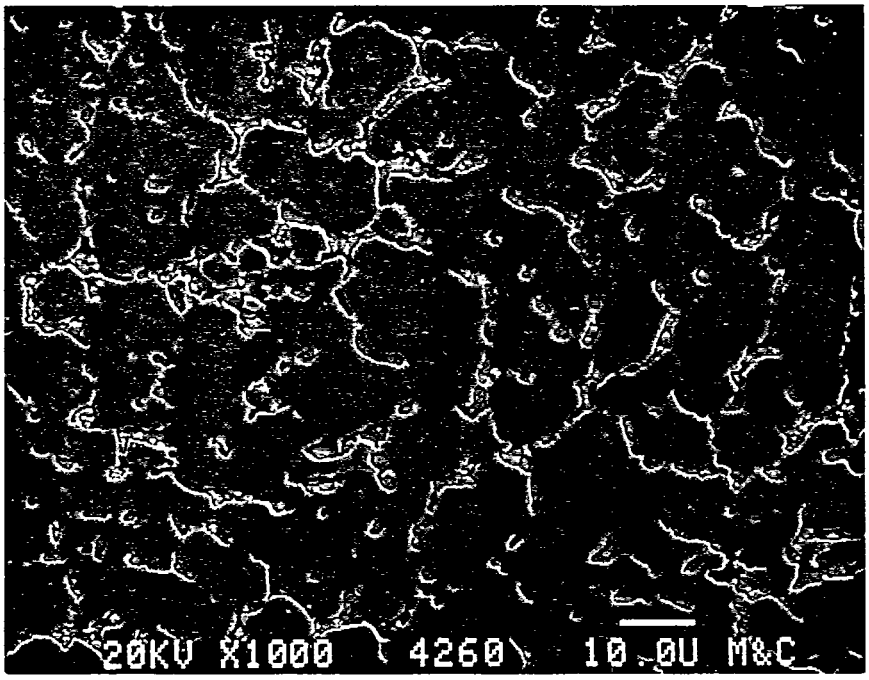

Figure 3(a). SEM micrograph of CN-7 showing chromium-rich patches (light patches) which cover most areas, and a small amount of the Laves-type phase seen as a network along the Cr-rich patches for an anneal of 3 d at 1100°C + 1 h at 1400°C.

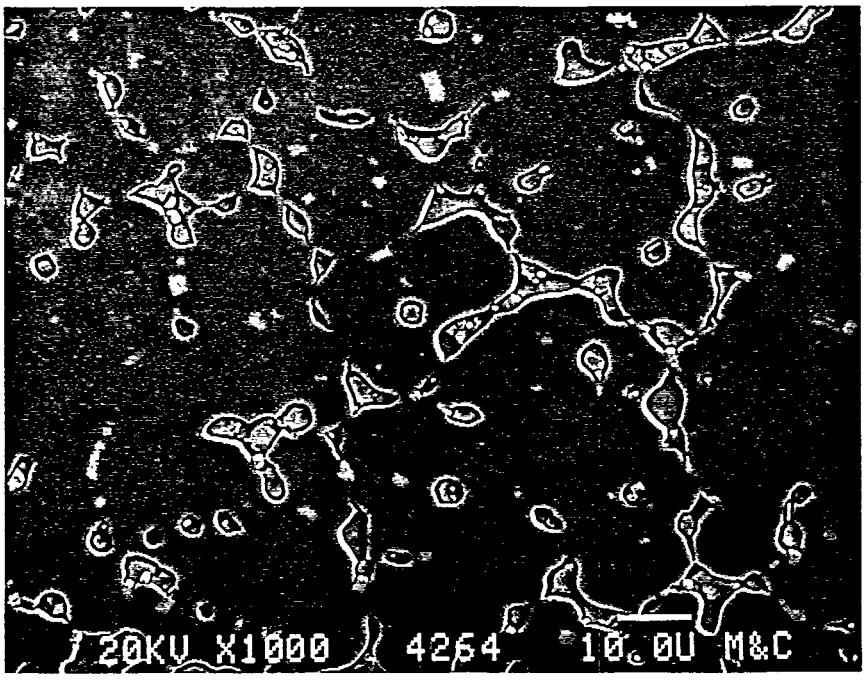

Figure 3(b). SEM micrograph of CN-7 showing chromium-rich patches (light patches) which cover most areas, and a small amount of the Laves-type phase that has been broken up (i.e. dispersed) from the lower temperature anneal. Sample was annealed for 3 d at 1100°C + 1 h at 1580°C.

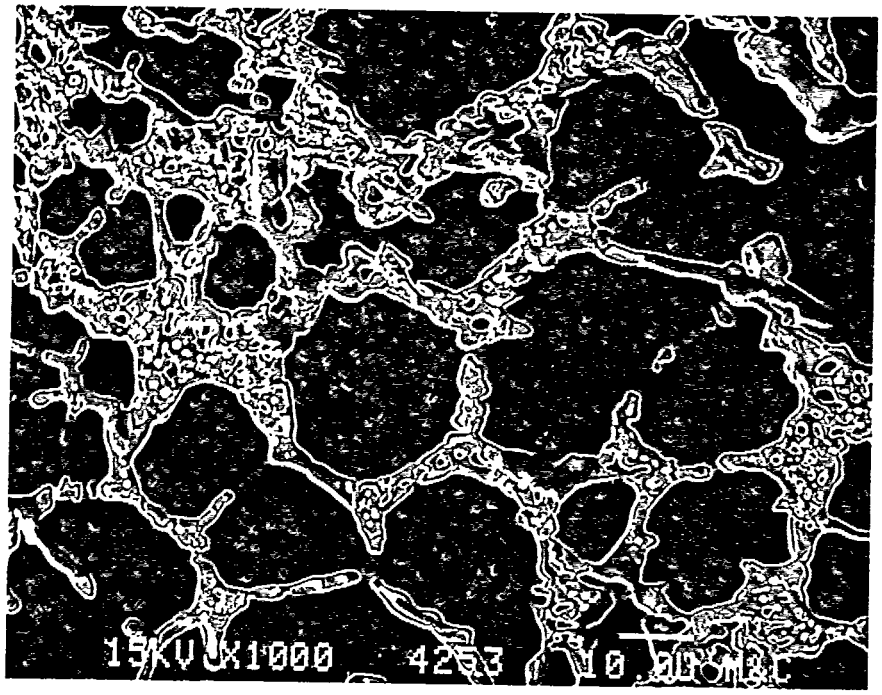

Figure 3(c). SEM micrograph of CN-4 showing chromium-rich patches (light patches) surrounded by the Laves-type phase (Cr_2Nb) for an anneal of 3 d at 1100°C + 1 h at 1400°C.

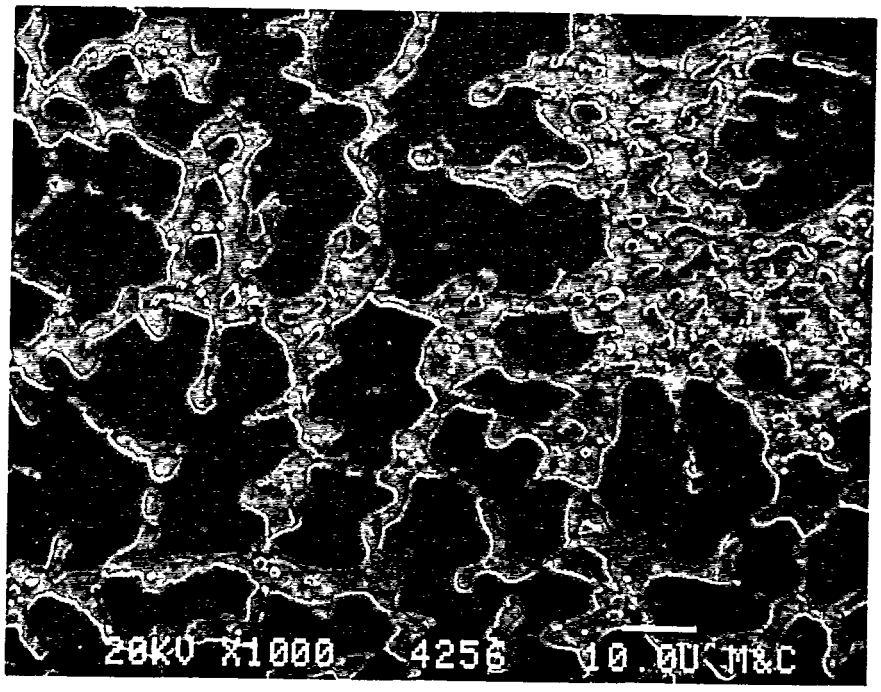

Figure 3(d). SEM micrograph of CN-4 showing chromium-rich patches (light patches) surrounded by the Laves-type phase (Cr_2Nb) for an anneal of 3 d at 1100°C + 1 h at 1580°C.

Figure 4(a). Hardness vs. Annealing Temperature for CN-4

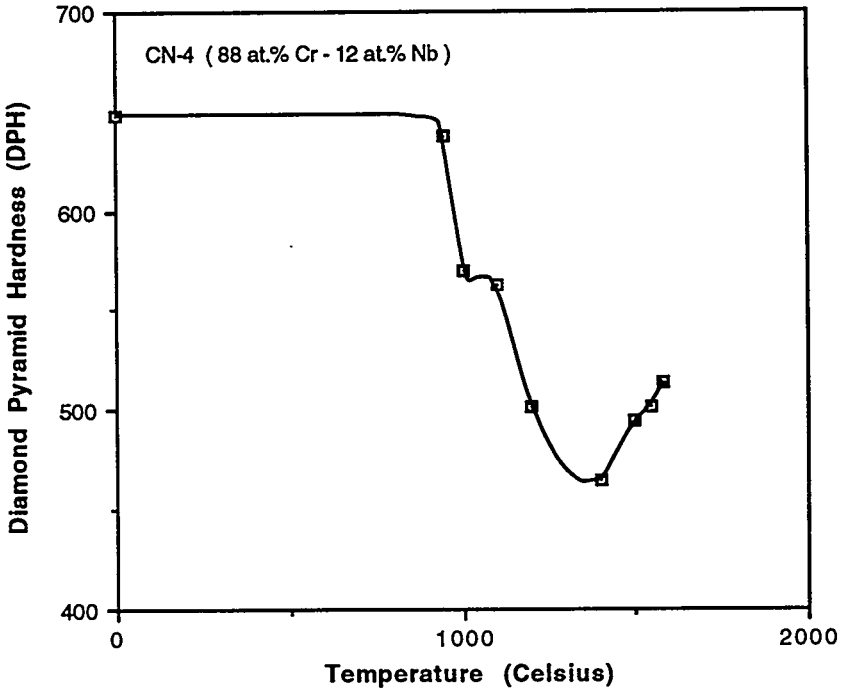

Figure 4(b). Hardness vs. Niobium Concentration (at.%)

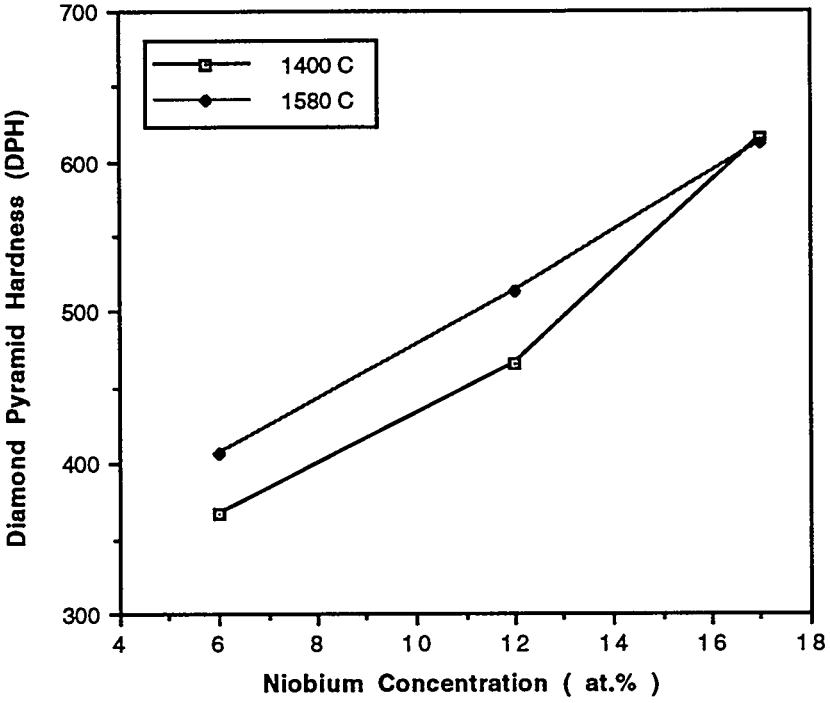

APPENDIX A

FINAL PROGRAM
FOR THE EIGHTH ANNUAL
CONFERENCE ON FOSSIL ENERGY MATERIALS

FINAL PROGRAM
EIGHTH ANNUAL CONFERENCE ON FOSSIL ENERGY MATERIALS

Tuesday, May 10, 1994

SESSION I - CERAMICS
R. R. Judkins, Chairperson

7:00 Registration Desk Opens

8:00 Welcome and Introductory Remarks

8:10 Keynote Address - Marvin Singer DOE/Fossil Energy, Deputy Assistant Secretary for Advanced Research and Special Technologies

8:40 AR&TD Materials Program Overview; James P. Carr, DOE/HQ Program Manager

Session IA - Structural Ceramics

9:10 *Fabrication of Fiber-Reinforced Composites by Chemical Vapor Infiltration*, D. P. Stinton, Oak Ridge National Laboratory

9:40 *Transport Properties of Ceramic Composites*, T. L. Starr, Georgia Tech Research Institute

10:10 *Investigation of Properties and Performance of Ceramic Composite Components*, K. L. Reifsnider, Virginia Polytechnic Institute and State University

10:40 **BREAK**

11:00 *Development of Nondestructive Evaluation Methods and Prediction of Effects of Flaws on the Fracture Behavior of Structural Ceramics*, W. A. Ellingson, Argonne National Laboratory

11:30 *Engineering-Scale Development of the Vapor-Liquid-Solid (VLS) Process for the Production of Silicon Carbide Fibrils*, W. E. Hollar, The Carborundum Company

12:00 **LUNCH**

Session IB - Functional Ceramics

1:20 *Hyrdrogen Production Using Inorganic Membranes*, D. E. Fain, Oak Ridge K-25 Site

1:50 *Carbon Fiber Composite Molecular Sieves*, T. D. Burchell, Oak Ridge National Laboratory

2:20 *Advanced Materials, Electrochemical Studies, and Electrochemical Catalysis Studies for Solid Oxide Fuel Cells*, L. R. Pederson, Pacific Northwest Laboratory

2:50 **BREAK**

3:10 *Testing of Full Size Fiber Reinforced Hot-Gas Filters Fabricated by Chemical Vapor Deposition*, R. G. Smith, 3M Company

3:40 *Advanced Electrolytes and Synthesis of Advanced Catalysts and Membrane Materials*, L. R. Pederson, Pacific Northwest Laboratory

4:10 **ADJOURN**

FINAL PROGRAM

Tuesday May 10, 1994

6:30 - 8:30 p.m.

SESSION II - CERAMICS AND NEW ALLOYS

POSTER PRESENTATIONS - BUFFET RECEPTION

Modeling of Fibrous Preforms for CVI Fabrication, T. L. Starr, Georgia Institute of Technology

Development of Oxidation-Resistant Interface Coatings, D. P. Stinton, Oak Ridge National Laboratory

Joining of SiC Ceramics and SiC/SiC Composites, B. H. Rabin, Idaho National Engineering Laboratory

Densification of Nanosize Powders, S. G. Malghan, National Institute of Standards and Technology

Activation and Micropore Structure Determination of Carbon-Fiber Composite Molecular Sieves, F. Derbyshire, University of Kentucky

Ceramic Catalyst Materials, A. G. Sault, Sandia National Laboratories

Advanced Ceramic Materials and Electrochemical Processes at Interfaces, L. R. Pederson, Pacific Northwest Laboratory

Microwave Assisted Chemical Vapor Deposition, M. A. Janney, Oak Ridge National Laboratory

Effect of Heat Treatment Temperature on Creep-Rupture Properties of Fe_3Al-Based Alloys, C. G. McKamey, Oak Ridge National Laboratory

In-Situ Fireside Corrosion Testing, J. L. Blough, Foster Wheeler Development Corporation

Tensile Properties of As-Cast Fe_3Al-Based Alloys, S. Viswanathan, Oak Ridge National Laboratory

Weldability of Iron Aluminides, G. M. Goodwin, Oak Ridge National Laboratory

Weldability of Polycrystalline Aluminides, G. R. Edwards, Colorado School of Mines

Electro-Spark Deposited Coatings for Fossil Energy Environments, R. N. Johnson, Westinghouse Hanford Company

High-Temperature Corrosion of Iron Aluminides, K. Natesan, Argonne National Laboratory

Elastic Behavior of Nickel Aluminide and Iron Aluminide-Based Intermetallics, M. N. Srinivasan, Texas A&M University

FINAL PROGRAM

Wednesday, May 11, 1994

SESSION III — WORKSHOP ON NEW MATERIALS DEVELOPMENT AND APPLICATIONS
R. R. Judkins, Chairperson

8:00 - 9:30 a.m.

Plenary Session — *Materials Needs in Advanced Fossil Systems*

David J. Beecy — Department of Energy, Office of Fossil Energy

John Mundy — Department of Energy, Basic Energy Sciences

John Stringer — Electric Power Research Institute

Cliff Smith — Department of Energy, Pittsburgh Energy Technology Center

Richard Dennis — Department of Energy, Morgantown Energy Technology Center

Workshop Sessions
9:30 - 12:00 and 1:00 - 2:45 p.m.

Group 1 — Alloys for Advanced Fossil Energy Systems (Combustion 2000; Externally Fired Combined Cycle; Low Emission Boiler System; Hot Particulate Cleanup Systems)

Rapporteurs: Robert W. Swindeman, Oak Ridge National Laboratory and Carl Lundin, University of Tennessee

Group 2 — Ceramic Composites for High Temperature Heat Exchangers, Air Heaters, and Hot Gas Particulate Filters

Rapporteurs: David P. Stinton, Oak Ridge National Laboratory and Mary A. Alvin, Westinghouse Science and Technology Center

Group 3 — Iron Aluminide Development for Coal Combustion, Coal Gasification, and Hot Particulate Cleanup

Rapporteurs: Vinod K. Sikka, Oak Ridge National Laboratory and David Wasyluk, Babcock and Wilcox

Group 4 — Functional Materials for Fuel Cells, Gas Separations, and Catalysts

Group 4A — Fuel Cell Materials Development

Rapporteurs: Larry R. Pederson and Timothy Armstrong, Pacific Northwest Laboratory

Group 4B — Gas Separations Materials

Rapporteurs: Michael S. Hiese, Amoco Corporation, and Timothy D. Burchell, Oak Ridge National Laboratory

Group 4C — Catalyst Materials

Rapporteur: Allen G. Sault, Sandia National Laboratories

3:00 - 4:30 PM

Plenary Session

3:00 PM — Group 1 Report

3:15 PM — Group 2 Report

3:30 PM — Group 3 Report

3:45 PM — Group 4A Report

4:00 PM — Group 4B Report

4:15 PM — Group 4C Report

4:30 PM — Adjourn

FINAL PROGRAM

Thursday, May 12, 1994

SESSION IV - INTERMETALLICS AND ADVANCED AUSTENITICS
N. C. Cole, Chairperson

7:30 Registration Desk Opens

8.00 Welcome and Introductory Remarks

8:10 *Low-Aluminum Content Iron-Aluminum Alloys*, V. K. Sikka, Oak Ridge National Laboratory

8:40 *The Influence of Processing on Microstructure and Properties of Iron Aluminides*, R. N. Wright, Idaho National Engineering Laboratory

9:10 *Fracture Behavior of the Alloy Fe8Al FAP-Y*, D. J. Alexander, Oak Ridge National Laboratory

9:40 *Investigation of Moisture-Induced Embrittlement of Iron Aluminides*, N. S. Stoloff, Rensslear Polytechnic Institute

10:10 **BREAK**

10:30 *Environmental Effects on Iron Aluminide*, J. H. DeVan, Oak Ridge National Laboratory

11:00 *Localized Corrosion and Stress Corrosion Cracking Characteristics of Low Aluminum-Content Iron Aluminum Alloys*, R. A. Buchanan, University of Tennessee

11:30 *Interactions Between Creep and Corrosion in Alloy 800*, K. Natesan, Argonne National Laboratory

12:00 **LUNCH**

1:15 *Fundamental Study of Aluminizing and Chromizing Processes*, R. A. Rapp, The Ohio State University

1:45 *Development of a Modified 310 Stainless Steel*, R. W. Swindeman, Oak Ridge National Laboratory

2:15 *Investigation on the Weldability of High Temperature Alloy Tubing Materials*, C. D. Lundin, University of Tennessee

2:45 **BREAK**

3:00 *Cr_2Nb-Based Alloy Development*, C. T. Liu, Oak Ridge National Laboratory

3:30 *Alloying Effects on the High-Temperature Oxidation Resistance of Cr-Cr_2Nb*, P. F. Tortorelli, Oak Ridge National Laboratory

4:00 *Fracture Behavior of Cr_2Nb-Based Intermetallics*, P. K. Liaw, University of Tennessee

4:30 **ADJOURN**

APPENDIX B

LIST OF ATTENDEES

LIST OF ATTENDEES

Eighth Annual Conference on Fossil Energy Materials
May 10-12, 1994
Oak Ridge, Tennessee

David J. Alexander
Oak Ridge National Laboratory
P.O. Box 2008
Oak Ridge, TN 37831-6151
(615) 574-4467

Mary Anne Alvin
Westinghouse Electric Corporation
Science and Technology Center
1310 Beulah Road
Pittsburgh, PA 15235-5098
(412) 256-2066

Don Anson
Battelle
Commercial/Industrial Technology
505 King Avenue
Columbus, OH 43201
(614) 424-5823

George J. Antos
UOP
50 E. Algonquin Road
Des Plaines, IL 60017-5016
(708) 391-3612

Timothy R. Armstrong
Pacific Northwest Laboratory
P.O. Box 999
Richland, WA 99352
(509) 375-3938

Y. W. Bae
Oak Ridge National Laboratory
P.O. Box 2008
MS-6063
Oak Ridge, TN 37831-6063
(615) 574-9070

J. Lambert Bates
Pacific Northwest Laboratory
P.O. Box 999
Richland, WA 99352
(509) 375-2579

Larry L. Baxter
Sandia National Laboratories
7011 East Avenue
P.O. Box 969
Livermore, CA 94551-0969
(510) 294-2862

David J. Beecy
Department of Energy
Office of Advanced Research
FE-72/GTN
Washington, DC 20585
(301) 903-2787

T. M. Besmann
Oak Ridge National Laboratory
P.O. Box 2008
MS-6063
Oak Ridge, TN 37831-6063
(615) 574-6852

James O. Bird
Amercom, Advanced Material Division
Atlantic Research Corporation
8928 Fullbright Avenue,
Chatsworth, CA 91311
(818) 407-4785

Jeff Blough
Foster Wheeler Development Corporation
John Blizard Research Center
12 Peach Tree Hill Road
Livingston, NJ 07039
(201) 535-2355

Yigal D. Blum
SRI International
333 Ravenswood Avenue
Meno Park, CA 94025
(415) 859-4367

Norman S. Bornstein
United Technologies Research Center
Materials Department
411 Silver Lane
East Hartford, CT 06108
(203) 727-7487

William H. Boss
University of Tennessee Space Institute
UTSI-MS3
Goethert Parkway
Tullahoma, TN 73788
(615) 393-7414

R. A. Bradley
Oak Ridge National Laboratory
P.O. Box 2008
4515, MS-6067
Oak Ridge, TN 37931-6067
(615) 574-6094

Kristin Breder
Oak Ridge National Laboratory
P.O. Box 2008
MS-6062
Oak Ridge, TN 37831-6062
(615) 574-5089

Richard A. Brown
Electric Power Research Institute
3412 Hillview Avenue
Palo Alto, CA 94303
(415) 855-2216

R. A. Buchanan
The University of Tennessee
Department of Materials Science
and Engineering
434 Doughtery Engineering Building
Knoxville, TN 37996-2200
(615) 974-4858

Tim Burchell
Oak Ridge National Laboratory
P.O. Box 2008
Oak Ridge, TN 37831-6088
(615) 576-8595

Bill E. Bustamante
Amercom, Advanced Material Division
Atlantic Research Corporation
8928 Fullbright Avenue
Chatsworth, CA 91311
(818) 407-4787

Narasimhan Calamur
Amoco Chemical Company
P.O. Box 3011, D-2
Naperville, IL 60566-7011
(705) 420-4435

Gary A. Carlson
Sandia National Laboratories
Department 6211, MS-0710
P.O. Box 5800
Albuquerque, NM 87114-0710
(505) 844-8116

J. P. Carr
U.S. Department of Energy
Fossil Energy
Office of Advanced Research
FE-72, GTN
Washington, DC 20585
(301) 903-6519

Richard G. Castro
Los Alamos National Laboratory
P.O. Box 1663
MS G720
Los Alamos, NM 87545
(505) 667-5191

Ashok Choudhury
Office of Technology Transfer
Martin Marietta Energy Systems
701 Scarboro Road
MS-8242
Oak Ridge, TN 37831
(615) 574-0393

Nancy C. Cole
Oak Ridge National Laboratory
P.O. Box 2008
4500, MS-6153
Oak Ridge, TN 37831-6084
(615) 574-4824

K. M. Cooley
Oak Ridge National Laboratory
P.O. Box 2008
MS-6063
Oak Ridge, TN 37831-6063
(615) 574-4559

Jean-Francois A. Le Costaouec
Techniweave, Inc.
109 Chestnut Hill Road
Rochester, NH 03868
(603) 335-2115

William Curtin
Virginia Polytechnic Institute & State University
Department of Engineering Science and Mechanics
College of Engineering
Blacksburg, VA 24061-0219
(703) 231-5316

Thomas P. DeAngelis
Director, Ceramic Technology
The Carborundum Company
P.O. Box 832
Niagara Falls, NY 14302-0832
(716) 278-2086

Arthur B. Denison
EG&G Idaho
Idaho National Engineering Laboratory
2151 N. Boulevard
Idaho Falls, ID 83401-2025
(208) 526-1294

Richard A. Dennis
Morgantown Energy Technology Center
880 Collins Ferry Road
Morgantown, WV 26505
(304) 291-4515

Frank Derbyshire
University of Kentucky
Center for Applied Energy Research
3572 Iron Works Pike
Lexington, KY 40511-8433
(606) 257-0305

J. H. DeVan
Oak Ridge National Laboratory
P.O. Box 2008
4500S, MS-6138
Oak Ridge, TN 37831-6138
(615) 574-4451

James R. DiStefano
Oak Ridge National Laboratory
P.O. Box 2008
Oak Ridge, TN 37831-6157
(615) 574-4452

John N. DuPont
Lehigh University
Energy Research Center
5E Packer Avenue
Whitaker Laboratory
Bethlehem, PA 18015
(215) 758-3942

Dewey Easton
Oak Ridge National Laboratory
P.O. Box 2008
Oak Ridge, TN 37831-6117
(615) 574-5158

Joseph H. Eaton
Ceramic Technology Center
3M Company
Bldg 203-1-01
3M Center
St. Paul, MN 55144
(612) 733-8482

G. R. Edwards
Colorado School of Mines
Center for Welding and Joining Research
Golden, CO 80401
(303) 273-3773

William A. Ellingson
Argonne National Laboratory
9700 South Cass Avenue
Argonne, IL 60439
(708) 252-5068

Douglas Fain
Oak Ridge K-25 Site
P.O. Box 2003
1004-L, MS 7271
Oak Ridge, TN 37831-7271
(615) 574-9932

Albert Z. Fresco
Dupont Lanxide Composites, Inc.
1300 Marrows Road
p.O. Box 6077
Newark, DE 19714-6077
(302) 456-6241

Thomas B. Gibbons
ABB Combustion Engineering
Power Plant Laboratories
1000 Prospect Hill Road
Windsor, CT 06095
(203) 285-3593

Philip Goldberg
U. S. Department of Energy
Pittsburgh Energy Technology Center
P.O. Box 10940
Pittsburgh, PA 15236
(412) 892-5806

Rocky Goldstein
Electric Power Research Institute
3412 Hillview Avenue
Palo Alto, CA 94303
(415) 855-2171

G. M. Goodwin
Oak Ridge National Laboratory
P.O. Box 2008
4508, MS-6096
Oak Ridge, TN 37831-6096
(615) 574-4809

Paul Gregson
British National Fuels Limited
804 Kerr Hollow Road
Oak Ridge, TN 37830
(615) 481-0455

Ulrich Grimm
U. S. Department of Energy
Morgantown Energy Technology Center
P.O. Box 880
Morgantown, WV 26505
(304) 291-4378

Lance E. Groseclose
Allison Engine Company
Materials Engineering
P.O. Box 420
Indianapolis, IN 46206-0420
(317) 230-3806

John Hanigofsky
Technology Assessment & Transfer
133 Defense Highway
Suite 212
Annapolis, MD 21401
(410) 224-3710

Tanweer Haq
PALL Corporation
5 E. Packer Avenue
Whitaker Laboratory #5
Bethlehem, PA 18015
(215) 758-3942

Bob Hayes
Manufacturing Sciences Corporation
804 Kerr Hollow Road
Oak Ridge, TN 37830
(615) 481-0455

Clint Haynes
Stress Engineering Services, Inc.
Consumer Products Group
415 Glensprings Drive, Suite 200
Cincinnati, OH 45246
(513) 589-3953

William P. Heckel, Jr.
President
Alon Processing, Inc.
Grantham Street
Tarentum, PA 15084
(412) 226-1677

Steven H. Hildebrandt
Research & Development
Hydrocarbon Research, Inc.
P.O. Box 6047
New York & Puritan Avenue
Lawrenceville, NJ 08648
(609) 394-3102

E. E. Hoffman
U. S. Department of Energy
Oak Ridge Operations
P.O. Box 2008
MS-6269
Oak Ridge, TN 37831
(615) 576-0735

William E. Hollar
The Carborundum Company
P.O. Box 832
Niagara Falls, NY 14302
(716) 278-2097

John E. Holowczak
Advanced Ceramics
United Technologies Research Center
MS 129-22
Silver Lane
East Hartford, CT 06108
(203) 727-1649

Linda Horton
Oak Ridge National Laboratory
P.O. Box 2008
Oak Ridge, TN 37831-6134
(615) 574-5081

Peggy Y. Hou
Lawrence Berkeley Laboratory
Material Science
1 Cyclotron Road
Ms 62-203
Berkeley, CA 94720
(510) 486-5560

Wayne Huebner
University of Missouri-Rolla
Department of Ceramics
222 McNutt Hall
Rolla, MO 65401

John P. Hurley
University of North Dakota
P.O. Box 9018
University Station
Grand Forks, ND 58202
(701) 777-5159

Nate Jacobson
NASA Lewis
MS 106-1
21000 Brookpark Road
Cleveland, OH 44135
(216) 433-5498

Suresh C. Jain
U. S. Department of Energy
FE 231
Washington, DC 20585
(301) 903-0508

Mark Janney
Oak Ridge National Laboratory
P.O. Box 2008
4508, MS-6087
Oak Ridge, TN 37831-6087
(615) 574-4281

R. N. Johnson
Westinghouse Hanford Company
P. O. Box 1970
Richland, WA 99352
(509) 376-3582

Roddie R. Judkins
Oak Ridge National Laboratory
P.O. Box 2008
4508, MS-6084
Oak Ridge, TN 37831-6084
(615) 574-4572

David P. Kalmanovitch
Riley Stoker Corporation
Metallurgical Laboratory
5 Neponset Street
Worcester, MA 01606
(508) 852-7100

James R. Keiser
Oak Ridge National Laboratory
P. O. Box 2008
Bldg. 4500S, MS-6156
Oak Ridge, TN 37831-6156
(615) 574-4453

James C. Kelly
Director of Technology
Rolled Alloys
125 West Sterns Road
P.O. Box 310
Temperance, MI 48182
(313) 847-0561

Robert J. Kerhin
Sargent & Lundy
CMED
55E Monroe Street
Chicago, IL 60603
(312) 269-6212

Ashok Khandkar
Ceramatec, Inc.
1415 S. 900 West
Salt Lake City, UT 84119
(801) 972-2455

Nick Korens
SFA Pacific, Inc
444 Castro Street, Suite 920
Mountain View, CA 94041
(415) 969-8876

George Y. Lai
Haynes International, Inc.
1020 W. Park Avenue
Kokomo, IN 46904
(317) 456-6260

Dennis Landini
Dupont Lanxide Composites
Advanced Composites
1300 Marrows Road
P.O. Box 6077
Newark, DE 19714
(302) 456-6514

Lori Leaskey
MER Corporation
7960 S. Kolb Road
Tucson, AZ 85706
(602) 574-1980

Benson P. Lee
Technology Management Inc.
9718 Lake Shore Blvd.
Cleveland, OH 44108
(216) 541-1000

Woo Y. Lee
Oak Ridge National Laboratory
P.O. Box 2008
MS-6063
Oak Ridge, TN 37831-6063
(615) 576-2894

Mel Leitheiser
3M Company
3M Center (201-4N-01)
St. Paul, MN 55144-1000
(612) 733-9394

Peter Liaw
The University of Tennessee
Department of Materials Science &
Engineering
434 Doughtery Engineering Building
Knoxville, TN 37996-2200
(615) 974-6356

C. T. Liu
Oak Ridge National Laboratory
P.O. Box 2008
Oak Ridge, TN 37831-6156
(615) 574-4459

Carl D. Lundin
The University of Tennessee
Department of Materials Science &
Engineering
434 Dougherty Engineering Building
Knoxville, TN 37996-2200
(615) 974-5310

Ed Ma
Department of Chemical Engineering
Worcester Polytechnic Institute
100 Institute Road
Worcester, MA 01609
(508) 831-5398

Subhaus G. Malghan
National Institute of Standards and Technology
Materials Building 223/A256
Gaithersburg, MD 20899
(301) 975-6101

Scott X. Mao
University of Calgary
Department of Mechanical Engineering
2500 University Dr. NW
Calgary, Canada
(403) 220-7185

Douglas Marriott
Stress Engineering Services, Inc.
Consumer Products Group
415 Glensprings Drive
Suite 200
Cincinnati, OH 45246
(513) 589-3951

W. M. Matlin
Oak Ridge National Laboratory
P.O. Box 2008
MS-6063
Oak Ridge, TN 37831-6063
(615) 574-4559

Claudette McKamey
Oak Ridge National Laboratory
P.O. Box 2008
MS-6114, 4500S
Oak Ridge, TN 37831-6114
(615) 574-6917

Jerry McLaughlin
Oak Ridge National Laboratory
P.O. Box 2008
Bldg. 4515, MS-6063
Oak Ridge, TN 37831-6063
(615) 574-4559

Theodore J. McMahon
U. S. Department of Energy
Morgantown Energy Technology Center
P.O. Box 880
MS CO4
Morgantown, WV 26505
(304) 291-4865

Bob Miller
NASA Lewis
MS 24-1
21000 Brookpark Road
Cleveland, OH 44135
(216) 433-3298

Nguyen Minh
AlliedSignal
2525 W 190th Street
Department 93140, MS T-41
Torrance, CA 90504-6099
(310) 512-3515

Karren More
Oak Ridge National Laboratory
P.O. Box 2008
4515, MS-6064
Oak Ridge, TN 37831-6064
(615) 574-7788

John N. Mundy
U. S. Department of Energy
BES
Division of Material Sciences
ER-131, MSG 236
Washington, DC 20585
(301) 903-4271

Thomas Muth
Manufacturing Sciences Corporation
804 Kerr Hollow Road
Oak Ridge, TN 37830
(615) 481-0455

T. V. Narayanan
Foster Wheeler Development Corporation
John Blizard Research Center
12 Peach Tree Hill Road
Livingston, NJ 07039
(201) 535-2224

K. Natesan
Argonne National Laboratory
9700 South Cass Avenue
Argonne, IL 60439
(708) 252-5103

Juan Carlos Nava-Paz
ABB Power Plant Laboratories
Materials and Water Chemistry
1000 Prospect Hill Road
Windsor, CT 06095
(203) 285-5887

Dick Nixdorf
President
ReMaxCo Technologies, Inc.
1701 Louisville Drive, Suite C
Knoxville, TN 37921
(615) 588-8342

Dennis J. O'Rear
Chevron Research & Technology Company
100 Chevron Way
Richmond, CA 94802-0627
(510) 242-4908

Arvid E. Pasto
Oak Ridge National Laboratory
P.O. Box 2008
Oak Ridge, TN 37831-6085
(615) 574-4956

Charles E. Pax
U. S. Department of Energy
Fossil Energy
FE-73
Washington, DC 20585
(301) 903-2832

L. R. Pederson
Pacific Northwest Laboratory
MS K2/44
P.O. Box 999
Richland, WA 99352
(509) 375-2731

Michael Perlsweig
U.S. Department of Energy
Office of Coal Technology
FE-232, GTN
Washington, DC 20585
(301) 903-4399

Bruce Pint
Oak Ridge National Laboratory
P.O. Box 2008
MS-6157
Oak Ridge, TN 37831-6157
(615) 576-2897

Cong Yue Qiao
The University of Tennessee
Department of Materials Science and Engineering
326 Doughtery Engineering Building
Knoxville, TN 37966-2200
(615) 974-5299

Barry H. Rabin
Idaho National Engineering Laboratory
P.O. Box 1625
Idaho Falls, ID 83415
(208) 526-0058

K. S. Ramesh
Pacific Northwest Laboratory
Materials Research
P.O. Box 999
MSIN K3-59
Richland, WA 99352
(509) 372-4523

R. A. Rapp
Ohio State University
Department of Metallurgical Engineering
116 West 19th Avenue
Columbus, OH 43210
(614) 292-6178

F. Rebillat
Oak Ridge National Laboratory
P.O. Box 2008
MS-6063
Oak Ridge, TN 37831-6063
(615) 574-6852

K. L. Reifsnider
Virginia Polytechnic Institute and
State University
Department of Engineering Science
and Mechanics
College of Engineering
Blacksburg, VA 24061-0219
(703) 231-5259

Jeffery H. Richardson
Chemistry and Materials Science
Lawrence Livermore National Laboratory
P.O. Box 808, L-353
Livermore, CA 94551
(510) 423-5187

George Roettger
Oak Ridge K-25 Site
P.O. Box 2003
1004-L, MS-7271
Oak Ridge, TN 37831-7271
(615) 574-7539

George Samara
Sandia National Laboratories
Department 6211
P.O. Box 5800
Albuquerque, NM 87185

Jag Sankar
North Carolina A&T State University
Department of Mechanical Engineering
#622 McNair Building
Greensboro, NC 27411
(910) 334-7620

Vinod K. Sarin
Boston University
44 Washington Street
Boston, MA 02215
(615) 353-6451

Allen G. Sault
Sandia National Laboratories
Department 6211
P.O. Box 5800
Albuquerque, NM 87185
(505) 844-8723

Dan Scarpiello
GRI
8600 W. Bryn Mawr
Chicago, IL 60656
(312) 399-8332

O. J. Schwarz
Oak Ridge National Laboratory
P.O. Box 2008
MS-6063
Oak Ridge, TN 37831-6063
(615) 576-2896

S. Shanmugham
Oak Ridge National Laboratory
P.O. Box 2008
MS-6063
Oak Ridge, TN 37831-6063
(615) 574-4559

Vinod Sikka
Oak Ridge National Laboratory
P.O. Box 2008
4508, MS-6083
Oak Ridge, TN 37831-6083
(615) 574-5112

Marvin I. Singer
U. S. Department of Energy
Fossil Energy
FE 70,
4G-052/FORS
Washington, DC 20585
(202) 586-1577

J. P. Singh
Argonne National Laboratory
Bldg. 212
9700 South Cass Avenue
Argonne, IL 60439

Subhash Singhal
Westinghouse Electric Corporation
Science & Technology Center
1310 Beulah Road
Pittsburgh, PA 15235
(412) 256-1208

Philip Sklad
Oak Ridge National Laboratory
P.O. Box 2008
Oak Ridge, TN 37831-6065
(615) 574-5069

David G. Sloat
Sargent & Lundy
55 E. Monroe Street
Chicago, IL 60603-5780
(312) 269-2784

Cliff Smith
U. S. Department of Energy
Pittsburgh Energy Technology Center
P.O. Box 10940
Pittsburgh, PA 15236
(412) 892-4518

Robert G. Smith
3M Company
Bldg. 203-1-01
3M Center
St. Paul, MN 55144-1000
(612) 733-2564

John E. Smugeresky
Sandia National Laboratories
7011 East Avenue
P.O. Box 969, MS 9402
Livermore, CA 94551-0969
(510) 294-2910

Stuart Soled
Exxon
Rt. 22 East
Annondale, NJ 08801
(908) 730-2577

Daniel J. Sordelet
Iowa State University
Ames Laboratory
107 Metals Development
Ames, IA
(515) 294-4713

Charles A. Sorrell
U.S. Department of Energy
Industrial Technologies
EE-232
1000 Independence Avenue, SW
Washington, DC 20585
(202) 586-1514

Malur N. Srinivasan
Texas A&M University
Engineering/Physics Building
College Station, TX 77843-3123
(409) 845-1417

Thomas L. Starr
Georgia Institute of Technology
GTRI/MSTL
925 Dalney Street
Atlanta, GA 30332
(404) 853-0579

H. Stuart Starrett
Director, Mechanics Research
Southern Research Institute
2000 Ninth Avenue South
Birmingham, AL 35205
(205) 581-2452

David P. Stinton
Oak Ridge National Laboratory
P.O. Box 2008
4515, MS-6063
Oak Ridge, TN 37831-6063
(615) 574-4556

N. S. Stoloff
Rensselaer Polytechnic Institute
Materials Engineering Department
Troy, NY 12180-3590
(518) 276-6371

Tom Strangman
Allied Signal Engines
MS 553-12
11 S. 34th Street
Phoenix, AZ 85071-2181
(602) 231-4147

John Stringer
Electric Power Research Institute
3412 Hillview Avenue
Palo Alto, CA 94303
(415) 855-2472

Robert W. Swindeman
Oak Ridge National Laboratory
P.O. Box 2008
MS-6155, 4500S
Oak Ridge, TN 37831-6155
(615) 574-5108

V. J. Tennery
Oak Ridge National Laboratory
P.O. Box 2008
MS-6062
Oak Ridge, TN 37831-6062
(615) 574-5123

Terry Tiegs
Oak Ridge National Laboratory
P.O. Box 2008
4515, MS-6087
Oak Ridge, TN 37831-6087
(615) 574-5173

Peter F. Tortorelli
Oak Ridge National Laboratory
P.O. Box 2008
Oak Ridge, TN 37831-6156
(615) 574-5119

Richard Tressler
Department of Materials Science and Engineering
Pennsylvania State University
101 Steidle Building
University Park, PA 16802
(814) 865-0497

Carl F. VanConant
Third Millennium Technology, Inc.
120 Sherlake Drive
P.O. Box 23556
Knoxville, TN 37933-1556
(615) 691-2170

Steven Visco
Materials Science Division
Lawrence Berkeley Laboratory
Berkeley, CA 94720
(510) 486-5821

Srinath Viswanathan
Oak Ridge National Laboratory
P.O. Box 2008
4508, MS-6083
Oak Ridge, TN 37831-6083
(615) 576-9917

Dave Wasyluk
Babcock & Wilcox
20 South Van Buren Avenue
Barberton, OH 44203
(216) 860-1132

Philip S. Way
Permeable Ceramics
Ferro Corporation
603 West Commercial St.
E. Rochester, NY 14445
(716) 586-8770

Bill L. Weaver
Ceramic Technology Center
3M Company
Bldg 203-1-01
3M Center
St. Paul, MN 55144
(612) 736-9655

James K. Weddell
Dupont Lanxide Composites, Inc.
Pencader Plant
P.O. Box 6100
Newark, DE 19714-6100
(302) 733-8008

James K. Wessel
Director
Federal Business Development
Dow Corning Corporation
1800 M Street, NW
#325 South
Washington, DC 20036
(202) 785-0585

Glenn White
Business Manager
Dupont Lanxide Composites
1300 Mallows Road
P.O. Box 6077
Newark, DE 19714
(302) 456-6481

Dane Wilson
Oak Ridge National Laboratory
P.O. Box 2008
MS-6156
Oak Ridge, TN 37831-6156
(615) 586-4810

Ian Wright
Electric Power Research Institute
3412 Hillview Avenue
Palo Alto, CA 94034
(415) 855-2363

Richard N. Wright
EG&G
Idaho National Engineering Laboratory
P.O. Box 1625
Idaho Falls, ID 83415-2218
(208) 526-6127

William H. Zielke
CE Tubes
500 West 26th Street
Chattanooga, TN 37408
(615) 752-7008

CONF-9405145
ORNL/FMP-94/1

INTERNAL DISTRIBUTION

1. D. J. Alexander
2. P. Angelini
3. Y. W. Bae
4. R. H. Baldwin
5. R. L. Beatty
6. T. M. Besmann
7. A. Bleier
8. R. A. Bradley
9. K. Breder
10. T. D. Burchell
11. P. T. Carlson
12-16. N. C. Cole
17. K. M. Cooley
18. J. H. DeVan
19. J. R. DiStefano
20. D. S. Easton
21. B. Z. Egan
22. D. E. Fain
23. W. Fulkerson
24. E. L. Fuller
25. G. M. Goodwin
26. J. D. Griffin
27. L. L. Horton
28. M. A. Janney
29-30. R. R. Judkins
31. M. A. Karnitz
32. J. R. Keiser
33. W. Y. Lee
34. C. T. Liu
35. W. M. Matlin
36. D. J. McGuire
37. C. G. McKamey
38. J. C. McLaughlin
39. K. L. More
40. A. Pasto
41. B. Pint
42. W. D. Porter
43. F. Rabillat
44. G. E. Roettger
45. A. C. Schaffhauser
46. J. H. Schneibel
47. O. J. Schwarz
48. S. Shanmugham
49. V. K. Sikka
50. P. S. Sklad
51. D. P. Stinton
52. R. W. Swindeman
53. V. J. Tennery
54. T. N. Tiegs
55. P. F. Tortorelli
56. S. Viswanathan
57. D. F. Wilson
58-59. Central Research Library
60. Document Reference Section
61. ORNL Patent Section
62-63. Laboratory Records Department
64. Metals and Ceramics Records Office
65. LRD-RC

EXTERNAL DISTRIBUTION

66-69. 3M COMPANY, 3M Center, St. Paul, MN 55144
J. H. Eaton (Bldg 203-1-01)
M. L. Leitheiser
R. G. Smith (Bldg 203-1-01)
B. L. Weaver (Bldg 203-1-01)

70. ABB Lummus Crest, 15 Broad St., Bloomfield, NJ 07003
M. Greene

71. ABB COMBUSTION ENGINEERING, 911 W. Main St., Chattanooga, TN 37402
D. A. Canonico

72-73. ABB COMBUSTION ENGINEERING, 1000 Prospect Hill Road, Windsor, CT 06095
T. B. Gibbons
J. C. Nava

74. ADIABATICS, INC., 3385 Commerce Dr., Columbus, IN 47201
P. Badgley

75. ADVANCED REFRACTORY TECHNOLOGIES, INC., 699 Hertel Avenue, Buffalo, NY 14207
K. A. Blakely

76-77. AEA INDUSTRIAL TECHNOLOGY, Harwell Laboratory, Materials Development Division, Bldg. 393, Didcot, Oxfordshire, OX110RA ENGLAND
M. Bennett
H. Bishop

78. AIR PRODUCTS AND CHEMICALS, INC., 7201 Hamilton Blvd., Allentown, PA 18195-1501
P. Dyer

79. ALBERTA RESEARCH COUNCIL, Oil Sands Research Department, P. O. Box 8330, Postal Station F, Edmonton, Alberta, CANADA T6H5X2
L. G. S. Gray

80. ALLEGHENY LUDLUM STEEL, Technical Center, Alabama and Pacific Avenues, Brackenridge, PA 15014
J. M. Larsen

81. ALLIEDSIGNAL, 2525 W 190th Street, Dept. 93140, Torrance, CA 90504-6099
N Minh (MS T-41)

82. ALLIEDSIGNAL ENGINES, 111 S. 34th Street,
Phoenix, AZ 85071-2181
T. Strangman (MS 553-12)

83. ALLISON ENGINE COMPANY, Materials Engineering, P.O. Box 420,
Indianapolis, IN 46206-0420
L. E. Groseclose

84-86. ALLISON GAS TURBINE DIVISION, P. O. Box 420, Indianapolis, IN 46206-0420
P. Khandalwal (Speed Code W-5)
R. A. Wenglarz (Speed Code W-16)
J. R. Whetstone

87. ALON PROCESSING, INC., Grantham Street, Tarentum, PA 15084
W. P. Heckel, Jr.

88. AMAX R&D CENTER, 5950 McIntyre St., Golden, CO 80403
T. B. Cox

89-90. AMERCOM, Advanced Material Division, Atlantic Research Corporation
8928 Fullbright Avenue, Chatsworth, CA 91311
J. O. Bird
W. E. Bustamante

91. AMOCO CHEMICAL COMPANY, P. O. Box 3011, D-2,
Naperville, IL 60566-7011
N. Calamur

92. A. P. GREEN REFRACTORIES COMPANY, Green Blvd.,
Mexico, MO 65265
J. L. Hill

93-95. ARGONNE NATIONAL LABORATORY, 9700 Cass Ave.,
Argonne, IL 60439
W. A. Ellingson
K. Natesan
J. P. Singh

96. ARMY MATERIALS TECHNOLOGY LABORATORY SLCMT-MCC,
Watertown, MA 02172-0001
D. R. Messier

97. AVCO RESEARCH LABORATORY, 2385 Revere Beach Parkway,
Everett, MA 02149
R. J. Pollina

98. BABCOCK & WILCOX, 1562 Beeson St., Alliance, OH 44601-2196
W. R. Mohn

99-100. BABCOCK & WILCOX, Domestic Fossil Operations,
20 South Van Buren Ave., Barberton, OH 44023
M. Gold
D. Wasyluk

101-104. BABCOCK & WILCOX, Lynchburg Research Center, P. O. Box 11165,
Lynchburg, VA 24506
R. Goettler
J. A. Heaney
W. Long
H. H. Moeller

105. BATTELLE COLUMBUS LABORATORIES, 505 King Ave.,
Columbus, OH 43201
D. Anson

106-107. BETHLEHEM STEEL CORPORATION, Homer Research Laboratories,
Bethlehem, PA 18016
B. L. Bramfitt
J. M. Chilton

108. BOSTON UNIVERSITY, 44 Washington Street, Boston, MA 02215
V. K. Sarin

109-111. BRITISH COAL CORPORATION, Coal Research Establishment,
Stoke Orchard, Cheltenham, Glocester, ENGLAND GL52 4RZ
J. Oakey
M. A. Smith
I. Summerfield

112-113. CANADA CENTER FOR MINERAL & ENERGY TECHNOLOGY,
568 Booth St., Ottawa, Ontario Canada K1A OG1
R. W. Revie
M. Sahoo

114. CATERPILLAR INC., Technology Center, P.O. Box 1875,
Perioria, IL 61656-1875
D. I. Biehler

115. CE TUBES, 500 West 26th Street, Chattanooga, TN 37408
W. H. Zielke

116. CERAMATEC, INC., 1415 S. 900 West, Salt Lake City, UT 84119
A. Khandkar

117. CHEVRON RESEARCH & TECHNOLOGY COMPANY, 100 Chevron Way,
Richmond, CA 94802-0627
D. J. O'Rear

118. CIEMAT, Avda. Complutense, 22, 28040-Madrid (SPAIN)
G. M. Calvo

119. COAL & SYNFUELS TECHNOLOGY, 1401 Wilson Blvd., Suite 900, Arlington, VA 22209
E. Tilley-Hinkle

120. COAL & SYNFUELS TECHNOLOGY, 1616 N. Fort Myer Dr., Suite 1000, Arlington, VA 22209
J. Bourbin

121-122. COAL TECHNOLOGY CORPORATION, 103 Thomas Road, Bristol, VA 24201
R. A. Wolfe
R. E. Wright

123. COLORADO SCHOOL OF MINES, Dept. of Metallurgical Engineering, Golden, CO 80401
G. R. Edwards

124-126. CONSOLIDATION COAL COMPANY, 4000 Brownsville Road, Library, PA 15129
F. P. Burke
S. Harding
D. Nichols

127. CUMMINS ENGINE COMPANY, Box 3005, MC 50183, Columbus, IN 47202-3005
T. M. Yonushonis

128-129. DEVASCO INTERNATIONAL, INC., 9618 W. Tidwell, Houston, TX 77041
J. L. Scott
J. F. Turner

130. DOW CORNING CORPORATION, 3901 S. Saginaw Road, Midland, MI 48686-0995
W. H. Atwell

131. DOW CORNING CORPORATION, 1800 M Street NW, #325 South, Washington, D.C. 20036
J. K. Wessel

132. J. DOWICKI, P.E., 19401 Framingham Dr., Gaithersburg, MD 20879

133. DUPONT LANXIDE COMPOSITES, INC., Pencader Plant, Box 6100, Newark, DE 19714-6100
J. K. Weddell

134-136. DUPONT LANXIDE COMPOSITES, INC., 1300 Mallows Road, P.O. Box 6077, Newark, DE 19914-0302
A. Z. Fresco
D. Landini
G. White

137. EC TECHNOLOGIES, INC., 3614 Highpoint Dr., San Antonio, TX 78217
D. J. Kenton

138-140. EG&G IDAHO, INC., Idaho National Engineering Laboratory, P.O. Box 1625, Idaho Falls, ID 83415
A. B. Denison
B. H. Rabin
R. N. Wright

141-146. ELECTRIC POWER RESEARCH INSTITUTE, P.O. Box 10412, 3412 Hillview Avenue, Palo Alto, CA 94303
W. T. Bakker
R. A. Brown
S. Gehl
R. Goldstein
J. Stringer
I. Wright

147. ENERGY AND ENVIRONMENTAL RESEARCH CENTER, Box 8213, University Station, Grand Forks, ND 58202
J. P. Hurley

148. ENERGY AND WATER RESEARCH CENTER, West Virginia University, Morgantown, WV 26505-5054
C. L. Irwin

149. ENVIRONMENTAL PROTECTION AGENCY, Global Warming Control Division (MD-63), Research Triangle Park, NC 27711
K. T. Janes

150. ERC, INC., P. O. Box 417, Tullahoma, TN 37388
Y. C. L. Susan Wu

151-152. EXXON RESEARCH AND ENGINEERING COMPANY, Clinton Township, Route 2 East, Annandale, NJ 08801
M. L. Gorbaty
S. Soled

153. FERRO CORPORATION, 603 West Commercial St. E., Rochester, NY 14445
P. S. Way

154. FLUIDIZED BED TECHNOLOGIES, 1 Northgate Park, Suite 403, Chattanooga, TN 37415
R. Q. Vincent

155. FORSCHUUGS ZENTRUM JÜLICH GmbH, ICT, Postfach 1913, D-5170 Jülich, Germany
H. Barnert-Wiemer

156-158. FOSTER WHEELER DEVELOPMENT CORPORATION, Materials Technology Dept., John Blizard Research Center, 12 Peach Tree Hill Road, Livingston, NJ 07039
J. L. Blough
T. V. Narayanan
S. Van Wheele

159. FRAUNHOFER-INSTITUT für WERKSTOFFMECHANIK, Wohlerstrass 11, 79108 Freiburg, West Germany
R. Westerheide

160. GAS RESEARCH INSTITUTE, 8600 West Bryn Mawr Avenue, Chicago, IL 60631
H. S. Meyer

161. GENERAL APPLIED SCIENCE LABS, 77 Raynor Avenue, Ronkonkoma, NY 11779
M. Novack

162. GEORGIA INSTITUTE OF TECHNOLOGY, Georgia Tech Research Institute/MSTL, 123D Baker Bldg., Atlanta, GA 30332
T. L. Starr

163. GRI, 8600 W. Bryn Mawr, Chicago, IL 60656
D. Scarpiello

164. HAYNES INTERNATIONAL, INC., 1020 W. Park Avenue, Kokomo, IN 46904
G. Y. Lai

165-166. HOSKINS MANUFACTURING COMPANY, 10776 Hall Rd., Hamburg, MI 48139
R. B. Brennan
F. B. Hall

167. HYDROCARBON RESEARCH, INC., P.O. Box 6047, New York & Puritan Avenue, Lawrenceville, NJ 08648
S. H. Hildebrandt

168. ILLINOIS INSTITUTE OF TECHNOLOGY, METM Dept., Perlstein Hall, IIT, Chicago, IL 60616
J. A. Todd-Copley

169. INCO ALLOYS INTERNATIONAL, INC., P. O. Box 1958,
Huntington, WV 25720
S. Tassen

170. INTECH, INC., 11316 Roven Dr., Potomac, MD 20854-3126
P. Lowe

171. IOWA STATE UNIVERSITY, Ames Laboratory, 107 Metals Development,
Ames, IA 50011
D. J. Sordelet

172. LIQUID CARBONIC INDUSTRIAS S.A, Avenida Rio Branco, 57-6° Andar,
Centro - 20090-004, Rio De Janeiro, Brazil
M. Saddy

173. JET PROPULSION LABORATORY, 4800 Oak Grove Dr., MS-79-21,
Pasadena, CA 91020
R. L. Chen

174. LANXIDE CORPORATION, 1 Tralee Industrial Park, Newark, DE 19711
E. M. Anderson

175. LAVA CRUCIBLE-REFRACTORIES CO., P.O. Box 278,
Zelienople, PA 16063
T. Mulholland

176-179. LAWRENCE BERKELEY LABORATORY, University of California,
1 Cyclotron Road, Berkeley, CA 94720
T. M. Devine
P. Y. Hou - MS 62-203
G. Rosenblatt
S. Visco

180. LAWRENCE LIVERMORE NATIONAL LABORATORY, P.O. Box 808,
Livermore, CA 94551
J. H. Richardson (L-353)

181. LEHIGH UNIVERSITY, Energy Research Center, 5 E Packer Avenue,
Bethlehem, PA 18015
J. N. DuPont

182. E. LORIA, 1829 Taper Drive, Pittsburgh, PA 15241

183-185. LOS ALAMOS NATIONAL LABORATORY, P.O. Box 1663,
Los Alamos, NM 87545
R. G. Castro - MS G720
J. D. Katz
D. Phillips

186-187. MANUFACTURING SCIENCES CORPORATION, 804 Kerr Hollar Road, Oak Ridge, TN 37830
R. Hayes
T. Muth

188-190. MARTIN MARIETTA-KAPL, P.O. Box 1072, MS G2-312, Schenectady, NY 12301
J. J. Letko (MS D2-121)
G. A. Newsome
J. Woods

191. MER CORPORATION, 7960- S. Kolb Road, Tucson, AZ 85706
L. Leaskey

192-193. MOBIL RESEARCH & DEVELOPMENT CORPORATION, P. O. Box 1026, Princeton, NJ 08540
R. E. Searles
S. T. Viscontini

194-197. NASA LEWIS RESEARCH CENTER, 21000 Brookpark Road, Cleveland, OH 44135
J. P. Gyekenyesi
N. Jacobson - MS 106-1
S. R. Levine
R. Miller - MS 24-1

198-200. NATIONAL INSTITUTE OF STANDARDS AND TECHNOLOGY, Materials Building, Gaithersburg, MD 20899
S. J. Dapkunas
L. K. Ives (Bldg. 220, Rm. A-215)
S. G. Malghan

201. NATIONAL MATERIALS ADVISORY BOARD, National Research Council, 2101 Constitution Avenue, Washington, DC 20418
K. M. Zwilsky

202. NEW ENERGY AND INDUSTRIAL TECHNOLOGY DEVELOPMENT ORGANIZATION, 1800 K Street, N.W., Suite 924, Washington, DC 20006
T. Fukumizu

203-205. NEW ENERGY AND INDUSTRIAL TECHNOLOGY DEVELOPMENT ORGANIZATION, Sunshine 60 Bldg., P.O. Box 1151, 1-1 Higashi-Ikebukuro 3-Chome, Toshima-Ku, Tokyo, 170, Japan
S. Hirano
H. Narita
S. Ueda

206-207. NETHERLANDS ENERGY RESEARCH FOUNDATION ECN,
P.O. Box 1, 1755 ZG Petten, The Netherlands
P. T. Alderliesten
M. Van de Voorde

208. NORCONTROL, Duran Marquina 20, 15080 La Coruna, Spain
S. Gomez

209-210. NORTH CAROLINA A&T STATE UNIVERSITY, Department of Mechanical Engineering, Greensboro, NC 27411
J. Sankar
R. Vaidyanathan

211. OFFICE OF NAVAL RESEARCH, Code 431, 800 N. Quincy St., Arlington, VA 22217
S. G. Fishman

212. OHIO STATE UNIVERSITY, Department of Metallurgical Engineering, 116 W. 19th Avenue, Columbus, OH 43210
R. A. Rapp

213-216. PACIFIC NORTHWEST LABORATORIES, P.O. Box 999, Richland, WA 99352
T. R. Armstrong
J. L. Bates
L. R. Pederson
K. S. Ramesh (MSIN K3-59)

217. PALL CORPORATION, 5E Packer Avenue, Whitaker Laboratory #5, Bethlehem, PA 18015
T. Haq

218. PENNSYLVANIA STATE UNIVERSITY, 101 Steidle Building, University Park, PA 16802
R. Tressler

219. PSI TECHNOLOGY COMPANY, 20 New England Business Center, Andover, MA 01810
C. L. Senior

220. REMAXCO TECHNOLOGIES, INC., 1701 Louisville Dr., Suite C, Knoxville, TN 37921
D. Nixdorf

221. RENSSELAER POLYTECHNIC INSTITUTE, Materials Engineering Department, Troy, NY 12180-3590
N. S. Stoloff

222. RIBBON TECHNOLOGY CORPORATION, P.O. Box 30758,
Columbus, OH 43230
T. Gaspar

223. RILEY STOKER CORPORATION, 5 Neponset Street, Worcester, MA 01606
D. P. Kalmanovitch

224. RISO NATIONAL LABORATORY, P.O. Box 49, DK-4000, Roskilde,
DENMARK
Aksel Olsen

225. ROLLED ALLOYS, 125 West Sterns Road, Temperance, MI 48182
J. C. Kelly

226. SANDIA NATIONAL LABORATORIES, 7011 East Avenue, P.O. Box 969
Livermore, CA 94551-0969
J. E. Smugeresky (MS-9402)

227-231. SANDIA NATIONAL LABORATORIES, P.O. Box 5800,
Albuquerque, NM 87185
L. L. Baxter
R. Bradshaw
G. Carlson
G. Samara
A. Sault

232-233. SARGENT AND LUNDY, 55 E Monroe Street, Chicago, IL 60603
R. J. Kerhin
D. G. Sloat

234-235. SCIENCE APPLICATIONS INTERNATIONAL CORPORATION,
1710 Goodridge Dr., McLean, VA 22102
J. T. Bartis
J. Ward (MS 2-20-1)

236. SFA PACIFIC, INC., 444 Castro Street, Suite 920, Mountain View, CA 94041
N. Korens

237. SHELL DEVELOPMENT COMPANY, P.O. Box 1380,
Houston, TX 77251-1380.
L. W. R. Dicks

238. G. SORELL, 49 Brookside Terrace, N. Caldwell, NJ 07006

239. SOUTHERN RESEARCH INSTITUTE, 2000 Ninth Avenue South,
Birmingham, AL 35202
H. S. Starrett

240. SOUTHWEST RESEARCH INSTITUTE, 6620 Culebra Road,
P.O. Drawer 28510, San Antonio, TX 78284
F. F. Lyle, Jr.

241. SRI INTERNATIONAL, 333 Ravenswood Avenue, Meno Park, CA 04025
Y. D. Blum

242. SRS TECHNOLOGIES, 990 Explorer Blvd., Huntsville, AL 35806
J. H. Laue

243. STATE ELECTRICITY COMMISSION OF VICTORIA, Herman Research
Laboratory Library, Howard St., Richmond, Victoria,
3121 Australia
H. Hodgskiss

244-245. STRESS ENGINEERING SERVICES, INC., 415 Glensprings Drive, Suite 200,
Cincinnati, OH 45246
C. Haynes
D. Marriott

246. SUNDSTRAND, 4747 Harrison Ave., Rockford, IL 61125
D. Oakey

247. SUPERKINETICS, 2881 Tramway Place, NE,
Albuquerque, NM 87122
J. V. Milewski

248. SWANSON ENGINEERING ASSOCIATES CORPORATION,
4050 Washington Rd., McMurray, PA 15317
R. H. Mallett

249. TECHNIWEAVE, INC., 109 Chestnut Hill Road, Rochester, NH 03868
J. A. LeCoustaouec

250. TECHNOLOGY ASSESSMENT AND TRANSFER, 133 Defense Highway,
Suite 212, Annapolis, MD 21401
J. Hanigofsky

251. TECHNOLOGY MANAGEMENT INC., 9718 Lake Shore Blvd.,
Cleveland, OH 44108
B. P. Lee

252. TELEDYNE ALLVAC, P.O. Box 5030, Monroe, NC 28110
A. L. Coffey

253-255. TENNESSEE VALLEY AUTHORITY, 3N66A Missionary Ridge Place,
Chattanooga, TN 37402-2801
J. B. Brooks
C. M. Huang
A. M. Manaker

256. TEXAS A&M UNIVERSITY, Engineering/Physics Building, College Station, TX 77843-3123
M. N. Srinivasan

257. TEXAS EASTERN TRANSMISSION CORPORATION, P.O. Box 2521, Houston, TX 77252
D. H. France

258. THE AMERICAN CERAMIC SOCIETY, INC., 735 Ceramic Place, Westerville, OH 43081
L. Sheppard

259-261. THE CARBORUNDUM COMPANY, Technology Division, P. O. Box 832, Niagara Falls, NY 14302
T. P. DeAngelis
W. E. Hollar, Jr.
R. S. Storm

262. THE JOHNS HOPKINS UNIVERSITY, Materials Science & Engineering, Maryland Hall, Baltimore, MD 21218
R. E. Green, Jr.

263. THE MATERIALS PROPERTIES COUNCIL, INC., United Engineering Center, 345 E. Forty-Seventh St., New York, NY 10017
M. Prager

264. THE NORTON COMPANY, High Performance Ceramics Division, Goddard Road, Northboro, MA 01532-1545
N. Corbin

265. THE RALPH M. PARSONS COMPANY, 100 West Walnut St., Pasadena, CA 91124
J. B. O'Hara

266. THE TORRINGTON COMPANY, Advanced Technology Center, 59 Field Street, Torrington, CT 06790
W. J. Chmura

267. THIRD MILLENNIUM TECHNOLOGY, INC., 120 Sherlake Drive, P.O. Box 23556, Knoxville, TN 37933-1556
C. F. VanConant

268. TRW, 1455 E. 195th Street, Cleveland, OH 44110
M. Kurup

269-270. UNITED TECHNOLOGIES RESEARCH CENTER, Materials Department, 411 Silver Lane, East Hartford, CT 06108
N. S. Bornstein
J. E. Holowczak

271. UNIVERSITY OF CALGARY, 2500 University Dr. NW, Calgary, Canada
S. X. Mao

272. UNIVERSITY OF CALIFORNIA, Department of Materials Science and Mineral Engineering, University of California, Building 66-Room 247, Berkeley, CA 94720
R. O. Richie

273. UNIVERSITY OF KENTUCKY, Center for Applied Energy Research, 3572 Iron Works Pike, Lexington, KY 40511-8433
F. Derbyshire

274. UNIVERSITY OF NORTH DAKOTA, P.O. Box 9018, University Station, Grand Forks, ND 58202
J. P. Hurley

275. UNIVERSITY OF NOTRE DAME, Department of Materials Science and Engineering, P. O. Box E, Notre Dame, IN 46556
T. H. Kosel

276. UNIVERSITY OF SOUTH AUSTRALIA, Department of Metallurgy, The Levels SA 5095 Australia
K. N. Strafford

277-280. UNIVERSITY OF TENNESSEE, Department of Materials Science and Engineering, Knoxville, TN 37996
R. A. Buchanan
P. Liaw
C. D. Lundin
P. Qiao

281-283. UNIVERSITY OF TENNESSEE SPACE INSTITUTE, Tullahoma, TN 37388
W. H. Boss
J. W. Muehlhauser
M. White

284. UNIVERSITY OF WASHINGTON, Department of Materials Science and Engineering, 101 Wilson, FB-10, Seattle, WA 98195
T. G. Stoebe

285. UOP, 50 E. Algonquin Road, Des Plaines, IL 60017-5016
G. J. Antos

286-287. U.S. BUREAU OF MINES, Tuscaloosa Research Center, P. O. Box L, Tuscaloosa, AL 35486
J. C. Debsikdar
J. Kwong

288. U.S. BUREAU OF MINES, Department of the Interior, 2401 E. St., NW
Washington, DC 20241
S. Dillich

289. U.S. BUREAU OF MINES, P. O. Box 70, Albany, OR 97321
J. Woodyard

290. U.S. DEPARTMENT OF TREASURY, 1500 Pennsylvania Ave., N.W.,
Rm. 5132, Washington, DC 20220
J. Benton

291. VEBA OEL, P. O. Box 45, 4650 Gelsenkirchen-Buer, Germany
D. Fuhrmann

292-293. VIRGINIA POLYTECHNIC INSTITUTE AND STATE UNIVERSITY,
Department of Materials Engineering, Blacksburg, VA 24061
W. Curtin
K. L. Reifsnyder

294. WESTERN RESEARCH INSTITUTE, 365 N. 9th Street, P. O. Box 3395,
University Station, Laramie, WY 82071
V. K. Sethi

295-298. WESTINGHOUSE ELECTRIC CORPORATION, Research and Development
Center, 1310 Beulah Road, Pittsburgh, PA 15235-5098
M. A. Alvin
D. L. Keairns
T. Lippert
S. C. Singhal

299. WESTINGHOUSE HANFORD COMPANY, P.O. Box 1970, L6-39,
Richland, WA 99352
R. N. Johnson

300. WORCESTER POLYTECHNIC INSTITUTE, 100 Institute Road,
Worcester, MA 01609
E. Ma

301. DOE CHICAGO OPERATIONS OFFICE, 9800 S. Cass Ave., Argonne,
IL 60439
J. Jonkouski

302. DOE IDAHO OPERATIONS OFFICE, 765 DOE Place, Idaho Falls,
ID 83406
J. B. Malmo

303-317. DOE MORGANTOWN ENERGY TECHNOLOGY CENTER,
P.O. Box 880, Morgantown, W VA 26505
R. A. Bajura
R. C. Bedick
D. C. Cicero
F. W. Crouse, Jr.
R. A. Dennis
U. Grimm
J. S. Halow
N. T. Holcombe
W. J. Huber
M. J. Mayfield
W. J. McMahon
W. R. Miller
J. E. Notestein
H. A. Webb
J. S. Wilson

318-319. DOE OAK RIDGE OPERATIONS OFFICE, Oak Ridge, P. O. Box 2008,
Oak Ridge, TN 37831-6269
Assistant Manager for Energy Research and Development
E. E. Hoffman

320. DOE OFFICE OF BASIC ENERGY SCIENCES, Materials Sciences Division,
ER-131, GTN, Washington, DC 20545
J. N. Mundy

321. DOE OFFICE OF COAL TECHNOLOGY, FE-232 GTN,
Washington, DC 20585
M. Perlsweig

322. DOE OFFICE OF ENERGY EFFICIENCY AND RENEWABLE ENERGY,
CE-12, Forrestal Building, Washington, DC 20545
J. J. Eberhardt

323-324. DOE OFFICE OF ENERGY RESEARCH, 14 Goshen Court, Gaithersburg,
MD 20882-1016
N. F. Barr
F. J. Wobber

325-332. DOE OFFICE OF FOSSIL ENERGY, Washington, DC 20585
W. Fedarko (FE-232)
K. N. Frye (FE-13)
S. C. Jain (FE-231)
C. E. Pax (FE 73)
T. B. Simpson (FE-231)
M. I. Singer (FE-70)
H. E. Thomas (FE-73)
G. F. Wheeler (FE-231)

333. DOE OFFICE OF NAVAL REACTORS, NE-60, Crystal City Bldg., N.C.-2, Washington, DC 20585
J. Mosquera

334. DOE OFFICE OF PETROLEUM RESERVES, Analysis Division, FE-431, 1000 Independence Ave., Washington, DC 20585
D. de B. Gray

335-347. DOE PITTSBURGH ENERGY TECHNOLOGY CENTER, P. O. Box 10940, Pittsburgh, PA 15236
A. H. Baldwin
J. L. Balzarini
R. A. Carabetta
R. C. Dolence
P. Goldberg
J. D. Hickerson
J. J. Lacey
S. R. Lee
M. E. Maher
G. V. McGurl
J. A. Ruether
C. Smith
T. M. Torkos

348-349. DOE, OFFICE OF SCIENTIFIC AND TECHNICAL INFORMATION, P.O.Box 62, Oak Ridge, TN 37831

For distribution by microfiche as shown in DOE/OSTI-4500, Distribution Category UC-114 (Coal Based Materials and Components)